May 2014

Stress Ratio Effects in Fatigue of Lost Foam Cast Aluminum Alloy 356

David Elijah Palmer
University of Wisconsin-Milwaukee

STRESS RATIO EFFECTS IN FATIGUE OF LOST FOAM CAST ALUMINUM ALLOY 356

by

David E. Palmer, P.E.

A Thesis Submitted in

Partial Fulfillment of the

Requirements for the Degree of

Master of Science

in Engineering

at

The University of Wisconsin-Milwaukee

May 2014

ABSTRACT
STRESS RATIO EFFECTS IN FATIGUE OF LOST FOAM CAST ALUMINUM ALLOY 356

by
David E. Palmer, P.E.

The University of Wisconsin-Milwaukee, 2014
Under the Supervision of Professor Pradeep K. Rohatgi

Lost foam casting is a highly versatile metalcasting process that offers significant benefits in terms of design flexibility, energy consumption, and environmental impact. In the present work, the fatigue behavior of lost foam cast aluminum alloy 356, in conditions T6 and T7, was investigated, under both zero and non-zero mean stress conditions, with either as-cast or machined surface finish. Scanning electron microscopy was used to identify and measure the defect from which fatigue fracture initiated. Based on the results, the applicability of nine different fatigue mean stress equations was compared. The widely-used Goodman equation was found to be highly non-conservative, while the Stulen, Topper-Sandor, and Walker equations performed reasonably well. Each of these three equations includes a material-dependent term for stress ratio sensitivity. The stress ratio sensitivity was found to be affected by heat treatment, with the T6 condition having greater sensitivity than the T7 condition. The surface condition (as-cast vs. machined) did not significantly affect the stress ratio sensitivity. The fatigue life of as-cast specimens was found to be approximately 60 – 70% lower than that of machined specimens at the same equivalent stress. This reduction could not be attributed to pore size alone, and is suspected to be due to the greater concentration of pyrolysis products at the as-cast surface. Directions for future work, including improved testing methods and some possible methods of improving the properties of lost foam castings, are discussed.

TABLE OF CONTENTS

LIST OF FIGURES

LIST OF TABLES

LIST OF EQUATIONS

LIST OF SYMBOLS

α …….. Weibull characteristic life parameter; Topper-Sandor mean stress parameter

A ……...……. Stulen mean stress parameter

β …… Weibull shape parameter

γ …… Walker mean stress parameter

b ……...……. Basquin fatigue life exponent

ε ……..……. Strain

ε_{min} ……..…… Minimum strain

ε_{max}……..…… Maximum strain

ε_m ……..……...…… Mean strain = $(\varepsilon_{max} + \varepsilon_{min}) / 2$

ε_a …… Alternating strain = $(\varepsilon_{max} - \varepsilon_{min}) / 2$

E ……. Tensile modulus

σ ……..……. Stress

σ_f' …… True fracture stress; Basquin fatigue stress coefficient

σ_{min} ……..…… Minimum stress

σ_{max} ……...……..…… Maximum stress

σ_m ……..……...…… Mean stress = $(\sigma_{max} + \sigma_{min}) / 2$

σ_a ……...…… Alternating stress = $(\sigma_{max} - \sigma_{min}) / 2$

R ……..…… Stress ratio = $\sigma_{min} / \sigma_{max}$

LIST OF ABBREVIATIONS

AFS …….. American Foundry Society

ASME …….…… American Society of Mechanical Engineers

ASTM …… American Society for Testing and Materials

BRP …….. Bombardier Recreational Products

CAD …… Computer-aided design

CFD ……..….Computational fluid dynamics

CMM …….. Coordinate measuring machine

CNC ……..……. Computer numeric control

DAS ……..……. Dendrite arm spacing

DOE ……...….. U.S. Department of Energy

EPAC …… Expanded polyalkene carbonate

EPC ……..…… Evaporative pattern casting or expendable pattern casting

EPE ……..…… Expanded polyethylene

EPMMA ……...…… Expanded poly(methyl methacrylate)

EPS ……...…… Expanded polystyrene

EVA ……..…….. Ethyl vinyl acetate

FDM ……..…… Finite difference method

FEA, FEM ……..……. Finite element analysis, finite element method

LCA ……...……. Life cycle analysis

LF, LFC ……...…… Lost foam, lost foam casting

MMC ……...…… Metal matrix composite

PSA ……..……. Pressure sensitive adhesive

PVAc ……..…….. Polyvinyl acetate

StMMA ……..…… Styrene-co-(methyl methacrylate)

SWT …….……. Smith-Watson-Topper equation

TGA …… Thermogravimetric analysis

UAB …….…….. University of Alabama at Birmingham

UMR …….…… University of Missouri–Rolla

UWM …… University of Wisconsin–Milwaukee

ACKNOWLEDGEMENTS

This thesis was many years in the making, and many people deserve thanks. First, I wish to thank UWM Distinguished Professor Dr. Pradeep K. Rohatgi for his patience and support over the course of this project. I would also like to thank CEAS Graduate Program Specialist Betty Warras for her invaluable assistance in navigating the official requirements of the UWM Graduate School.

This research was fully supported by my employer, Bombardier Recreational Products (BRP). I would like to take this opportunity to thank my BRP colleagues around the world, without whom this project would have been impossible. In particular, thanks are due to Glover Kerlin in Spruce Pine, NC; Bill Barth, Ken Chung, Matt Coyne, Todd Craft, Ben Jones, Mark Noble, and Rich Smock in Sturtevant, WI; Karl Glinsner and Pete Lucier in Gunskirchen, Austria; and Jim Bonifield (retired).

In addition, I would like to thank a number of experts who graciously took the time to discuss this work with me: Harry Littleton of the University of Alabama at Birmingham, Dr. Norman Dowling of Virginia Tech, Dr. Nikhilesh Chawla of Arizona State University, and Dr. Sheldon Mostovoy of the Illinois Institute of Technology.

Finally, and most importantly, I would like to thank my family: my parents, Patrick and Joan Palmer, of Chicago, Illinois; my wife Lorenita Palmer; and my children Carlos, Adelyn, and Kriscia, for being my inspiration and my motivation.

CHAPTER 1 – INTRODUCTION

1.1.1 BACKGROUND

The lost foam casting process, also known as evaporative pattern casting or expendable pattern casting (EPC), has been used for many years to produce a wide variety of components (1). First used for art castings (2), the automotive and outboard engine industries were among the first to adopt this technology commercially (3). It continues to be widely used to manufacture engine blocks, cylinder heads, crankcases, and other powertrain components. One of the key advantages of the process is that it makes it possible to cast these components – which typically have elaborate internal passages for cooling – without the need for cores. This is because patterns for lost foam casting can be built up from multiple sections of expanded polymer foam, glued together with a hot-melt adhesive. This method of pattern construction provides a great deal of design versatility.

Powertrain components manufactured using the lost foam process are often subjected to severe and repeated loading. For example, a cylinder head may be subjected to combustion loads amounting to thousands of pounds, hundreds of times per second. Therefore, designers must consider the possibility of fatigue. Fatigue is a failure mode that occurs as a result of accumulated damage over multiple cycles, at stress levels that may be many times lower than the tensile strength of the material (4). The widespread use of computer-aided design (CAD) and finite element analysis (FEA) allows designers

to predict the stresses to which a given component will be subjected. However, in order to make good use of the output of FEA software and prevent fatigue failures, designers must also have a good understanding of the fatigue behavior of the material.

The fatigue properties of cast metals are largely determined by the presence of pre-existing defects (5). Such defects may include porosity (either gas or shrinkage porosity), non-metallic inclusions, oxide folds, second-phase particles, or surface discontinuities. These defects may initiate fatigue cracks that propagate under cyclic loading. For lost foam castings, in particular, the surface finish resulting from the use of expanded foam patterns must be taken into account. Gaps between the expanded foam beads are filled with ceramic slurry during the coating process; when the molten metal is poured and the foam pattern evaporates, these gaps are re-created in the metal casting. This is shown in schematic form in Figure 1. These surface defects can initiate fatigue cracks. A scanning electron micrograph of a fatigue crack in an outboard engine cylinder block is shown in Figure 2. As may be seen, the crack originated in a gap between foam beads.

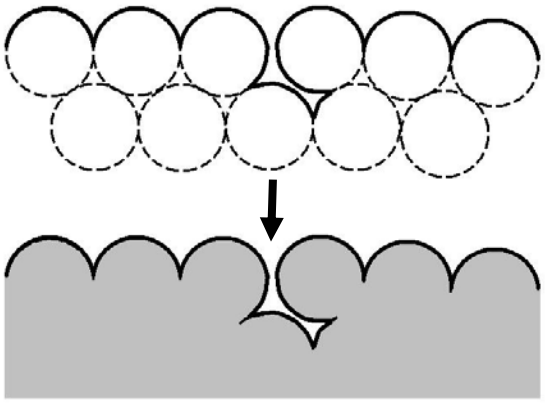

Figure 1. Schematic of as-cast surface of lost-foam casting. Top: surface of foam pattern (foam beads shown with dotted line). Bottom: resulting surface of metal casting.

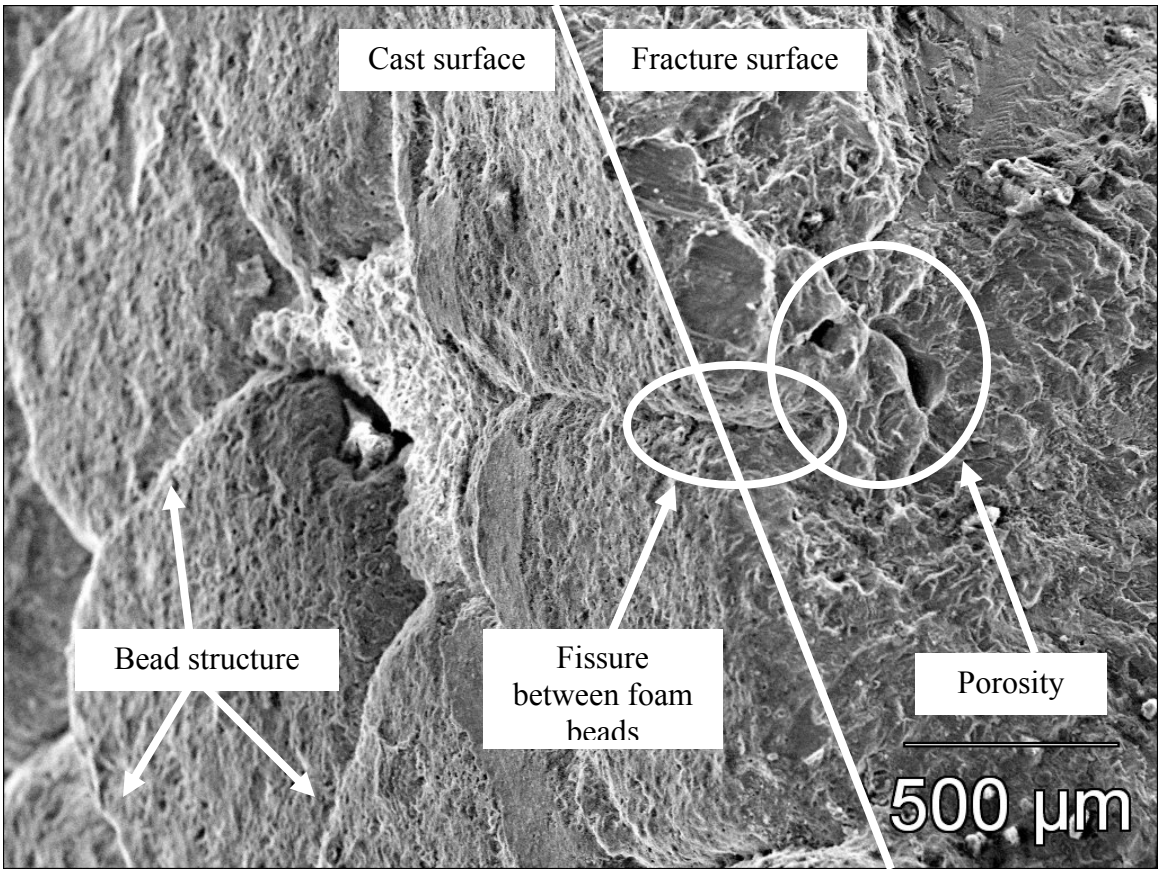

Figure 2. Scanning electron micrograph of fatigue crack in lost-foam outboard engine cylinder block casting. Left: cast surface; right: fracture surface. Some residual ceramic (refractory) is visible at the center left. Well-defined fatigue striations can be seen in the upper right. The fatigue crack appears to have initiated from a fissure between foam beads, along with a pocket of subsurface porosity. Ductile tearing appears to have taken place in the immediate vicinity of these two defects, followed by fatigue crack propagation.

Fatigue stresses may be thought of as consisting of two components: mean stress and alternating stress. This is shown in Figure 3, which shows stress vs. time for generalized sinusoidal fatigue. The stress varies between a minimum value (σ_{min}) and a maximum value (σ_{max}). The mean stress (σ_m) is the time average of the stress; for any symmetric load form (sinusoidal or not), it is the average of the maximum and minimum stress. The alternating stress (σ_a) is one-half of the difference between the minimum and maximum. The stress ratio R is defined as the maximum stress divided by the minimum stress. It is also possible (and sometime useful) to conceptualize fatigue as consisting as

cyclic strain; the definitions for minimum strain, maximum strain, mean strain, and alternating strain are exactly analogous to those for minimum stress, maximum stress, etc.

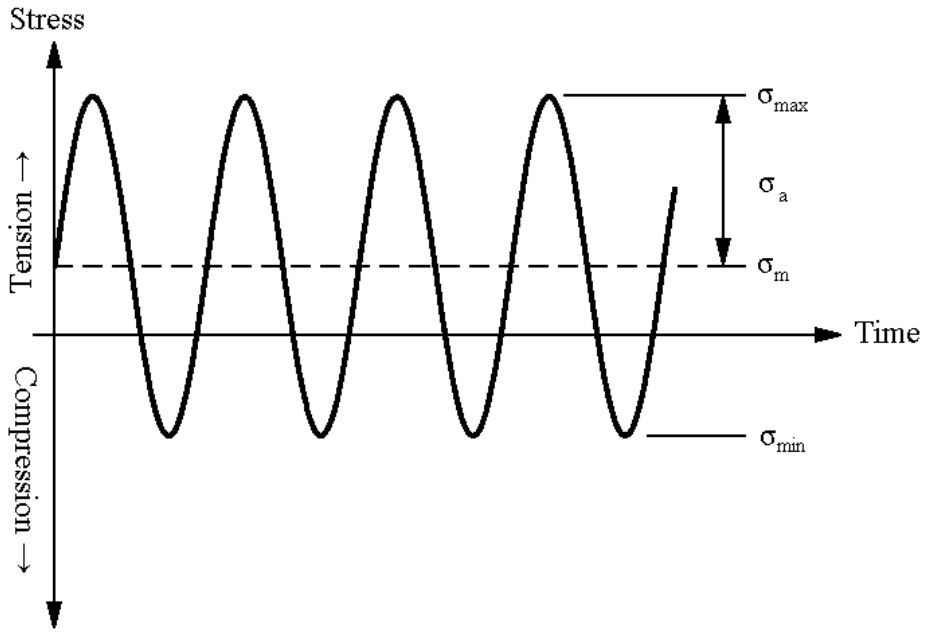

Figure 3. Stress vs. time for generalized sinusoidal fatigue. σ_{max} is maximum stress, σ_a is alternating stress, σ_m is mean stress, and σ_{min} is minimum stress.

Published fatigue strengths typically correspond to fully-reversed loading, i.e. zero mean stress (6). However, many applications involve non-zero mean stresses. Standard mechanical engineering design textbooks (7) provide three criteria for evaluating the effects of mean stresses: the Goodman equation (8, 9), the Soderberg equation (10), and the Gerber equation (11). Several other criteria, more or less similar in form to these three well-known equations, have been advanced in recent years. These include the ASME-Elliptic equation (7), the Bagci equation (12), and the Clemson equation (13). Many other mean stress equations have been proposed. These include the Stulen equation (14), the Morrow equation (15), the Smith-Watson-Topper equation (16),

the Walker equation (17), the Topper-Sandor equation (18), and the Leis equation (19), among others. The purpose of each of these equations is to relate the fatigue behavior of a material under non-zero mean stress conditions to its behavior under fully reversing conditions. The existence of such a large number of different equations suggests that no single equation yields completely satisfactory results for all materials under all conditions. After all, if such an equation did exist, it could be expected that all of the other equations would be largely forgotten.

Based on the considerations discussed above, there is a need for designers of lost-foam components to have reliable data regarding the fatigue behavior of metals cast using this process. Specifically, it is necessary for designers to understand how the as-cast surface, as well as internal defects, affects the fatigue life of lost foam castings. It is also necessary to have adequate data regarding the specific alloy used (in this case, aluminum alloy 356) and the heat treatments employed (T6 and T7). In addition, it is necessary to establish how these castings respond to fatigue with non-zero mean stress, and which of the dozen or so mean stress equations that have been proposed is most applicable. The purpose of this work is to provide answers to these questions so that the durability of lost foam components may be improved.

1.2 LITERATURE REVIEW

Since its invention in the 1950s (1), the lost foam casting process has been studied extensively, particularly through a long-running research initiative jointly sponsored by

the U.S. Department of Energy and the American Foundry Society that began in 1989 and continues to this day, with the most recent report issued in 2011 (20 – 27). Fatigue has been a topic of study since the first half of the 19th century (28), with the role of mean stress becoming recognized by the second half of that century (8, 11). Today, more than 175 years after Wilhelm Albert's first paper on the subject, it continues to be a vibrant area of research. The modern study of the role of defects in fatigue began in the late 1950s as a result of the failure of welded rocket cases due to porosity (29); recent work focuses on 3-D defect characterization (30), modeling (31), finite-element analysis (32), and statistical techniques (33). Aluminum alloy 356 is one of the most widely-used and widely-studied aluminum casting alloys, and a great deal of data is available regarding its properties for various casting methods. While a truly comprehensive review of this literature and its development would be extremely lengthy, a summary is presented below.

1.2.1 LOST FOAM CASTING

1.2.1.1 HISTORICAL BACKGROUND

The first patent for lost foam casting was issued to Shroyer in 1958 (1). Shroyer describes a "cavityless casting method," in which a pattern is made from expanded polystyrene foam, or another material that will rapidly disintegrate upon contact with molten metal, leaving minimal residue. The pattern may be machined from an extruded foam block, or molded from foam beads. If the shape to be cast is particularly complex,

the pattern may be assembled from multiple foam sections, attached to one another by "simple cementing, doweling, or wiring." The pattern is then placed in a flask; the flask is filled with bonded sand, which is rammed against the pattern. Molten metal is then poured into the mold, displacing the foam, which is converted into gaseous and liquid pyrolysis and/or combustion products that escape through vents made in the mold with an icepick. Once the metal has solidified, the casting may be knocked out of the mold using conventional knock-out techniques. The main advantages of this method, as described by Shroyer, include the ability to produce castings that would otherwise require complex cores and difficult parting lines, as well as the ability to economically produce small-run castings without investing in expensive tooling.

While Shroyer was the first to patent this technology, it may have already been in use by 1956, when Shroyer's patent was filed. In a presentation delivered to the Institute of Indian Foundrymen's annual convention in 2012 (34), M.C. Flemings described a visit to the studio of artist Alfred Duca in early 1956, where he observed Duca using polystyrene foam to produce patterns for art castings. "Pegasus," one of the first castings produced by Duca using this process, is shown in Figure 3. This sculpture is currently located at the deCordova Sculpture Park and Museum in Lincoln, Massachusetts. Flemings and Duca, along with Howard F. Taylor, conducted research into this process at the Metallurgy Department of the Massachusetts Institute of Technology, with the goal of reducing casting defects and encouraging wider production of art castings in the United States (2). They developed two important modifications to Shroyer's method: the use of a ceramic slurry to coat the foam patterns prior to placement in the flask, and the use of

unbonded rather than bonded sand. This last modification was developed based on discussions with Thomas Smith of the Maytag Company, who patented the unbonded sand process in 1964 (35). The ceramic slurry helped to reduce sand penetration defects, while the higher permeability of the unbonded sand reduced the need for venting. With these changes, the essential elements of the modern lost foam casting process were in place.

Figure 4. "Pegasus" (1959) by Alfred Duca, one of the first castings produced using the lost foam technique. Bronze, 42" x 36" x 36", deCordova Sculpture Park and Museum Permanent Collection 2001.55, gift of Veronique Bernard in memory of Alfred Duca. Photo used with permission of the deCordova Sculpture Park and Museum.

For the next decade, a company called Full Mold Process, Inc. licensed both the bonded and unbonded sand processes, and kept them under close control. After the Shroyer patent expired in 1975, Full Mold Process attempted to maintain control of the technology under an additional patent, which covered the use of ceramic slurry to coat foam patterns (36). In 1980, this patent was found to be invalid by U.S. District Court

Judge Anna Diggs Taylor, largely on the basis of the prior work published by Flemings and Duca (37).

Judge Taylor's decision, along with the expiration of the Smith patent the following year, meant that companies could freely pursue the lost foam casting process without the need to pay royalties. This resulted in widespread adoption of the process, especially by automotive and outboard engine manufacturers, in the first part of the 1980s (3). This is when many of the commercial lost foam foundries currently in operation in the United States, including the Bombardier Recreational Products (formerly Outboard Marine Corporation) facility in Spruce Pine, North Carolina, were built (38).

1.2.1.2 PROCESS DESCRIPTION

At this point, it is perhaps worthwhile to take a detour from the historical narrative to describe in depth the lost foam casting process that is employed at BRP-Spruce Pine. A schematic of this process is shown in Figure 5. This process, with a few variations, is more or less representative of the process as it is practiced worldwide.

The process begins with polystyrene beads, with a diameter of 0.25 – 0.50 mm. Polystyrene is an amorphous polymer with a glass transition temperature of 100°C. This means that it is hard and brittle at room temperature, but rubbery above 100°C. The beads are supplied pre-impregnated with approximately 5 – 7% pentane by weight. Pentane is a liquid alkane with a boiling point of 36°C.

In the first step of the process, the beads are placed in a reactor vessel and pre-expanded by means of flowing steam. This causes the pentane to boil and the polystyrene to undergo a glass transition, expanding the beads to a diameter of 0.75 – 1.5 mm. (Smaller beads, with a pre-expanded diameter of 0.50 – 1.0 mm, are sometimes used to mold thin-section parts). As the beads cool, the pentane condenses inside them, causing the polystyrene beads to shrink somewhat. Therefore, it is necessary for the pre-expanded beads to be stabilized under controlled conditions of temperature and humidity for a period of time (6 – 12 hours) prior to use. Excessive aging leads to loss of the pentane blowing agent by diffusion through the walls of the polystyrene beads.

The pre-expanded beads are then blown into a mold cavity using compressed air. The mold cavity typically consists of two mold halves, which are generally CNC machined from aluminum billet. Mold cavities are usually fabricated from a specialized 7000-series aluminum alloy designed for injection molding applications, such as Alcoa QC-7 or QC-10, although 6061-T6 has also been used with good success. The mold halves are mounted on steam chests, one stationary and one movable. The molds are designed with multiple vents, consisting of slits about 2 mm wide and 5 – 10 mm in length, and one or more fill gun ports, through which the pre-expanded beads are introduced. After the beads are introduced into the mold cavity, superheated steam at approximately 120°C and 100 – 200 kPa is applied by means of the steam chests. This causes the beads to expand and fuse. The mold halves are then cooled by means of a water spray. Once the pattern has cooled, the moveable steam chest is retracted, and the

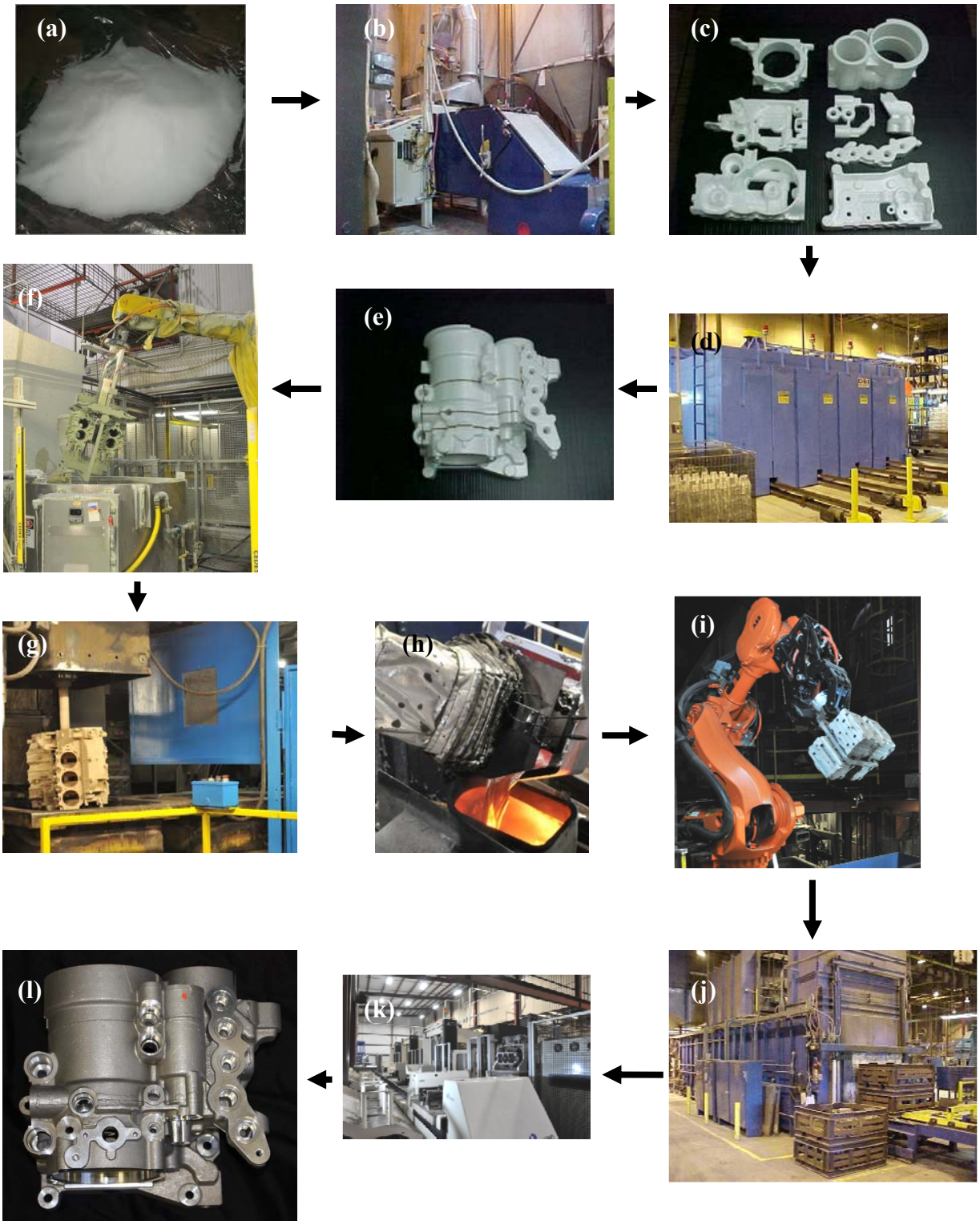

Figure 5. Schematic of lost foam casting process at BRP-Spruce Pine. (a): raw polystyrene bead, (b): pre-expansion; (c): pattern molding; (d): pattern drying; (e): pattern assembly; (f): pattern coating; (g): placement in flask and sand fill; (h): pouring; (i): shakeout; (j): heat treatment; (k): machining; (l): finished casting. The casting shown in (c). (e), and (l), a fuel filter housing for a heavy truck, was awarded "Best in Class" in the 2010 AFS Casting of the Year competition.

pattern is ejected from the mold. The resulting patterns are composed of a closed-cell expanded polystyrene (EPS) foam, with a density of about 22.4 – 25.6 kg/m³.

Inadequate compaction and incomplete fusion of the foam beads can produce pattern defects of the type shown in Figures 1 and 2. This is particularly true for patterns with complex geometry. Inadequate fusion occurs when the beads do not spend sufficient time at a temperature above T_g to conform to the cavity and fuse to one another. Factors contributing to this include inadequate steam volume or steaming time, poor venting, or low mold temperatures (21). In addition, variations in the molecular weight of the pattern material and absorption of blowing agent can affect bead fusion by altering T_g (25). Pattern fusion is measured using a permeability apparatus (27). The pattern permeability apparatus applies a 21 kPa vacuum pressure to the surface of a pattern. When the vacuum is applied, air flows in through the gaps between the foam beads. The flow rate of the air is measured using a mass flow meter. The greater the degree of pattern fusion, the lower the air flow rate will be.

After molding, patterns are cured in an oven at 60 – 70°C for 3 – 4 hours. Pattern curing achieves several important ends: it dries the pattern of the water introduced during the steam cycle, eliminates any residual blowing agent, and dimensionally stabilizes the patterns.

Besides the use of molded EPS patterns, as described above, patterns may also be CNC machined from extruded polystyrene foam (28). This method is particularly well

suited to prototyping, as it avoids the time and cost associated with tooling. It is also possible to use CNC machining to produce patterns from pre-formed EPS blocks. However, one problem encountered during the machining of molded foam blocks is the "pull out" of foam beads. For this reason, extruded foam is preferred; when molded foam blocks are used, it is preferable to use foam with as small of a bead size as possible.

While EPS is the most widely-used pattern material in the lost foam industry, other types of polymer foam have been used. Besides EPS, the most common pattern materials include expanded poly(methyl methacrylate) (EPMMA) (20), and co-polymers of styrene and methyl methacrylate (StMMA) (22, 39). Expanded polyalkene carbonate (EPAC) has also seen some limited use, particularly for iron castings (40). Expanded polyethylene was mentioned as a possible material in Shoyer's original patent (1), but does not appear to have gained much acceptance. Polyurethane foam has also been evaluated as a pattern material for lost foam castings (26, 48), but was judged to be unacceptable, due to its low stiffness, higher density, poor degradation behavior, and potentially hazardous pyrolysis products.

Patterns for lost foam castings are typically built up from multiple foam sections, glued together with a suitable adhesive. Typically, ethyl vinyl acetate (EVA) hot melt glue is used. The sections are assembled using an automated glue machine, consisting of an upper platen, a lower platen, and a glue platen. One foam section to be assembled is held in an aluminum nest in the upper platen, while the other is held in an aluminum nest in the lower platen. The glue platen, with an aluminum glue print plate, is held in a bath

of holt melt glue at a temperature of 120 – 130°C. To assemble the pattern, the upper platen is moved into place above the glue pot. The glue platen is then raised until the glue print plate contacts the foam pattern in the upper nest, applying the glue print. The glue platen is then retracted, and the upper platen is moved into place above the lower platen. The lower platen rises up and mates the lower foam to the upper foam. The lower platen is then retracted, and the assembled pattern can be released from the nest.

Many defects in lost foam castings occur around the glue line, for reasons that will be discussed later in this section. Despite the importance of the gluing process, the selection of adhesives for lost foam casting is a subject that has received relatively little attention in published works (26). In general, it is important for the adhesive to have a relatively low melting point, so that it does not harm the foam patterns when applied. (However, if the melting/softening point of the adhesive is too low, the glue joint may fail during the slurry drying process). It is also desirable for the adhesive to have low ash content, and to have a similar thermal degradation profile to the pattern material. In addition, the adhesive must have adequate strength, so that it does not crack during the pattern coating, sand fill, or compaction processes.

For prototype castings made from machined extruded foam, hot melt glue is applied using a glue gun. Due to the time required to assemble patterns by hand, it is necessary to select a hot melt glue with a somewhat longer working time than that used in the automated glue machine. This is typically achieved by increasing the fraction of low molecular weight EVA. Polyolefin-based hot melts provide even longer working times,

but have higher dispensing temperatures (160 – 200°C) that tend to make them unsuitable for use with EPS patterns. Air-setting glues based on polyvinyl acetate (PVAc) are readily available and provide a much longer working time than hot melts, but, based on this author's experience, produce unacceptable levels of casting defects, due to their higher ash content (~1.5% for PVAc vs. ~0.2% for EVA hot melt), as well as their high moisture content if not fully dried. Furthermore, PVAc forms a brittle bond that may break during coating or compaction. Spray-applied pressure sensitive adhesive (PSA) has also been tried, but does not adequately seal the glue joint from slurry penetration during the coating process. Researchers at the University of Alabama at Birmingham (UAB) investigated a protein-based adhesive, but found it to be unacceptable as well (26). The use of rubber cements has been reported (41), and appears to be quite popular in amateur craft casting, although the selection of a rubber cement requires caution, since many rubber cements contain solvents (i.e. acetone, hexane, heptane, or toluene) that will dissolve polystyrene.

After the patterns are assembled, one or more patterns are attached to a sprue. Like the patterns, the sprue may be made from molded foam or extruded foam. The patterns are glued to the sprue using the same techniques described above for pattern assembly. The assembly of the patterns and sprue is customarily referred to as a cluster.

The assembled cluster is then coated with ceramic slurry. The slurry consists of refractory particles (typically silica, aluminum, zircon, and/or aluminosilicate) in water with a binder (typically colloidal silica), along with various additives, including

dispersants, surfactants, and thixotropic agents. The use of fly ash as a refractory material has been investigated (42). The purpose of the coating is twofold: first, to prevent sand penetration as the EPS pattern is replaced by molten metal, and second, to permit the liquid and gaseous pyrolysis products of the EPS pattern to escape from the mold. Therefore, the permeability of the coating is a key parameter. According to Goria et al (43), if the coating does not have sufficient permeability, gaseous pyrolysis products will be trapped inside the mold, temporarily halting the advance of the metal front until the evolved gases bubble out through the molten metal. As each bubble escapes, the metal front will advance violently, distorting the mold cavity. In addition, the gas and liquid pyrolysis products will create defects in the casting. On the other hand, if the permeability of the coating is too high, the evolved gases will escape so quickly that the gas pressure will be insufficient to resist the weight of the sand, leading to collapse of the mold cavity. Several different methods of measuring coating permeability have been developed (22, 43-46). Most methods involve measuring the flow rate of air through a coated stainless steel mesh (46) or through a dried wafer of coating (22, 45); the original method of Goria (43) involved measuring the time required for the applied pressure and the atmospheric pressure to equalize. Cluster coating is typically performed using a robot, which immerses the cluster in a slurry dip tank, then drains the cluster in such a way that all of the internal and external surfaces of the patterns are evenly coated with slurry. This operation can also be done by hand.

The coated clusters are loaded onto a conveyor, which takes them through an overhead drying oven, where they are dried for two hours at 60°C. The thickness of the

dried coating is typically between 0.1 – 0.5 mm. In some foundries, additional drying is achieved by the use of microwave energy (47). After passing through the drying oven, the clusters are placed in a chamber where they are exposed to microwave energy at a density of 500 – 1100 W/m^3 for a period of 6 – 15 minutes. Microwave radiation heats materials by forcing oscillations of molecular dipoles. Water, a highly polar molecule, is readily heated by microwave radiation. Ceramics are ionic solids that lack molecular dipoles and are essentially transparent to microwave radiation. The internal heating produced by microwave radiation increases the vapor pressure of the moisture within the ceramic coating, increasing the rate of moisture diffusion to the surface of the cluster, where it is removed by convection.

The dried, coated clusters are placed in a flask, which is clamped to a vibrating table. The flask is filled with unbonded silica sand using a rainfall sander. While the sand is being added to the flask, the flask is vibrated at a frequency of 30 – 50 Hz. The sand becomes fluidized and flows around the coated cluster. Further vibration compacts the sand around the cluster. It is sometimes necessary for patterns to have sand fill holes to ensure adequate sand fill in internal passages; these holes must be plugged or welded shut after the casting is made. Like the coating, the permeability of the sand is a critical parameter. The sand must be sufficiently permeable to allow pyrolysis products to escape, yet strong enough to maintain the shape of the mold cavity during the pouring process.

At this point, the castings are ready to be poured. Mold filling in the lost foam process is more complex than in other metalcasting processes. Rather than being poured into an empty mold, the molten metal must displace the foam pattern. (This is the origin of the term "full mold process," which distinguishes lost foam casting from "empty mold" processes). In lost foam casting, mold filling is accompanied by a number of heat- and mass-transfer processes, including melting and vaporization of the foam pattern and removal of gaseous and liquid pyrolysis products, which have no parallel in other casting methods. This has implications for both mold filling and solidification.

The first direct observation of lost foam mold filling was performed by Butler and Pope in 1964 (48). They poured aluminum into a polystyrene pattern in a specially-designed mold box with a glass window, with one surface of the pattern in contact with the window. This allowed them to observe the mold filling process in real time, and to record the process on film. A then-current theory suggested that a sizeable gap would form ahead of the metal front, but that pyrolysis products of the foam would be absorbed by the sand and act as a binder, preventing sand collapse. The real-time film showed that, provided that a suitably rapid pouring rate was used, no noticeable gap ever formed between the pattern and the metal. The film also showed that, if the pour was interrupted, a gap did in fact form ahead of the metal front. If no pattern coating was used, the sand collapsed catastrophically into the gap in less than 1 second, destroying the casting. With coating, the gap persisted for as long as 1 minute before collapse occurred. While the authors acknowledged that the presence of the glass window affected the process due to its low permeability, they concluded that the film provided a reasonable representation of

the pattern replacement mechanism. Based on their observations, they recommended fast pouring rates, preferably using a large pouring basin which is kept full during mold filling. This continues to be the preferred manner of pouring lost foam castings to the present day.

A more sophisticated physical model of the mold filling process was proposed by researchers at the University of Alabama-Birmingham (UAB) in 1993 (21). According to this model, when the molten metal contacts the foam pattern, the pattern softens and then decomposes into liquid and gas pyrolysis products; a significant volume of air (which makes up as much as 97% of the original volume of the expanded foam) is also released. As the metal front advances, the gasses (including air) and the liquid polymer are pushed to the metal-pattern-coating interface (later called the "kinetic zone"). The gaseous products diffuse through the coating and into the sand, while the liquid products wet the surface of the coating, then begin to wick through the coating. Low coating permeability results in a buildup of gas pressure within the mold, which reduces the velocity of the metal front and may produce misrun defects. Inadequate wettability of the coating may result in surface defects, where liquid products "pool" against the coating.

This theory was challenged by Zhao, Burke, and Gustafson in 2002 (49), who performed a number of partial mold filling trials, in which a lost foam mold contained in an open-bottom steel flask was lowered into a crucible filled with molten aluminum, then removed. On the basis of these trials, they proposed an alternate theory, which de-

emphasized the role of liquid pyrolysis products, and focused on pattern gasification as the primary mode of mass transfer.

With the advent of real-time x-ray and neutron radiography of the mold filling process, it became clear that the process was more complex than either model predicted. Based on neutron imaging, David Caulk of General Motors proposed four different filling "modes" that may occur under different conditions. The first is known as "contact mode" (51). This is the mode that typically occurs at the beginning of the filling process. In this mode, foam is removed by means of ablation by the liquid metal. The metal front has a convex shape. A layer of liquid pyrolysis products, approximately 0.1 – 0.2 mm thick, forms ahead of the advancing metal front. The liquid products are drawn towards the porous coating by convection, where they are absorbed, gasified, and diffuse out. This filling mode is considered to be the most desirable, because it produces fewer defects than the other modes.

The second mode identified by Caulk is called "gap mode" (52). This mode occurs when the advancing metal front overtakes pockets of liquid pyrolysis products. The liquid is vaporized, producing gas bubbles that travel upwards through the molten metal. A gas layer, or "gap," forms between the metal front and the pattern. The gas layer reduces heat transfer between the molten metal and the pattern material. The reduced heat flux into the pattern promotes removal by melting, rather than ablation. The liquid pyrolysis products are drawn together by surface tension and form globules at the coating surface. As the advancing metal front overtakes these globules, more gas is

produced, sustaining the gap. Because of the low heat transfer coefficient through the gap, mold filling proceeds more slowly in gap mode than in contact mode.

In addition to these two modes, Caulk identified a mode called "collapse mode" (53). This mode occurs particularly when there are density or fusion gradients within a pattern, i.e. regions where foam beads are not well-packed or well-fused. These regions provide an escape path for air and gaseous pyrolysis products, resulting in low local gas pressures. This allows the metal front to advance in "fingers." Liquid pyrolysis products accumulate along the perimeter of these "fingers." As the multiple metal fronts re-combine, pyrolysis products are trapped between them, producing fold defects.

The final mode identified by Caulk is known as "engulf mode." This mode can take place when the shape of the metal front changes from convex to concave. This occurs because the metal front is providing the pressure gradient in the decomposition layer that directs the foam decomposition products towards the coating. As the metal front becomes more concave, the pattern material surrounded by the concave metal front is softened. Eventually, chunks of the pattern are engulfed by molten metal. This results in a sudden and chaotic advance of the metal front. The foam chunks quickly decompose, releasing pyrolysis products within the molten metal. This filling mode is considered to be catastrophic and results in a large number of casting defects. Some possible measures to prevent foam engulfment suggested by Caulk are the use of brominated foam additives to reduce the viscosity of liquid decomposition products,

lowering metal velocity by decreasing coating permeability, reducing the pattern density and/or thickness, and pouring at higher temperatures.

A number of casting defects are particularly associated with glue joints. When the advancing metal front reaches the glue line, the metal velocity decreases, due to the greater thermal energy required to decompose the glue. As the metal breaks through the glue, multiple converging metal fronts are formed, resulting in fold defects (26). In addition, the greater density of the glue relative to the foam results an increased production of gaseous decomposition products, which may result in gas defects. Another type of glue line defect can occur if the glue joint breaks prior to the coating process. Slurry penetrates into the gap between the two foam sections, resulting in a corresponding gap in the metal casting (50). Furthermore, the ceramic slurry in the gap may not dry properly. When the advancing metal front reaches this slurry, the remaining water will be converted into steam, potentially producing gas defects. (This phenomenon can also occur in areas of poor pattern fusion, and may be the cause of the subsurface porosity observed in Figure 3).

An interesting and elegant analog of the lost foam mold filling process was developed by Ainsworth and Griffiths (55). They used mercury to represent liquid aluminum, and glucose to represent polystyrene pyrolysis products. Mercury was chosen because its viscosity at room temperature ($1.55 \cdot 10^{-3}$ Pa·s) approximates the viscosity of aluminum at lost foam casting temperatures ($1.22 \cdot 10^{-3}$ Pa·s). Glucose was chosen because it has a higher viscosity and lower density than mercury; similarly, liquid

polystyrene has a higher viscosity and lower density than molten aluminum. Under these conditions, a hydrodynamic phenomenon known as a "Saffman-Taylor instability" occurs. As the lower-viscosity, higher-density fluid (aluminum or mercury) advances into the higher-viscosity, lower-density fluid (glucose or polystyrene), the flow front forms "fingers." This is similar to the "collapse mode" proposed by Caulk, but does not require foam density gradients to occur. The use of brominated pattern additives to reduce the viscosity of the liquid polystyrene, or irradiation of the foam pattern to reduce the molecular weight of the polystyrene itself, were proposed as possible solutions.

While mold filling in lost foam casting is very different from mold filling in other metalcasting processes, the fundamentals of solidification in lost foam are not essentially different from solidification in insulating molds in general. It has been found that Chvorinov's rule applies to the solidification of lost foam cast aluminum alloy A356 (56). Cooling rates in lost foam casting of aluminum have been measured in the range of 0.3 – 0.7 °C/sec (57), which are somewhat higher than cooling rates in sand castings of comparable section thickness (typically on the order of 0.1 °C/sec or less). The cooling rate is affected by the presence of glue lines, with higher cooling rates observed in castings with a greater adhesive content (58). The higher cooling rates in lost foam casting compared to sand casting can be explained by the endothermic nature of the pattern decomposition process. However, cooling rates in lost foam casting are still significantly lower than those for casting processes that use metal molds, such as permanent mold or diecasting.

Shakeout of lost foam castings is simpler than for other sand casting processes. Since the sand is unbonded, the contents of the flask can simply be dumped onto a conveyer. The sand can be reused after cooling and classification (sieving) to the correct grain size. A portion of the sand is thermally reclaimed in order to remove foam pyrolysis products that have been deposited on the sand. The cast cluster is typically quenched in water, which helps to remove the ceramic coating. The castings are typically cut off the cluster using a bandsaw.

A detailed life cycle analysis (LCA) comparing the environmental impacts of lost foam casting, semi-permanent mold casting, and precision sand casting found that lost foam casting had the lowest overall environmental impact (59). Key to this was the ability of sand to be reused in the lost foam process. The overall energy consumption of the lost foam process (per 1000 kg of degated castings) was significantly lower than that of precision sand casting, and roughly equivalent to that of semi-permanent mold casting. Solid waste, liquid waste, and overall air emissions (including hydrocarbons, carbon monoxide, nitrogen oxides, sulfur oxides, and particulate matter) were lowest for lost foam casting. The study was based on data from approximately 14 million kg of lost foam castings, 45 million kg of semi-permanent mold castings, and 15 million kg of precision sand castings produced in 1996 in automotive foundries. The analysis specifically excluded machining and assembly processes. It is likely that, if the savings that can be realized by combining multiple components produced using other manufacturing techniques into a single lost foam casting were considered, the environmental benefits of the lost foam process would be even more apparent.

1.2.1.3 VARIATIONS ON THE LOST FOAM PROCESS

A number of variations on the lost foam casting process have been developed over the years, which deserve brief mention here. The main variants include the Replicast CS process (in which a ceramic shell is used on place of a sand-filled flask), the magnetic molding process (in which steel shot, held together with an applied magnetic field, is used in place of sand in the flask), lost foam casting with vacuum-assisted pouring, and lost foam casting with pressure solidification.

The Replicast CS process was developed in the early 1980s by M.C. Ashton at the Steel Castings Research and Trade Association in the United Kingdom (60). This process is a hybrid of lost foam casting and investment casting. As in lost foam casting, the patterns are made from molded foam. A ceramic shell is then built over the pattern by multiple applications of slurry and stucco, as in investment casting. In investment casting with wax patterns, it is necessary to melt the wax out of the coated mold in a steam autoclave prior to firing the ceramic shell, otherwise the expansion of the wax will crack the ceramic. In the Replicast CS process, this is unnecessary: coated molds, with the EPS patterns still inside them, are loaded directly into a 1000°C burnout oven. The foam burns out during the firing process of the shell. This results in an empty ceramic shell mold. Pouring and all subsequent operations are exactly the same as traditional lost wax investment casting. As a result, the defects related to pattern pyrolysis that are characteristic of the lost foam process are not typically encountered in castings made

using the Replicast CS process. In particular, there is no pick-up of carbon, which greatly facilitates the production of steel castings.

A further development of the ceramic shell process has been recently proposed by Guler et al (61). In this version, the EPS patterns are removed from the ceramic shell by means of a chemical solvent. Although Guler and his co-workers did not directly compare this process to the Replicast CS process, it is conceivable that chemical removal of the EPS pattern prior to the firing of the ceramic shell might further reduce defects related to pattern burn-off residue.

The magnetic molding process was developed by Hoffman and Wittmoser in Germany in the late 1960s (62). In this process, EPS patterns are assembled and coated as in the lost foam process. However, rather than sand, the flask is filled with a magnetic material, such as steel shot. A magnetic field is applied in order to lock the molding media in place. The casting is then poured as in the lost foam process. The magnetic field helps to ensure that the molding media does not shift during the filling of the mold. Once the mold is filled, the magnetic field is turned off and the casting is allowed to cool. The higher thermal conductivity of the steel shot (as compared to sand) results in a faster cooling rate, corresponding to a finer microstructure and improved mechanical properties. Research into the process was conducted in the Soviet Union in the 1970s and 1980s (63), but it never gained widespread acceptance in either the socialist or the capitalist countries. Recently, there has been a resurgence of interest in this process in the European Union. From 2004 to 2006, the European Commission funded a major multi-

country research program coordinated by Fundación Inasmet in Spain. This project included research institutions, foundries, and EPS producers in Spain, France, Germany, Poland, and the United Kingdom. Magnetically-molded castings were successfully produced in aluminum, bronze, cast iron, and steel (64).

Vacuum-assisted filling of lost foam molds is a topic that has received a great deal of interest, although up to now, the results have not quite lived up to expectations. According to the concept, applying vacuum during the filling of lost foam molds will allow pyrolysis products to be more removed more effectively, leading to lower defect rates. In practice, however, the applied vacuum also results in increased metal velocities, which promotes fold formation, so defect reduction is not actually realized (25). Littleton (27) demonstrated small, but statistically significant, improvements in the mechanical properties of aluminum alloy 319 lost foam castings by using applied vacuum and a lower pouring temperature. The lower pouring temperature limits the metal velocity so that filling is not too fast. In contrast, Shin et al (65) reported that vacuum, combined with a higher pouring temperature, produced good results for magnesium alloy lost foam castings. The differences can be explained by the lower heat content of the magnesium alloy, which results in a lower fluidity when cast in lost foam. The higher pouring temperatures and applied vacuum helped to increase the flow length of the molten magnesium. However, it was also found that excessive vacuum pressures (>50 kPa below atmospheric pressure) promoted filling by collapse mode or engulf mode, contributing to defect formation.

The concept of applying pressure during solidification of lost foam castings was mentioned in passing as early as 1964 in a paper by Butler and Pope (48). Isostatic pressure has two fundamental benefits: suppression of gas bubble formation and enhanced feeding during solidification (66). The concept of solidification under pressure was explored as early as the 1870s, when W.R. Jones in the United States, la Challasiere in France, and D.K. Chernov in Russia each experimented with the application of steam pressure to solidifying steel ingots (67). One of the first studies of the effect of pressure on the solidification of aluminum sand castings was performed by Hansen and Slater in 1935 (68). They found an increase in density of 2 – 4%, an increase in tensile strength of up to 70%, and an increase in elongation of up to 150% when solidifying aluminum sand castings in an autoclave under 1.4 MPa of nitrogen. Interestingly, contemporary response to Hansen and Slater's work was mostly negative. In the discussion published after their paper, one commenter stated that "although very interesting, this seems to me to be not the right way to go about the production of castings"; another stated that "the practical possibilities are not great," while one commenter suggested that "the authors of the paper should be confined to subterranean regions!" Nevertheless, research into pressure-assisted solidification of castings continued through the following decades. In the 1980s, the French company Aluminum Pechiney developed a process for solidification of lost foam castings under pressure (69). In this process, the flask consists of a pressure vessel with a hinged lid. After the casting is poured, the lid is closed and the vessel is pressurized with gas. A hydrostatic pressure of 1.0 – 1.5 MPa is developed over a period of 60 – 90 seconds. This process has been adopted at Mercury Marine, reportedly with great success (50). It is claimed that solidification under pressure has resulted in a 100%

increase in elongation and a 50% increase in fatigue strength of lost foam aluminum alloy A356 castings at Mercury (70). Similar improvements in the mechanical properties of lost foam A356 solidified under pressure were also reported by Kang et al (71), who also reported a significant decrease in dendrite arm spacing (DAS). Donahue has attributed the success of this technique for A356 to the low copper content of the alloy (<0.20% Cu), which prevents the formation of Al-Cu intermetallics that are believed to interfere with feeding (72). However, in 2011, Ghanti et al (73) demonstrated similar success with solidification under pressure of the aluminum-copper alloy A206, which contains 4.2 – 5.0% Cu. Both A356 and A206 are low-iron alloys (<0.20% Fe for A356, <0.10% Fe for A206). It quite possible that the low iron content plays a role in the technique's success, since it is known that the "needle-like" β-Al_5SiFe intermetallic (which actually forms in platelets, not needles) interferes with feeding (74).

The combined effect of vacuum filling and solidification under pressure of four different lost foam cast aluminum alloys (A356, A206, 319M, and 535) was discussed in a presentation by John Griffin at the 2014 AFS Metalcasting Congress (75). It was shown that the combination of 30 kPa vacuum during filling and 1 MPa pressure during solidification provided a significant improvement in tensile strength and ductility for all four alloys.

Another variation of the lost foam process, which includes both pressure and vacuum, is known as the low pressure lost foam process. This process, which is a hybrid of lost foam casting and low pressure permanent mold casting, was developed at the

Freiburg University of Mining and Technology in Germany in the late 1990s (76). In this process, a coated EPS cluster is placed in a flask, which is located directly above a holding furnace. The furnace is pressurized with gas, which forces the molten metal up a tube into the EPS mold above. Simultaneously, vacuum may be applied to the flask to facilitate removal of pattern pyrolysis products. The pressure-assisted counter-gravity filling helps to ensure that the metal front advances in contact mode, reducing filling-related defects. In recent years, this process has attracted a great deal of attention, particularly in China, as a method for producing magnesium alloy castings (77).

1.2.1.4 RECENT DEVELOPMENTS

Despite the large volume of work carried out over the past several decades, lost foam casting continues to be a fruitful field for research. Some of the topics that have received attention in recent years include the use of vacuum-assisted filling (27, 67), pressure under solidification (70, 72), or both (74), to reduce defects and improve mechanical properties. These techniques have been described above. Other subjects that have emerged in the present decade include the casting of magnesium alloys using lost foam, the use of the lost foam technique to produce metal matrix composites and hybrid structures, the application of vibration during solidification of lost foam castings to refine microstructure, the combination of lost foam casting with rapid prototyping techniques, and improvements in computational modeling. These topics will be briefly discussed below.

Magnesium alloys have attracted a great deal of attention over the past several years because of their low density and high strength-to-weight ratio. Magnesium alloy AZ91E has a density of 1810 kg/m³, compared to 2670 kg/m³ for aluminum alloy 356. Since both alloys have comparable tensile strength (~275 MPa) in the T6 condition, this means that the magnesium alloy has roughly 50% greater strength per unit mass. However, magnesium alloys are more challenging to cast, for a number of reasons. First, magnesium is highly reactive, which requires that the melt be protected from oxygen, either by a protective flux or a covering gas (78). In addition, while the heat of fusion for magnesium alloys is close to that of aluminum alloys (373 kJ/kg for magnesium alloy AZ91E vs. 389 kJ/kg for aluminum alloy 356), the lower density of magnesium means that the quantity of heat that must be removed in order to solidify a given volume of molten magnesium is significantly lower than the quantity of heat that would need to be removed from an equal volume of molten aluminum. Similarly, while the specific heat capacity of magnesium alloys is higher than that of aluminum alloys (1.43 kJ/kg·K for magnesium alloy AZ91E at pouring temperature vs. 1.08 kJ/kg·K for aluminum alloy 356 at pouring temperature), due to its lower density, an equal volume of molten magnesium has a lower heat content than molten aluminum. Flemings (79) developed a well-known equation for the fluidity of a superheated metal in an empty mold, which is given by Equation 1, on the following page.

From Equation 1, it can be calculated that, if both metals are poured with 100°C of superheat, and all other variables (metal velocity, mold diameter, heat transfer coefficient, and mold temperature) are held constant, magnesium alloy AZ91E will have

approximately 27% less fluidity than aluminum alloy 356. However, Flemings' equation was developed for an empty mold. In lost foam casting, the metal will not only lose heat to the mold, but also to the pattern material. The molten metal must have sufficient heat content to decompose the foam, or the metal front will stop. The relatively low heat content of magnesium has made it extremely challenging to cast in lost foam.

$$L_f \cong \frac{\rho_s a v}{2h(T_m - T_0)}(H + c'\Delta T)$$

Equation 1. Flemings' equation for fluidity, where:
L_f = fluidity length (m)
ρ_s = density of solid (kg/m³)
a = cross-sectional radius of casting (m)
v = metal velocity (m/s)
h = heat transfer coefficient (W/m²·K)
T_m = melting temperature (K)
T_0 = mold temperature (K)
H = heat of fusion (J/kg)
c' = heat capacity (J/kg·K)
ΔT = superheat (K)

The use of vacuum-assisted filling by Shin et al (65) to successfully cast magnesium alloy AZ91H in lost foam has already been discussed above. In 2005, Ji and Fan described the use of the low pressure lost foam process to successfully cast magnesium alloy AZ91E (77). Using this process, they were able to obtain monotonic tensile properties comparable to open-mold sand casting. The use of the low pressure lost foam process for magnesium alloys has been a topic of considerable interest in recent years, particularly in China, where at least 39 academic and conference papers, 4 doctoral dissertations, and 8 masters' theses have been published on this subject in the past decade (80).

In addition to the use of lightweight materials such as magnesium, further weight reductions can be obtained by the use of metal matrix composites and/or hybrid materials, such as sandwich panels, lattice structures, and metallic foams. Metal matrix composites (MMCs), which incorporate particulate or fiber reinforcements, can provide higher strength-to-weight ratios and stiffness-to-weight ratios than unreinforced metal allots. Casting has long been seen as an economical route to the production of such composites (81), but until recently, the production of MMCs using the lost foam process had not been explored. In 2011, Guler et al described a novel method of producing MMCs in lost foam (82). They produced patterns from alternating layers of EPS boards and SiC particles, held together with glue. The patterns were then coated and poured, as in the conventional lost foam process. The filling of the mold redistributed the SiC particles to some extent, although the particles continued to be arranged in layers. In 2012, Pakzaman et al (83) used a similar method to produce a lost foam aluminum MMC reinforced with a two-dimensional matrix of steel wires. The wire performs were sandwiched between EPS boards and held in place with tape. Wire volume fractions from 5.8 – 17.7% were investigated. Wire reinforcement was found to significantly increase both yield strength and tensile strength, with a modest reduction in ductility. Coating the wire performs with 15 μm of electroless nickel led to greater increases in yield strength and tensile strength, and smaller reductions in ductility. This was attributed to the suppression of Al-Fe intermetallic formation at the wire-matrix interface. Ho (84) investigated the use of lost foam casting to produce periodic cellular materials. A corrugated sandwich core, a pyramidal lattice core, and an integral pyramidal sandwich were produced by hot-knife machining from EPS blocks. These patterns were used to

produce sandwich panels using both aluminum alloy A356 and magnesium alloy AZ91. The magnesium sandwich panels were produced using vacuum-assisted filling. The lost foam AZ91 integral sandwich panels showed nearly two orders of magnitude higher compressive yield strength per unit density when compared to open-celled magnesium foams.

The application of mechanical vibration to a solidifying casting in order to refine microstructure is not a new technique. D.K. Chernov observed grain refinement in steel castings subjected to low-frequency vibration as early as 1878 (85). In a comprehensive literature review published in 1981, Campbell (86) introduced the concept of a frequency-amplitude map, and showed that a "grain multiplication regime" exists beyond a certain threshold of frequency and amplitude. He compared various theoretical models that had been proposed, and showed that the existing data was best explained by dendrite fragmentation increasing the number of nuclei available for solidification. Despite its long history, this technique has only recently been applied to lost foam castings. The apparent lack of investigation in this area is surprising; since vibrating tables are already used in the lost foam process to achieve sand compaction, using them to apply vibration during solidification would seem a natural outgrowth. In 2010, Fan et al (87) reported increases in the tensile strength and elongation, and decreases in the porosity fraction, of lost foam aluminum alloy 356 cast with 1 – 4 g peak acceleration during solidification and frequencies of 10 – 60 Hz. Peak accelerations above 4 g were found to result in reduced mechanical properties and increased porosity, due to sand collapse and coalescence of gas bubbles. In 2011, the same group reported significant increases in the

mechanical properties of lost foam magnesium alloy AZ91D solidified under mechanical vibration (88). It appears that work on this promising approach is continuing in China.

Rapid prototyping is an area that has received a great deal of attention in recent years, and the lost foam casting world is no exception to this. Many in the industry have argued that lost foam casting should itself be viewed as a rapid prototyping technique, since, with CNC machined EPS patterns, it is possible to produce lost foam castings in a short period of time, without any investment in tooling. However, in certain situations, the number of castings required may be large enough that producing patterns by CNC machining of EPS blocks would unacceptably time-consuming, yet also small enough (or the design uncertain enough) that production tooling can also not be justified. In such situations, it may be advantageous to use three-dimensional printing techniques to manufacture short-term tooling. Gervasi and Sheikh (89) described the use of the laminated object manufacturing (LOM) process to fabricate patterns of lost foam mold halves. The LOM mold halves were then used to produce a silicone mold. Steam vents were placed within the silicone mold cavity. The silicone cavity was then filled using an aluminum-epoxy composite. The resulting aluminum-epoxy mold halves were then mounted to a steam chest and used to produce EPS patterns, as in the conventional lost foam process. In recent years, direct fabrication of lost foam pattern tooling using rapid prototyping techniques has become popular. One commercial process, which is based on powder-binder printing, is known as the ProMetal process (90). A number of other proprietary processes are also in use.

The application of computational modeling to metalcasting is another area that has expanded widely in recent years. Lost foam casting has been a particularly challenging process to model, due to the complexity of the filling process. As described in the previous section, the work of the Lost Foam Consortium has been essential to the development of accurate casting simulation codes for the lost foam process. Flow-3D is a commercially-available computational fluid dynamics (CFD) code based on the finite difference method (FDM) and using the volume of fluid (VOF) method for tracking free surfaces. It was one of the first codes to be adapted for lost foam simulation (91). It continues to be widely used, and is updated on a regular basis. Some other commercially-available codes include ProCAST (92) and Magmasoft (93). In 2006, Hozeaux and Codina (94) described a lost foam casting model using the finite element method (FEM). Migbagheri and Davami (95) developed a code known as SUTCAST, based on a variation of the VOF method, which has also been used with success for lost foam casting. In addition, a commercial code known as Arena-flow-eps (96) has been developed to model the process of pattern blowing and steaming. Junxia et al (97) developed a numerical model of the lost foam pattern making process based on an Euler-Lagrange discrete particle model, and found a good correlation between this method and Arena-flow-eps. The widespread availability of simulation tools means that the development of lost foam castings no longer needs to proceed by trial and error. Instead, casting designs may be developed in a virtual space long before the first casting is poured.

In spite of the major advances in lost foam casting technology over the past few years, there has been an overall trend away from lost foam casting in the United States and Europe. In 2008, W.D. Griffiths of the University of Birmingham (U.K.) wrote that "the future of lost foam casting is currently uncertain, to say the least." (98) At a meeting of the Great Lakes Section of the Society for Industrial and Applied Mathematics in 2011, David Caulk of General Motors said that "lost foam casting is on the decline at General Motors, because the relatively low ultimate strength of aluminum cast in unbonded sand is not up to the high demands of current and future engine designs." (99) In 2013, Mark Ainsworth concluded a presentation to the South African Institute of Foundrymen by stating that lost foam casting is "a niche process for niche markets, requiring very tight parameter control." (100)

However, there continues to be strong interest in lost foam casting in emerging countries, including China, Iran, and India, among others. Lost foam developments in these three countries will be briefly outlined below.

In China, research into the lost foam casting process began in 1965, when members of the Academy of Machinery Science began to investigate the technique. The first industrial-scale production of lost foam castings in China started in 1967 at the Shanghai Heavy Machinery Plant. At that time, the focus of both research and industrial work was primarily on the use of the bonded sand method to make large (multi-ton) castings. Production of lost foam castings in China was relatively low until around 1995, when the process began to experience rapid growth. Also, at this time, the unbonded

sand process began to overtake the bonded sand process. In 1995, 15,200 tons of lost foam castings were produced in China, of which 7,200 tons were produced by the unbonded sand method. In 2005, 321,000 tons of lost foam castings were produced in China, of which 216,000 tons were produced by the unbonded sand method. By 2007, China overtook the United States as the world's leading producer of lost foam castings (101).

China has also outpaced the United States in its production of academic papers concerning the lost foam casting process. Of 86 papers published on the topic of lost foam casting in 2013, 42 (49%) were written by authors whose primary affiliation was to a Chinese institution. In comparison, only 7 (8%) were written by authors whose primary affiliation was to a U.S. institution. A full breakdown of 2013 lost foam papers by country is provided in Figure 6. Note that this figure only includes papers published in English. If papers published in other languages were included, the U.S. percentage of the total would almost certainly be smaller.

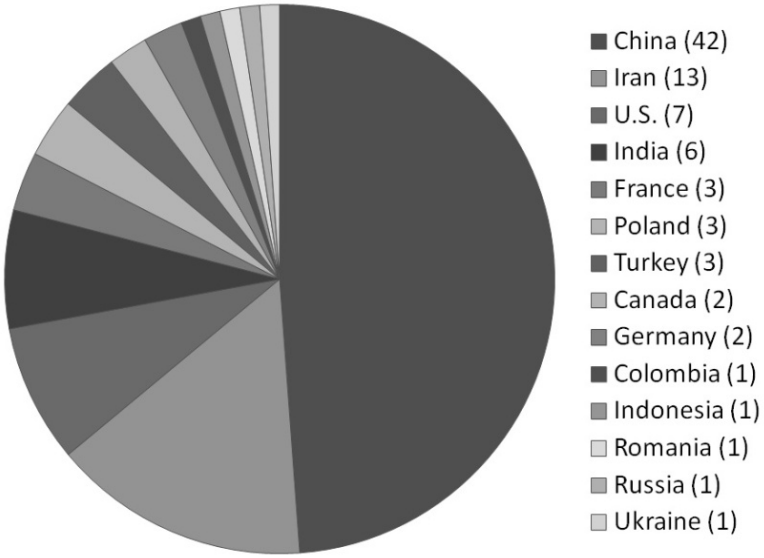

Figure 6. Lost foam publications by country, 2013.

As Figure 6 shows, Iran is the second country in terms of lost foam publications after China. Due to the poor relationship between the government of Iran and the government of the United States since 1979, there is very little information available in English regarding the state of the lost foam casting industry in Iran. However, published academic work by Iranian researchers focuses on practical aspects of the lost foam process, suggesting a healthy and growing industry. Examples of Iranian lost foam research include the previously cited works by Mirbagheri and Davami (95) on mold-filling simulation and by Pakzaman (83) on lost foam casting of aluminum MMCs. Other topics explored by Iranian researchers include gating of lost foam castings (102), pattern coatings (103), and compound lost foam castings, i.e. magnesium-alloy lost foam castings with integral aluminum inserts (104). In addition, some interesting work has been done recently in Iran on lost foam mold filling, revisiting the direct observation method of Butler and Pope (48): Khodai and Mirbagheri (105) modified the apparatus to include a gas flow meter to measure gas evolution, while Sharifi and Abadi (106) used the method to investigate the effects of gating and foam density.

In India, adoption of the lost foam casting process has been surprisingly slow, particularly considering the long history of metalcasting in India and the overall position of India in the global foundry industry. Gujarat Metal Casting began producing aluminum and malleable iron castings using the lost foam process in 1978, and was India's only lost foam foundry for many years. Another lost foam foundry, Alexcon Foamcast, opened in 1997, but failed in its first year, reportedly due to financial

irregularities. It has been suggested that the failure of Alexcon Foamcast discouraged other Indian foundries from pursuing the lost foam process. However, a small handful of foundries have adopted the technique in recent years. Interestingly, the foundries that have adopted the process in India have tended to focus on advanced variants, including the ceramic shell process and vacuum-assisted filling (107). Considering this focus, it is possible that significant developments in lost foam casting technology may come out of India in the near future.

Given the fact that the lost foam process had its genesis with the sculptures of Alfred Duca, it is perhaps appropriate to close this section with a mention of the Red Bull sculpture completed in Spielberg, Austria in May, 2012 (108). This sculpture, which marks the site of a racetrack, was designed to be easily seen from a roadway 2 km away. The sculpture depicts a bull jumping through an arch. The body of the bull is made from welded Corten steel plates. The arch is made from 83 lost foam aluminum blocks, weighing a total of 32,000 kg. The foam patterns for the arch were machined by a robot from CAD files. The bull's horns, which have a 7 m span, were also cast in aluminum using the lost foam process. This monumental sculpture is a symbol of the continued vitality of lost foam casting.

Figure 7. "Bull" (2012) by Clemens Neuebauer and Martin Kölldorfer. Corten steel and aluminum, Red Bull Ring, Spielberg, Austria.

1.2.2 FATIGUE AND MEAN STRESS

The first paper addressing the failure of metals as a result of cyclic loading was published by Wilhelm Albert in 1838, based on work he had done in 1829 (27). Albert, a German mining engineer, was concerned with the failure of mine hoist chains. He observed that the chains failed after repeated loads much smaller than those that would be needed to break the chains in a single cycle. Correctly recognizing the magnitude of the load and the number of cycles as the key variables, he devised a fatigue test for chains, using a water wheel and a pulley to raise and lower a set of weights. He attributed fatigue failure to an "adverse hardening" ("nachteiligen Härtung") effect, a viewpoint that would persist for several decades to come. On the basis of his fatigue tests of cast iron chains, and his finding of fatigue cracks even in chains that did not fracture, he invented modern steel wire rope.

The term "fatigue" was first used by French mathematician and engineer Jean-Victor Poncelet (109). In the 1841 edition of his treatise on industrial engineering, the word "fatigue" is mentioned 28 times. In most instances, it is used to refer to the muscular exhaustion of human beings and animals that were used to provide power for machinery in Poncelet's era. However, on two occasions in the text, Poncelet also used the term to refer to mechanical components themselves (compression springs and suspension rods). The implication was that, like human beings and other living things, inanimate objects could become exhausted after repeated exertion. While this is far from the current concept, "fatigue" has become the generally accepted term for failure resulting from cyclic loading.

The idea that the fatigue of metals was due to exhaustion or deterioration of their mechanical properties was widely held throughout the 1840s and 1850s – a period during which, thanks to the development and expansion of railroads, fatigue failure began to emerge as a serious problem. Partially due to the distinct appearance of fracture surfaces resulting from fatigue (as opposed to those resulting from tensile overload), it was believed that cyclic loading somehow caused the internal structure of metals to transform from "fibrous" to "crystalline," with the crystalline structure being the weaker of the two. Interestingly, Chernov's work regarding the effect of mechanical vibration on the solidification of metals (85) was erroneously cited as evidence for the crystallization theory. The debate regarding the crystallization theory in the United Kingdom is covered by Timoshenko (110). The theory was eventually overthrown by two facts: first, static

tests on railcar axles that had been subjected to cyclic loading failed to show any deterioration in mechanical properties; second, when examined under an optical microscope, steel claimed to be "crystalline" on the basis of its fracture surface failed to show any microstructural differences compared to steel exhibiting a "fibrous" fracture surface. (In spite of this – and the understanding that the structure of metals is almost always crystalline, except in the relatively exotic case of metallic glasses – the term "fibrous fracture" continues to be widely used in fractography).

From 1847 to 1870, August Wöhler conducted a systematic study of fatigue, with the goal of reducing fatigue failures in railcar axles. Wöhler's work is summarized by Timoshenko (110). Wöhler developed a rotating bending fatigue test, which used separately machined test specimens rather than full-sized axles. In Wöhler's test, rotating specimens were subjected to cantilever bending. The stress at any point in the outer fiber of the specimen at the support varied from a tensile value of σ_{max}, to a compressive value of σ_{min} ($= -\sigma_{max}$), and back to σ_{max}, in each cycle of rotation. This provided fully-reversed loading ($R= -1$). On the basis of this test, Wöhler determined that there was a "limiting stress," below which fatigue failure did not occur. This is now known as the endurance limit or fatigue strength (σ_e). For materials that do not show a definite limiting stress, it is defined as the stress at which a specimen fails in fully-reversed loading at a given (large) number of cycles.

Unlike previous authors, who assumed that the magnitude of σ_{max} determined fatigue life, Wöhler recognized the importance of the stress ratio. Therefore, he also

developed a (non-rotating) three-point bending fatigue test, which he used to perform tests at R=0 and R>0. He found that, for a given σ_{max}, the number of cycles to failure increased as σ_{min} increased. Unlike later authors, he did not propose an equation relating fatigue under fully-reversed conditions to fatigue with non-zero mean stress. However, for one particular steel used for axles, he provided a list of acceptable maximum stresses for five different minimum stresses.

In 1874, three years after Wöhler's results were published, Gerber (11) fitted a parabola to Wöhler's data. For the purposes of this parabola, Gerber assumed that the fatigue strength at zero alternating stress was equal to the ultimate tensile strength (σ_{max}). The Gerber equation can be written as:

$$\sigma_{eq} = \frac{\sigma_a}{1 - (\frac{\sigma_m}{\sigma_u})^2}$$

Equation 2. Gerber equation, where:
σ_{eq} = equivalent stress (MPa)
σ_a = alternating stress (MPa)
σ_m = mean stress (MPa)
σ_u = ultimate tensile strength (MPa)

In the Gerber equation and the equations that follow, the equivalent stress σ_{eq} is the fully-reversed stress that would result in failure in an equal number of cycles to the given alternating stress σ_a and mean stress σ_m. If the endurance limit σ_e is substituted for σ_{eq}, then the equation will yield a set of pairs of mean stresses and alternating stresses (σ_m, σ_a) that the material will be able to withstand for an indefinite number of cycles.

From the perspective of the 21st century, a number of objections to the Gerber equation may be raised. For one thing, the concept of a fatigue strength at zero alternating stress is problematic; if there is no alternating stress, there can be no fatigue. However, in Gerber's time, the distinction between fatigue and tensile overload was not as clear. Another weakness of the Gerber equation is that it predicts that compressive mean stresses will have a harmful effect on fatigue life. In fact, compressive mean stresses are generally beneficial. Despite these weaknesses, Gerber deserves credit as the originator of the first mean stress equivalence equation.

Perhaps the best-known mean stress equivalence equation is attributed to Goodman (8). Like Gerber, Goodman was also working with Wöhler's data of several decades earlier. Unlike Gerber, Goodman chose to fit the data with a line, rather than a parabola. Furthermore, Goodman assumed that the fully-reversed endurance limit was equal to one-third of the ultimate tensile strength σ_u, while the endurance limit for R=0 was equal to one-half of the ultimate tensile strength. Goodman based his reasoning on previously established design rules for dynamic loading in bridges. As Sendeckyj (111) points out, these rules were not original to Goodman, and dated back to the 1850s. Also, these rules were intended to deal with impact, not fatigue. Once again, it should be remembered that the distinctions between different failure modes were not clearly understood in the 19th century. Goodman developed a schematic representing this relationship, which is shown in Figure 8, on the following page. In this diagram, the lower line represents σ_{min}, while the upper line represents σ_{max}. The vertical distance between the two lines represents the allowable stress range.

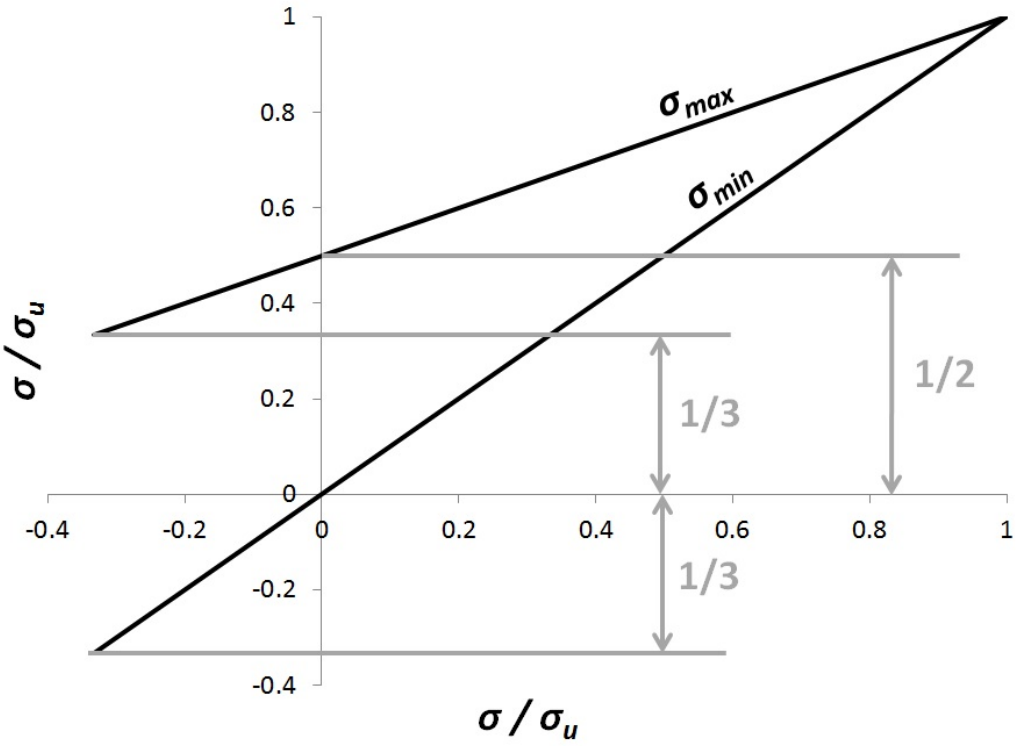

Figure 8. Goodman diagram.

Figure 8 is not the familiar form of the Goodman diagram. Instead, a modified version of the Goodman diagram is used, as shown in Figure 9. This modification was first proposed by Haigh in 1917 (9). In this version, mean stress is shown on the horizontal axis, while alternating stress is shown on the vertical axis. Haigh also discarded Goodman's insistence that the fully-reversed endurance limit must be equal to one-third of the ultimate tensile strength, and instead used the experimentally-determined endurance limit σ_e. In the United States, Figure 9 is usually referred to as the "Goodman diagram" or the "modified Goodman diagram." In Europe, it is usually referred to as the "Haigh diagram." Haigh himself used the term "constant life diagram." Similarly, the associated equivalent stress equation (Equation 3) is widely referred to as the "Goodman equation," even though it is not actually due to Goodman. Throughout this work,

Equation 3 will be referred to as the Goodman equation, following accepted usage, although it is recognized that this is something of a misnomer.

$$\sigma_{eq} = \frac{\sigma_a}{1 - (\frac{\sigma_m}{\sigma_u})}$$

Equation 3. Goodman equation, where:
σ_{eq} = equivalent stress (MPa)
σ_a = alternating stress (MPa)
σ_m = mean stress (MPa)
σ_u = ultimate tensile strength (MPa)

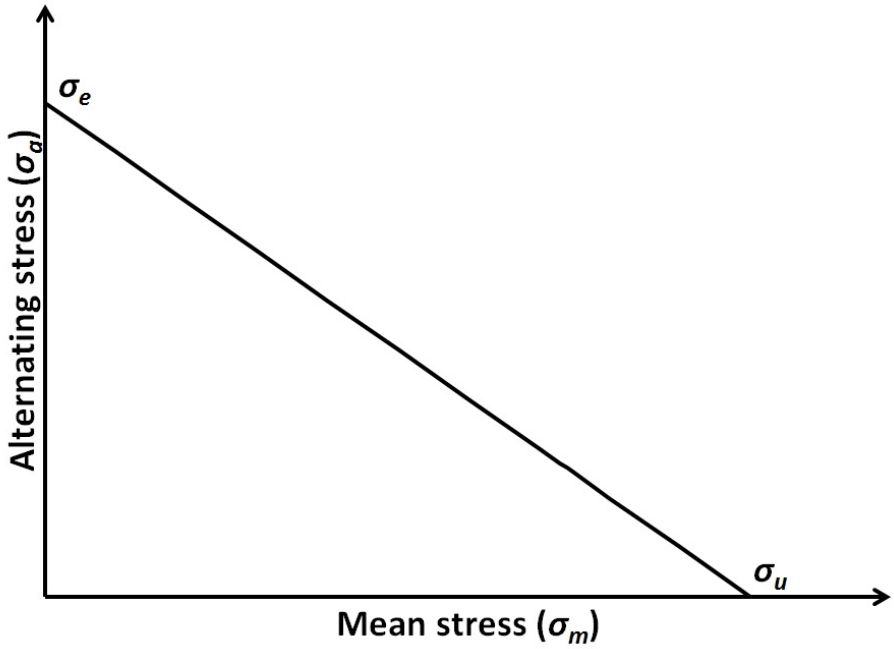

Figure 9. Haigh constant life diagram (also known as "Goodman diagram" or "modified Goodman diagram").

In 1930, Soderberg (10) pointed out that application of the Goodman equation in design without consideration of other criteria could allow mean stresses in excess of the yield strength σ_y. He therefore proposed an alternative equation, which is given in

Equation 4, below. Soderberg's reasoning shows that the distinction between fatigue failure and failure due to monotonic loading was still not clear, even into the 20th century.

$$\sigma_{eq} = \frac{\sigma_a}{1 - (\frac{\sigma_m}{\sigma_y})}$$

Equation 4. Soderberg equation, where:
σ_{eq} = equivalent stress (MPa)
σ_a = alternating stress (MPa)
σ_m = mean stress (MPa)
σ_y = yield strength (MPa)

Another equation of the same form was proposed by Morrow in 1968 (15). The Morrow equation (Equation 5) is equivalent to the Goodman equation, except that the ultimate tensile strength σ_u is replaced by the true fracture strength σ_f'. Since the true fracture strength is not always known, Morrow suggests using the fatigue strength coefficient from the Basquin equation (Equation 6) as an alternative.

$$\sigma_{eq} = \frac{\sigma_a}{1 - \left(\frac{\sigma_m}{\sigma_f'}\right)}$$

Equation 5. Morrow equation, where:
σ_{eq} = equivalent stress (MPa)
σ_a = alternating stress (MPa)
σ_m = mean stress (MPa)
σ_f' = true fracture strength or Basquin fatigue strength coefficient (MPa)

$$\sigma_a = \sigma_f'(2N_f)^b$$

Equation 6. Basquin equation, where:
σ_a = alternating stress (MPa)
σ_f' = fatigue strength coefficient (MPa)
N_f = cycles to failure
b = fatigue life exponent

An equation similar in form to the Gerber equation was proposed by Loewenthal in 1975 (112). This equation was incorporated into ASME Standard B106.1 in 1985 (113), and is generally known as the ASME-Elliptic equation (7).

$$\sigma_{eq} = \frac{\sigma_a}{\sqrt{1 - \left(\frac{\sigma_m}{\sigma_y}\right)^2}}$$

Equation 7. ASME-Elliptic equation, where:
σ_{eq} = equivalent stress (MPa)
σ_a = alternating stress (MPa)
σ_m = mean stress (MPa)
σ_y = yield strength (MPa)

An equation of a different form was proposed by Smith, Watson, and Topper (16) in 1970. Unlike the equations discussed above, the Smith-Watson-Topper equation (often abbreviated SWT) does not depend on any monotonic mechanical properties.

$$\sigma_{eq} = \sqrt{\sigma_a(\sigma_a + \sigma_m)}$$

Equation 8. Smith-Watson-Topper (SWT) equation, where:
σ_{eq} = equivalent stress (MPa)
σ_a = alternating stress (MPa)
σ_m = mean stress (MPa)

The six equations described above (Gerber, Goodman, Soderberg, Morrow, ASME-Elliptic, and SWT) are shown together on a constant-life diagram in Figure 10. Since the Smith-Watson-Topper equation does not depend on any monotonic mechanical properties, its relationship to the other equations may vary from that shown in the figure.

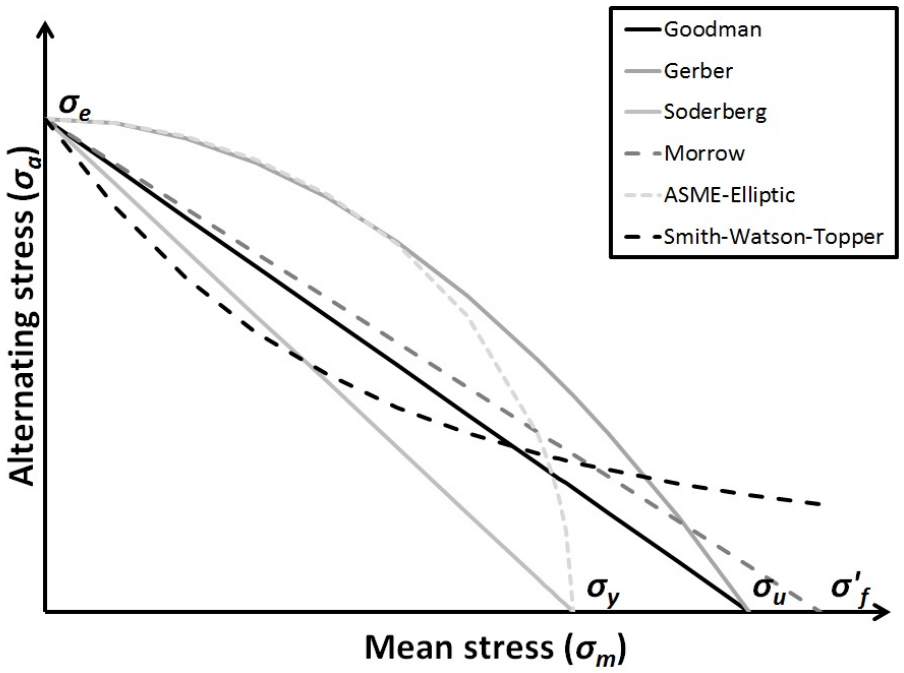

Figure 10. Constant life diagram with six different mean stress equations.

In addition to the equations described above, there are also a number of equations that make use of fitting parameters. The use of these equations requires collecting data at two or more different *R* ratios (i.e. $R = -1$ and at least one other value). The parameters are then adjusted to fit the data.

One such approach was proposed by Stulen in 1965 (14). The Stulen equation is linear in form, like the Goodman, Soderberg, and Morrow equations. However, the slope of the line, *A*, is chosen in order to fit data from multiple stress ratios. This is shown in Equation 9, below.

$$\sigma_{eq} = \sigma_a + A\sigma_m$$

Equation 9. Stulen equation, where:
σ_{eq} = equivalent stress (MPa)
σ_a = alternating stress (MPa)
A = Stulen parameter
σ_m = mean stress (MPa)

Another equation using a fitting parameter was proposed by Walker in 1970 (17). The Walker equation has a similar form to the Smith-Watson-Topper equation, but the exponent γ is chosen to fit the data. If $\gamma = 0.5$, then the Walker equation is equivalent to the Smith-Watson-Topper equation.

$$\sigma_{eq} = \sigma_a^{\gamma}(\sigma_a + \sigma_m)^{1-\gamma}$$

Equation 10. Walker equation, where:
σ_{eq} = equivalent stress (MPa)
σ_a = alternating stress (MPa)
γ = Walker parameter
σ_m = mean stress (MPa)

In the same year, Topper and Sandor proposed a power law equation with a fitting parameter (18). This is shown in Equation 11, below.

$$\sigma_{eq} = \sigma_a + \sigma_m^{\alpha}$$

Equation 11. Topper-Sandor equation, where:
σ_{eq} = equivalent stress (MPa)
σ_a = alternating stress (MPa)
σ_m = mean stress (MPa)
α = Topper-Sandor parameter

The nine equations described above are by no means all of the mean stress equivalence equations that have been proposed over the years. Many more equations have been suggested in the literature (e.g. 12, 13, 19), but are not included here because they are rarely used.

In 2009, Dowling (114) performed a meta-analysis comparing the applicability of the Goodman, Morrow, SWT, and Walker equations. He attempted to fit previously-published fatigue data for 18 steels, 9 aluminums, and one titanium alloy using each of

these four equations. Dowling concluded that the Goodman equation was "highly inaccurate and should not be used." He found that the Morrow equation provided a reasonable fit for the steel data, while the SWT equation provided a good fit for the aluminum data. The Walker equation provided the best fit for all of the data. Dowling attempted to find a relationship between the Walker exponent γ and the tensile strength σ_u. For steels, he found that the Walker exponent γ decreased with increasing tensile strength. For aluminum alloys, he found no such relationship.

The fact that equations such as the Stulen, Walker, and Topper-Sandor equations include fitting parameters which are have different values for different materials suggests that mean stress sensitivity varies between materials. This thought suggests another question: what is the physical basis for mean stress sensitivity in materials?

An indication of an answer to this question may be found in the work of Kirby and Beevers (115), who studied fatigue crack growth in wrought aluminum alloys in air and in vacuum. They found that, in air, the fatigue crack growth rate da/dN was a function of both the stress intensity range ΔK and the stress ratio R. However, in vacuum, da/dN depended only on ΔK. This indicates that stress ratio sensitivity depends on environment as well as material. In 2011, Chawla et al (116) investigated fatigue crack growth in aluminum alloy 7075 in dry air, moisture, and ultra-high vacuum conditions. Unlike Kirby and Beevers, Chawla et al found that da/dN was dependent on R in ultra-high vacuum; however, after correcting for crack deflection, this effect disappeared. They also found that the effect of moisture on the threshold stress intensity range ΔK_{th}

and the critical stress intensity range ΔK_{cr} was significantly greater than that of dry air. Their findings indicate that the formation of oxide on the crack tip plays an important role in stress ratio sensitivity.

1.2.3 EFFECTS OF CASTING DEFECTS IN FATIGUE

One of the first systematic attempts to correlate the radiographic soundness of castings with their mechanical properties was performed by Larson (117). Larson cast test bars of high strength steel with varying degrees of shrinkage porosity by controlling the solidification conditions. He then compared the performance of the cast test bars in tensile tests (yield strength, ultimate tensile strength, ductility, etc.). Larson found that, particularly at high levels of porosity, the effect of porosity on mechanical properties could largely be explained by the reduction in effective cross-section thickness caused by the presence of the porosity. However, Larson only studied the relatively simple case of single-cycle, uniaxial loading. Under uniaxial loading, the stress is distributed uniformly over the cross section, so defects located at or near the surface of the casting and defects located on the interior of the casting will have more or less the same effect on the overall properties. Larson recognized that in bending, torsion, or fatigue, the role of defects located at or near the surface of the casting would be much greater, while the role of defects located on the interior of the casting would be much less.

Five years later, Greenberg (118) applied a fracture mechanics approach to porosity in steel weldments. The interest in this topic was generated by the failure of

welded rocket motor cases. Greenberg critically reviewed the radiographic acceptance standards for welds in the ASME Unfired Pressure Vessel Code and found them inconsistent and inadequate. Using fracture mechanics concepts, Greenberg proposed a new radiographic acceptance standard. His approach was based on treating all defects as semi-elliptical surface flaws. Since it is generally not possible to determine, on the basis of a single radiographic view, whether a given flaw is located on the surface or internal to the casting, and since the stress intensity factor K for a surface flaw is 1.12 times greater than for an internal flaw of equivalent size, this is a conservative approach. Greenberg also made use of concurrent work by Peterson (29) to determine the minimum allowable distance between flaws. He developed a curve to determine the critical ligament between flaws of a given size. Flaws closer together than the critical ligament would be rejected. This approach is extremely over-conservative, since it assumes that the flaws are located in the same plane. The true three-dimensional distance between two flaws in a casting or weldment may be many times greater than the two-dimensional distance measured in a radiographic view. While Greenberg's work was concerned with porosity in weldments subject to single-cycle loading, he noted that the methodology could also be used for castings.

Kohno and Makioka (119) conducted a detailed study of the effect of casting defects on the fatigue strength of chromium stainless steel. However, they did not make use of fatigue fracture mechanics concepts as suggested by Greenberg; instead, they employed a more traditional stress-based approach to fatigue. Thus, rather than treating a casting defect as an equivalent semielliptical flaw and solving the appropriate fracture

mechanics equations, they treated a casting defect as an equivalent notch, and compared their experimentally-obtained *S*-*N* curves for specimens with casting defects to an experimentally obtained *S*-*N* curve for sound specimens to determine fatigue notch coefficients for defects of various sizes and types. Also, unlike the previous authors, who used radiography as a non-destructive testing method, Kohno and Makioka employed magnetic particle testing. This meant that they were only able to detect defects located at or very near the surface of the casting. However, for the reasons mentioned by Larson in the previously-cited reference, surface defects play a predominant role in fatigue, and, in fact, for all of the specimens tested by Kohno and Makioka, fatigue failure was observed to originate from surface defects. In all cases, fatigue cracks were found to originate from shrinkage porosity or surface cracks. Gas porosity up to 5 mm in diameter was found to have no effect on fatigue strength. Based on their results, Kohno and Makioka recommended using a fatigue notch factor of 1.5 for shrinkage porosity up to 3 mm^2 in area, and 2.0 for surface cracks or shrinkage porosity over 3 mm^2 in area. These suggested fatigue notch factors were based on an empirical correlation with their experimental results, rather than a rigorous theoretical analysis.

In the early 1980s, the British Investment Casting Trade Association and the National Engineering Laboratory of the United Kingdom collaborated in a large scale research and development effort focused on improving the fatigue behavior of high strength steel investment castings. This research included a study on the influence of casting defects on fatigue behavior. McCallum and Lang (120) summarized the findings of this study at the 6^{th} World Conference on Investment Casting. McCallum and Lang

tested a large number of investment cast specimens in fatigue. Using scanning electron microscopy (SEM), they located and characterized the defects from which the fracture originated. Using the measured flaw size a, the applied stress range $\Delta\sigma$, and a geometric factor based on the shape of the defect, they calculated a fictitious stress intensity range ΔK corresponding to the observed defect. They then plotted ΔK versus the number of cycles to failure N, and found that this reduced scatter compared to an S-N curve constructed without reference to defect size. From this, they were able to determine what they termed the threshold stress intensity range ΔK_{th} (or, more properly, the endurance limit σ_e, adjusted for the defect size). They did not make any measurements of the fatigue crack growth rate da/dN, and it could certainly be argued that they misappropriated terminology from fatigue fracture mechanics to describe what was, in essence, a stress-based approach devoid of any actual fracture mechanics. Nevertheless, the values determined for ΔK_{th} for investment cast high strength steels agreed closely with reported values of ΔK_{th} for equivalent wrought alloys.

Another joint research and development program concerning the fatigue behavior of steel castings was carried out in Germany in the early 1990s by Heuler et al (121). Test specimens removed from large steel castings were examined using magnetic particle, ultrasonic, and radiographic means. The test specimens were then subjected to cyclic loading, while undergoing real-time ultrasonic inspection. As soon as crack initiation and growth was detected by the ultrasonic inspection apparatus, the cyclic loading test was halted. The test specimen was then removed from the testing apparatus, cooled to cryogenic temperatures, and broken open. The fracture surface was then

observed using optical microscopy. This procedure was carried out on a total of 385 test specimens. Heuler, Berger, and Motz then analyzed the results using two different approaches: a local strain approach and a fracture mechanics approach. The local strain approach was similar in some respects to the stress-based approach used by Kohno and Makioka. However, Heuler et al used a much more rigorous theoretical approach to derive values for the fatigue notch coefficient, modeling a defect as a three-dimensional ellipsoid of rotation. In the fracture mechanics approach, they made use of a strain-based stress intensity factor ΔK as well as a cyclic J-integral in order to take plastic strains into account. Like McCallum and Lang, they determined the threshold stress intensity range ΔK_{th}. In examining the fracture surfaces, however, they found that many defects with stress intensity ranges greater than ΔK_{th} did not actually initiate cracks. They concluded that the strain-based approach, which considers crack initiation as the critical step in determining fatigue life, was more accurate than the fracture mechanics approach, which assumes that all flaws whose stress intensity factor exceeds ΔK_{th} immediately initiate cracks, and that crack propogation is the critical step in determining fatigue life. They found, however, that the fracture mechanics approach gave accurate results for defects that displayed crack growth greater than 1 mm. Thus, the strain-based approach could be used for the initial stage of fatigue comprising crack initiation, while the fracture mechanics approach could be used for the second stage of fatigue comprising crack propagation.

A recent article by Hardin (32) presents an example of the use of strain-based fatigue life concepts, along with modern casting simulation software, in the design of a

cast steel component. Hardin prepared cast test bars of 8630 steel with varying degrees of shrinkage porosity. Two orthogonal radiographic exposures were prepared of each of the specimens, in order to obtain an estimate of the three-dimensional distribution of porosity in each specimen. This was used to calculate the "lost" cross-section thickness in each specimen (thus harkening back to the early work of Larson, who found that the effect of porosity on mechanical properties could largely be explained by the reduction in effective cross-section thickness). Hardin then calculated a fatigue notch coefficient, using a handbook value for a spherical hole in a cylindrical bar and treating the maximum "lost" cross-section thickness as the diameter the sphere. He found that the fatigue notch coefficient thus determined correlated relatively well with the empirically determined fatigue notch coefficient from the experimental *S-N* curve when the specimens were tested in fatigue. This method of calculating the fatigue notch coefficient based on the "lost" cross-section thickness was then applied to the design of a cast component. Solidification simulation software was employed to predict the size and location of shrinkage porosity in the component. This result was then fed into the fatigue package of a finite element stress analysis program. Local fatigue notch coefficients based on the "lost" cross-section thickness could then be used to predict the fatigue life of the component. The predictions were accurate within one order of magnitude.

Wang and Apelian (122, 123) performed a study of the effects of porosity on the fatigue of sand cast aluminum alloy A356-T6. They produced "pore-free" specimens by means of hot isostatic pressing (HIP), and compared the fatigue behavior of the "pore-free" specimens to that of specimens containing pores. They also investigated the effect

of dendrite arm spacing (DAS). They found that the fatigue lives of castings containing porosity were at least one order of magnitude shorter than those without porosity. A critical pore size (approximately 25 – 30 μm) was identified, below which fatigue cracks initiated from microstructural features or slip bands, rather than pores. Fatigue life was found to decrease with increasing DAS for unmodified alloys. For strontium-modified alloys, fatigue life decreased with increasing DAS up to 60 μm; for DAS > 60 μm, the fatigue life was found to increase with increasing DAS.

Gao et al (124) found that fatigue lives in permanent mold cast A356-T6 were determined by the size of pores as well as their distance from the specimen surface. They imported the geometry of actual pores, as observed in metallographic sections, into a two-dimensional elastic-plastic finite element model. They used a local mesh refinement technique in order to predict the local plastic strains around the defects. Based on this, they developed a parametric model relating fatigue life to the defect size, distance from the surface, three geometric stress concentration factors, stress amplitude, and an additional fitting parameter.

In 2013, Tijani et al (31) described a similar parametric model for porosity effects in the fatigue of aluminum alloy A356. However, Tijani's model was based on a three-dimensional finite element model, rather than the two-dimensional model of Gao et al. Parameters included in Tijani's model include the pore diameter, volume, and area (used together to create a measure of pore roundness that describes the difference in the pore shape from a perfect sphere), the distance from the surface, and a notch sensitivity factor.

X-ray computed tomography was used to measure the actual three-dimensional size and shape of defects in cast test bars. The bars were then tested in fatigue. The fatigue strength predicted by the model was found to be within 5% of the actual strength.

While Tijani's results are impressive, at the present time, the routine use of x-ray computed tomography to characterize defects in commercial castings is impractical. Therefore, other authors have applied a statistical approach. The use of extreme value statistics to evaluate the effect of defects on fatigue was pioneered by Murakami and Endo (125), who used it to determine the effect of inclusions on the fatigue life of steels. Recently, this method has been used by Kočená et al (33) to determine the effect of pore size on aluminum alloy A356. In this method, metallographic sections are used to measure the distribution of pore sizes in a casting. Extreme value statistics are then used to predict the largest pore size (which is typically significantly larger than the largest pore actually observed in the specimen).

It can be imagined that, in the future, a stochastic model might be developed, whereby multiple Monte Carlo casting simulations would be performed in order to predict a range of possible defect sizes and shapes for a given casting poured under given conditions. Finite-element analysis would then be performed on each of the predicted defect distributions in order to predict an expected range of fatigue lives. However, neither the computational power nor the detailed understanding of defect formation in castings that would be needed to create such a tool is in existence at the present time.

1.2.4 ALUMINUM ALLOY 356

Aluminum alloys 356 and A356 are among the most widely-used and widely-studied aluminum-silicon casting alloys. The composition of the two alloys, as registered with the Aluminum Association (126), are given in Table 1, below.

Table 1. Composition of aluminum alloys 356 and A356

Alloy	Si	Fe	Cu	Mn	Mg	Zn	Ti	Others (each)	Others (total)	Al
356.0	6.5 – 7.5	0.6 max.	0.25 max.	0.35 max.	0.20 – 0.45	0.35 max.	0.25 max.	0.05 max.	0.15 max.	Balance
A356.0	6.5 – 7.5	0.20 max.	0.20 max.	0.10 max.	0.20 – 0.45	0.10 max.	0.20 max.	0.05 max.	0.15 max.	Balance

As Table 1 shows, both alloys consist of aluminum with 6.5 – 7.5% silicon and 0.20 – 0.45% magnesium. However, A356 has tighter limits on other elements, especially iron. The lower limit on iron reduces the formation of Al-Fe intermetallics, which have a detrimental effect on mechanical properties (74).

The as-cast microstructure of these alloys consists primarily of dendrites of α-aluminum containing silicon and magnesium in solid solution, surrounded by eutectic aluminum-silicon. The Al-Si eutectic takes the form of coarse platelets, unless a modifier such as strontium, sodium, or antimony is added. Small additions of these elements (at the parts-per-million level) change the morphology of the Al-Si eutectic to a fine fibrous structure. The as-cast microstructure also includes particles of Mg_2Si within the α-Al matrix. In addition, smaller quantities of various Al-Fe and Al-Cu intermetallics may be present. The detrimental effect of Al-Fe intermetallics, especially β-Al_5SiFe, on

mechanical properties has already been mentioned. Al-Cu intermetallics are often to be considered to be beneficial for mechanical properties, but detrimental for corrosion resistance, due to the formation of localized galvanic cells.

The alloys 356 and A356 are rarely, if ever, used in the as-cast condition. Instead, they are heat treated in order to achieve precipitation hardening. The castings are solution heat treated at a temperature of 520 – 550ºC for 6 – 12 hours. This results in dissolution of Mg_2Si and other intermetallic compounds, as well as spheroidization of eutectic silicon. The castings are then quenched in water, in order to keep the Mg in solid solution. Next, the castings are artificially aged at an elevated temperature in order to allow precipitation of Mg_2Si in a controlled fashion. Initially, clusters of Mg and Si atoms known as Gunier-Preston zones form. Next, a needle-like precipitate (β''-Mg_5Si_6) forms. This phase is associated with peak strength. With increased aging temperature and/or time, rod-like β'-$MgSi_2$ forms, followed by platelets of β-$MgSi_2$. Continued aging results in coarsening of the β-$MgSi_2$ phase.

Aging for peak strength is designated the T6 condition, and typically involves temperatures of 150 – 180ºC for 2 – 5 hours. Alternatively, castings may be aged at a somewhat higher temperature and/or for a slightly longer time for greater dimensional stability; this is known as condition T7.

Published mechanical properties for aluminum alloys 356 and A356, in conditions T6 and T7, cast by various processes including lost foam, are given in Table 2, on the

following page. As Table 2 shows, A356 generally has somewhat improved properties compared to 356. For example, Wang et al (133) found that lost foam cast A356 had approximately 5% higher yield strength, 10% higher tensile strength, 5% greater fatigue strength, and 240% greater elongation than lost foam cast 356. The T7 heat treatment generally results in a decrease in yield strength and tensile strength in exchange for greater ductility; however, for sand cast 356, the opposite effect has been reported (134). Of the various casting methods shown in Table 3 (lost foam casting, sand casting, permanent mold casting, semi-solid casting, and squeeze casting), lost foam castings have the lowest ductility (0.5 – 3.0%) and fatigue strength (56.7 – 67.7 MPa).

Table 2. Mechanical properties of 356 and A356 cast by various processes

Alloy	Condition	Casting method	Yield strength (MPa)	Tensile strength (MPa)	Elongation	Fatigue strength at 10^7 cycles (MPa)	Notes	Reference
356	T6	Lost foam	207	222	0.5%	64.4		133
A356	T6	Lost foam	215	245	1.2%	67.7		133
A356	T6	Lost foam	-	-	-	56.7		126
A356	T6	Lost foam	240	255	1.2%	-		128
A356	T6	Lost foam	-	232	3.0%	-		132
A356	T6	Lost foam	-	252	3.3%	-	Low pressure process	132
A356	T6	Lost foam	-	261	6.2%	-	Ceramic shell process	132
A356	T6	Lost foam	-	278	8.1%	-	Low pressure ceramic shell process	132
A356	T6	Lost foam	-	-	-	75.0	Liquid hot isostatic pressed	126
356	T6	Sand cast	165	228	3.5%	-		134
356	T7	Sand cast	207	234	2.0%	-		134
A356	T6	Sand cast	212	256	3.9%	71.7		126, 127
A356	T7	Sand cast	144	199	11%	-		129
356	T6	Permanent mold	186	262	5.0%	90		134
356	T7	Permanent mold	165	221	6.0%	76		134
A356	T6	Permanent mold	250	305	7.7%	112.1		126, 127
A356	T6	Permanent mold	234	298	8%	111		130
A356	T7	Permanent mold	257	299	9.9%	-		131
A356	T6	Semi-solid cast	267	321	15%	135		130
A356	T6	Squeeze cast	267	335	12%	130		130

1.3 RESEARCH OBJECTIVES AND SCOPE

In spite of the tremendous volume of research that has been done on lost foam casting over the past several decades, there is no published work on the effect of as-cast surface on the fatigue of lost foam cast aluminum. In the early 1990s, Littleton et al studied the effect of as-cast surface on lost foam ductile iron (21) and gray iron (23) castings. A significant reduction in fatigue strength with as-cast surface was found for ductile iron, but not for gray iron. In the 1995 summary report of the DOE-AFS-Lost Foam Consortium (22), it was stated that fatigue testing would also be performed on lost foam aluminum alloy 356-T6. However, the results of this testing were never published. Since 1995, a number of studies of the fatigue properties of lost foam cast aluminum alloy 356 have been published, but none that incorporated the effects of as-cast surface.

Furthermore, the fatigue specimens used by Littleton et al were cast cylinders. As discussed by Littleton et al, the cast specimens tended to distort during solidification. Thus, the straightness of the as-cast specimens was less than that of the machined specimens. This meant that the as-cast specimens were subjected to bending moments, which the machined specimens were not subjected to. Littleton et al mention this as a possible source of error.

Also, there is very little published work on fatigue of aluminum LFCs that incorporates stress ratio effects. As discussed above, there are more than a dozen mean stress correction equations in existence, several of which (e.g. the Stulen, Topper-Sandor,

and Walker equations) incorporate a material-dependent term which reflects stress ratio sensitivity. Thus, there is a need for data on the stress ratio sensitivity of lost foam cast aluminum alloy 356.

The primary motivation of the present work is to provide mechanical property data on aluminum LFCs for use by designers. A secondary motivation is to understand the factors that influence the fatigue behavior of aluminum LFCs, in order to determine possible ways of improving their properties. A third motivation is to gain insight into the nature and origins of stress ratio sensitivity in materials.

The objectives of this work are as follows:

(1.) Determine the monotonic tensile properties (yield strength, tensile strength, and elongation) of lost foam cast aluminum alloy 356-T6 and 356-T7 with as-cast and machined surface

(2.) Generate *S-N* curves (R=-1) for lost foam cast aluminum alloy 356-T6 and 356-T7 with as-cast and machined surface

(3.) Determine which mean stress correction equation (Goodman, Soderberg, Morrow, Gerber, ASME-Elliptic, Smith-Watson-Topper, Stulen, Topper-Sandor, or Walker) is best suited for lost foam cast aluminum alloy 356-T6 and 356-T7 with R>-1

(4.) Evaluate the effect of defect size on the fatigue life of lost foam cast aluminum alloy 356-T6 and 356-T7 under R=-1 and R>-1 conditions

In the following chapter, the methodology employed to answer these questions will be detailed.

CHAPTER 2 – METHODOLOGY

2.1 SAMPLE PREPARATION

A total of eight sets of specimens were prepared:

- 356-T6 tensile test specimens with machined surface (12 pieces)
- 356-T6 fatigue test specimens with machined surface (60 pieces)
- 356-T7 tensile test specimens with machined surface (12 pieces)
- 356-T7 fatigue test specimens with machined surface (45 pieces)
- 356-T6 tensile test specimens with as-cast surface (12 pieces)
- 356-T6 fatigue test specimens with as-cast surface (40 pieces)
- 356-T7 tensile test specimens with as-cast surface (12 pieces)
- 356-T7 fatigue test specimens with as-cast surface (40 pieces)

All of the specimens were poured and heat treated at BRP-Spruce Pine, and machined at BRP-Waukegan. The preparation of the specimens is detailed below.

2.1.1 MACHINED SURFACE SPECIMENS

Foam cylinders, measuring 9 mm in diameter and 100 mm in length, were cut out from a sheet of extruded polystyrene foam with an approximate density of 32 kg/m^3. The foam cylinders were glued to a molded EPS gating system as shown in Figure 11, below.

The patterns were glued to the cluster using a hot-melt EVA adhesive, with 14 specimens per cluster.

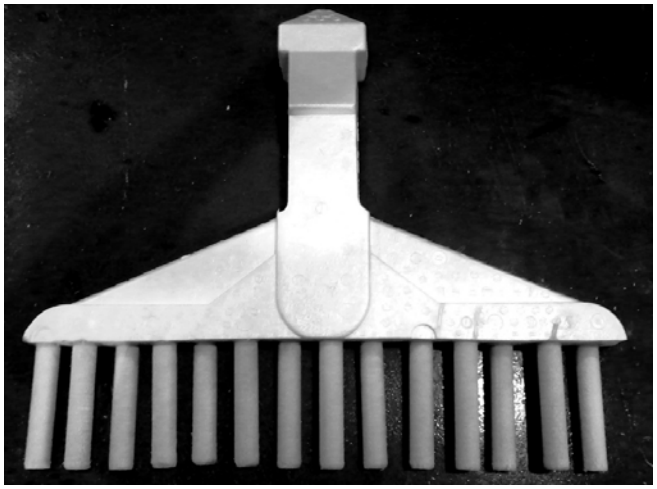

Figure 11. Mold setup for machined surface specimens.

The clusters were coated and placed in a flask, which was filled with sand. Aluminum alloy 356 was poured into the molds at a temperature of 830°C. The solidified castings were removed from the flask and quenched in water. The cast specimens were removed from the cluster using a band saw.

The specimens were solutionized at 539°C for 10 hours, then quenched in 65°C water. The T6 specimens were aged at 177°C for 5.5 hours and air cooled. The T7 specimens were aged by heating to a temperature of 150°C and holding for 1.5 hours, then ramping to a temperature of 205°C and holding for 6 hours, followed by air cooling.

The specimens were then sent to BRP-Waukegan for machining. The tensile test bars were machined to the dimensions shown in Figure 12, below. The fatigue test specimens were machined to the dimensions shown in Figure 13, below. The constant-

radius geometry of ASTM E466 (135) was used. This geometry was chosen to avoid any stress concentration at the transition between the grips and the gage length.

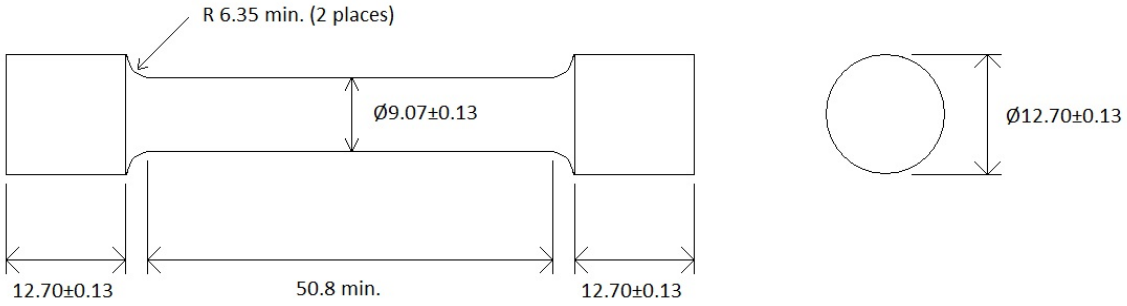

Figure 12. Tensile test specimen with machined surface. All dimensions in mm.

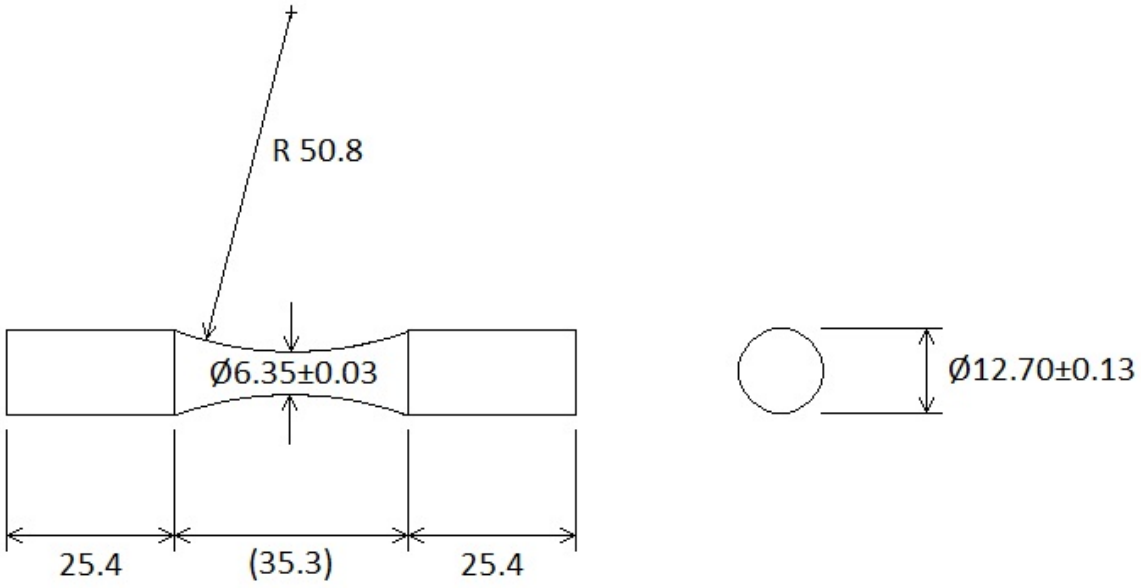

Figure 13. Fatigue test specimen with machined surface. All dimensions in mm.

2.1.2 CAST SURFACE SPECIMENS

For the cast surface specimens, an existing foam tool was used to produce a rectangular EPS pattern measuring approximately 432 mm × 305 mm × 19 mm. The

permeability of 12 patterns was measured, using the UAB pattern fusion tester (26). The permeability was measured in 18 different locations on each rectangular pattern (9 locations on each side). The average pattern permeability was 4.3 cm/s, with a standard deviation of 2.1 cm/s. A histogram of the results is shown in Figure 14, below.

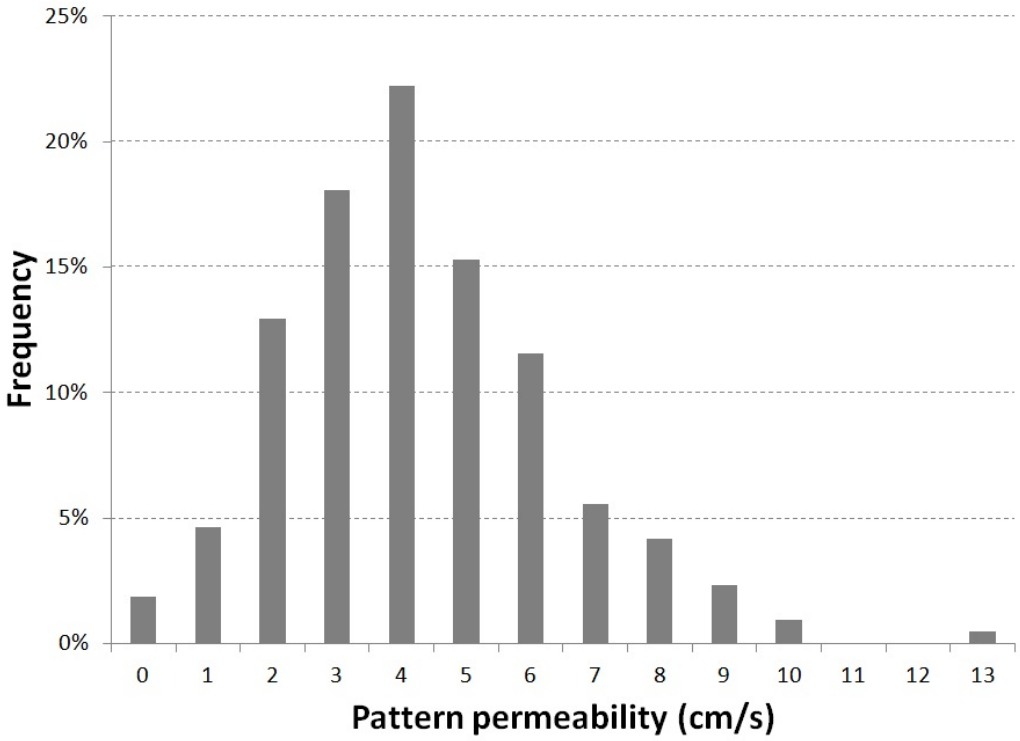

Figure 14. Histogram of pattern permeability for cast surface specimens.

The patterns were attached to a foam cluster, and were poured and heat treated as described above for the machined surface specimens. The specimens were then sent to BRP-Waukegan, where they were machined to the dimensions shown in Figures 15 and 16, below.

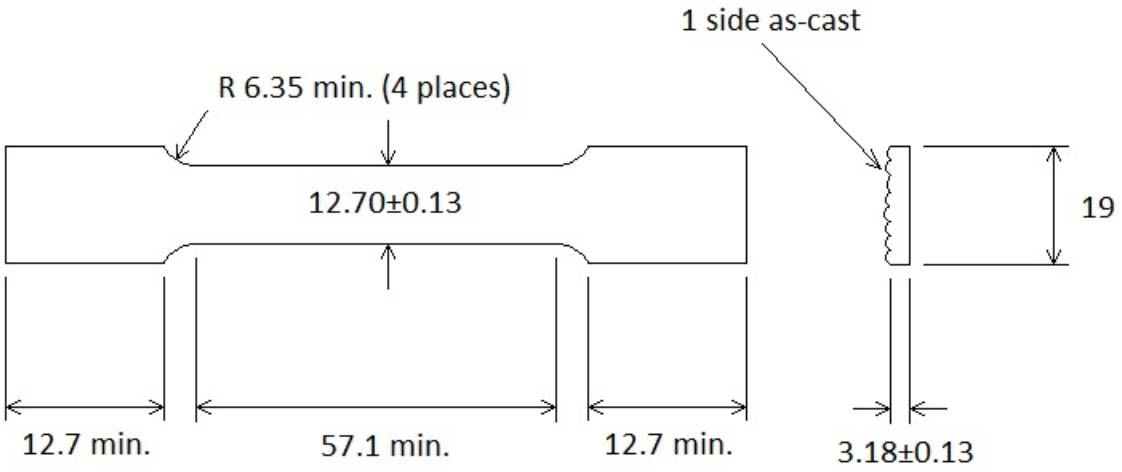

Figure 15. Tensile test specimen with as-cast surface. All dimensions in mm.

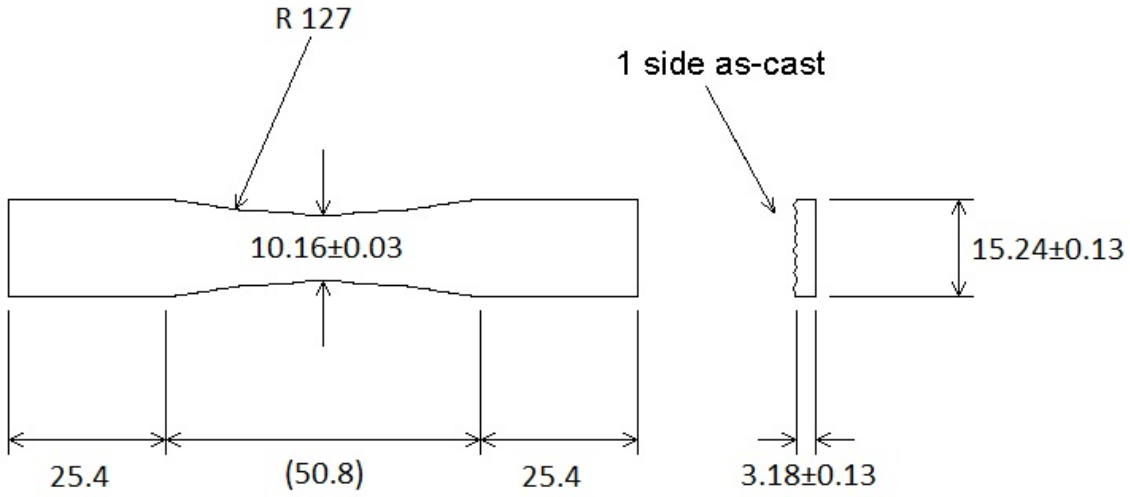

Figure 16. Fatigue test specimen with as-cast surface. All dimensions in mm.

It was decided to make use of flat specimens, with one as-cast, in order to better control the straightness of the specimens. Littleton et al (23), who used fully-cast specimens, identified dimensional variability of the castings as a possible source of error. By machining all but one side of the specimen, tighter dimensional tolerances could be maintained.

2.2 TENSILE TESTING

Five tensile test specimens from each of the four groups (356-T6 machined, 356-T6 as-cast, 356-T7 machined, and 356-T7 as-cast) were tested in accordance with ASTM E8. The tensile tests were performed using an MTS load frame, with a Model 661 load cell and Model 647 hydraulic wedge grips. The specimens were tested at a constant displacement rate of 5 mm per minute. Specimen deflection was measured using an extensometer.

2.3 FATIGUE TESTING

Fatigue testing was performed according to ASTM E466 using the previously described MTS load frame. Testing was performed in load control. Strain control was considered, but it was decided that a cyclic stress-strain curve for the specimen as a whole would be unrepresentative of the local strain around a casting defect. A sinusoidal load frequency of 10 Hz was used.

2.4 SCANNING ELECTRON MICROSCOPY

Fractured specimens were observed using a Hitachi S-2460N scanning electron microscope, with an accelerating voltage of 25 keV. Fatigue striations were used to locate the casting defect from which the fatigue fracture appeared to initiate. Defect

areas were measured using ImageJ software, a Java-based open source image processing application developed by the National Institutes of Health.

CHAPTER 3 – RESULTS

3.1 TENSILE TESTING RESULTS

Tables 3 – 6 show the tensile modulus, yield strength, tensile strength, elongation, and quality index for the machined-surface 356-T6, machined-surface 356-T7, as-cast 356-T6, and as-cast 356-T7 specimens, respectively. The quality index first proposed by Drouzy, Jacob, and Richard (136) was used, calculated according to Equation x, below. The purpose of the quality index is to provide a single metric for both tensile strength and elongation. Representative stress-strain curves are shown in Figures 17 – 20.

$$Q = \sigma_u + 150 \log \varepsilon_f$$

Equation 12. Drouzy-Jacob-Richard equation for quality index, where:
Q = quality index (MPa)
σ_u = ultimate tensile strength (MPa)
ε_f = elongation at fracture

Table 3. Monotonic properties of lost foam 356-T6 with machined surface

Specimen	Tensile modulus, GPa	Yield strength, MPa	Tensile strength, MPa	Elongation	Quality index, MPa
1	69.6	253	300	1.94%	343
2	70.5	251	299	2.40%	356
3	68.8	253	297	2.01%	343
4	69.9	250	289	1.56%	318
5	68.7	243	291	2.23%	343
Average	69.5	250	295	2.03%	340
Standard Deviation	0.8	4	5	0.32%	14

Table 4. Monotonic properties of lost foam 356-T7 with machined surface

Specimen	Tensile modulus, GPa	Yield strength, MPa	Tensile strength, MPa	Elongation	Quality index, MPa
1	69.4	252	280	1.39%	302
2	69.7	263	281	1.12%	288
3	70.1	256	278	1.27%	293
4	69.4	261	284	1.48%	309
5	70.4	251	276	1.31%	294
Average	69.8	257	280	1.31%	297
Standard Deviation	0.4	5	3	0.14%	8

Table 5. Monotonic properties of lost foam 356-T6 with as-cast surface

Specimen	Tensile modulus, GPa	Yield strength, MPa	Tensile strength, MPa	Elongation	Quality index, MPa
1	69.5	243	243	0.51%	199
2	64.3	242	244	0.61%	212
3	66.1	228	228	0.56%	191
4	66.3	240	241	0.56%	203
5	66.6	238	238	0.57%	201
Average	66.5	238	239	0.56%	201
Standard Deviation	1.9	6	6	0.04%	8

Table 6. Monotonic properties of lost foam 356-T7 with as-cast surface

Specimen	Tensile modulus, GPa	Yield strength, MPa	Tensile strength, MPa	Elongation	Quality index, MPa
1	67.8	234	235	0.56%	197
2	70.0	228	228	0.52%	186
3	68.5	228	229	0.56%	191
4	68.8	232	243	0.71%	221
5	66.1	228	238	0.70%	215
Average	68.2	230	235	0.62%	202
Standard Deviation	1.4	3	6	0.10%	15

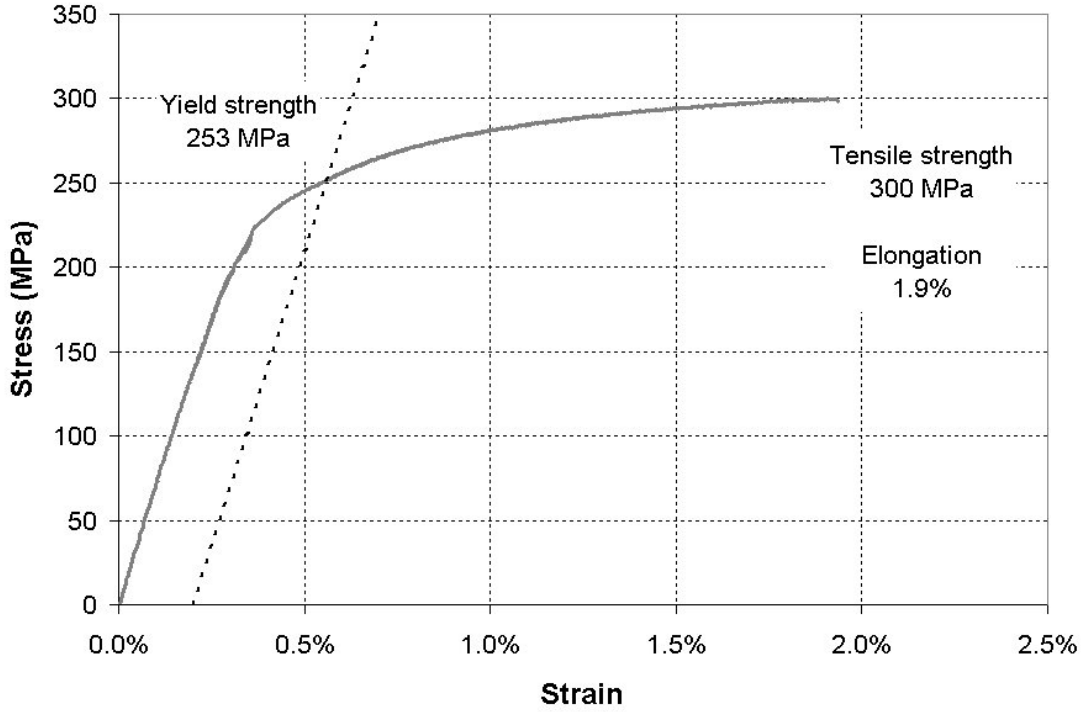

Figure 17. Stress-strain curve for 356-T6 with machined surface.

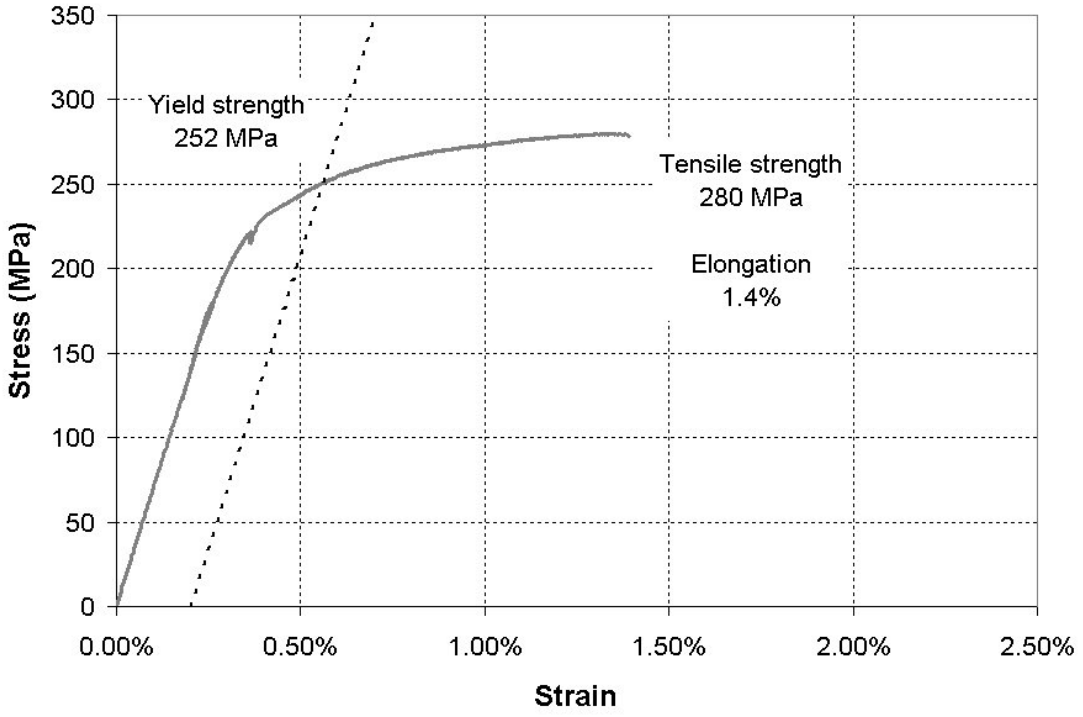

Figure 18. Stress-strain curve for 356-T7 with machined surface.

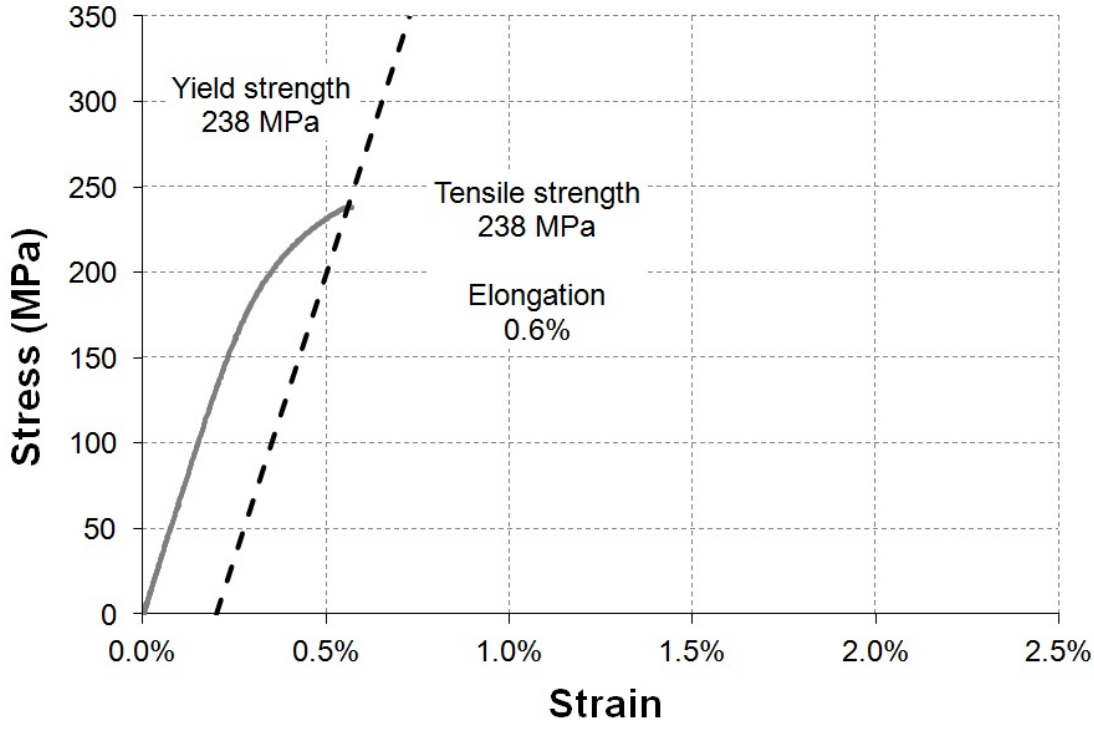

Figure 19. Stress-strain curve for 356-T6 with as-cast surface.

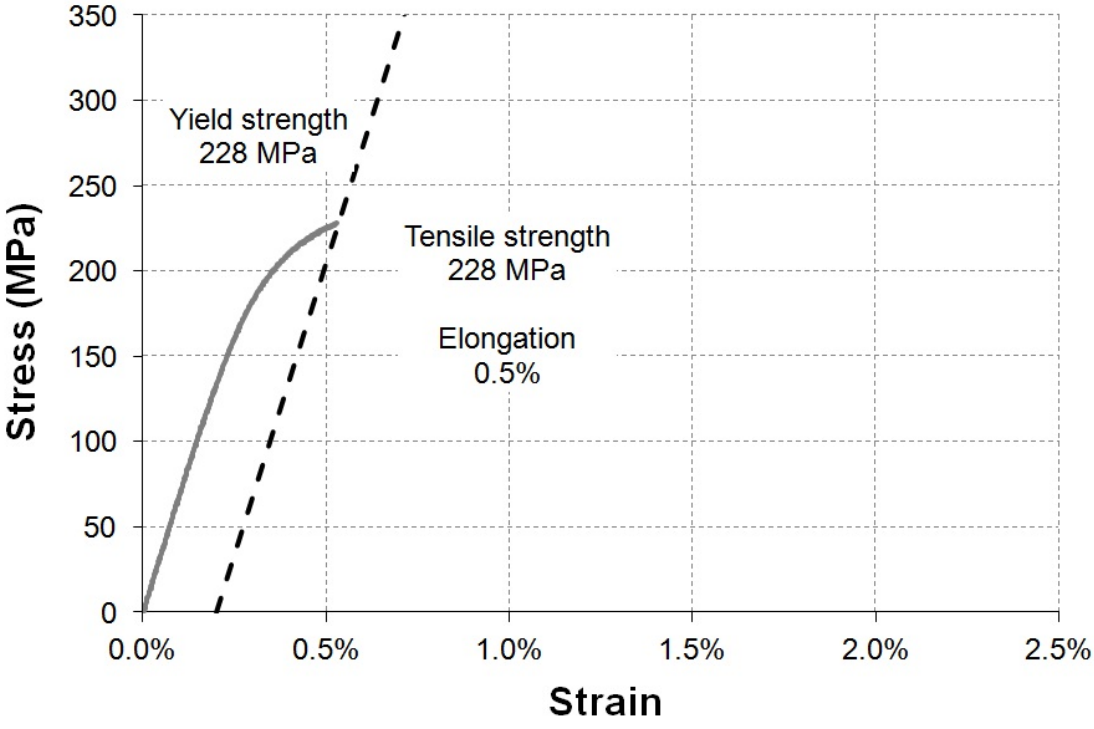

Figure 20. Stress-strain curve for 356-T7 with as-cast surface.

3.2 FATIGUE TESTING RESULTS

Fatigue testing results for machined-surface 356-T6, machined-surface 356-T7, as-cast 356-T6, and as-cast 356-T7 specimens are shown in Tables 7 – 10. For each specimen, the minimum and maximum load, alternating and mean stress, and cycles to failure are shown. In addition, for the as-cast samples, the specimen thickness is shown. This is due to the fact that thickness varied slightly from specimen to specimen.

On the basis of the $R = -1$ data for each group of specimens, a linear least-squares fit of log stress vs. log reversals was used to determine the Basquin parameters σ_f' and b. This was used to plot an *S*-*N* curve for each group. The *S*-*N* curves are shown in Figures 21 – 24.

Table 7. Cycles to failure for lost foam 356-T6 with machined surface

R	Minimum load (N)	Maximum load (N)	Alternating stress (MPa)	Mean stress (MPa)	Cycles to failure
-1	-2887	2887	91.2	0	489,096
-1	-2887	2887	91.2	0	440,237
-1	-2887	2887	91.2	0	226,309
-1	-2887	2887	91.2	0	234,121
-1	-2562	2562	80.9	0	1,031,085
-1	-2562	2562	80.9	0	437,409
-1	-2562	2562	80.9	0	404,262
-1	-2562	2562	80.9	0	504,488
-1	-2562	2562	80.9	0	261,898
-1	-2562	2562	80.9	0	462,649
-1	-2349	2349	74.2	0	628,000
-1	-2349	2349	74.2	0	850,293
-1	-2349	2349	74.2	0	553,584
-1	-2349	2349	74.2	0	821,440
-1	-2282	2282	72.1	0	752,949
-1	-2282	2282	72.1	0	940,302
-1	-2282	2282	72.1	0	532,142
-1	-2282	2282	72.1	0	843,923
-1	-2282	2282	72.1	0	508,404
-1	-2282	2282	72.1	0	803,783
-1	-2211	2211	69.8	0	955,962
-1	-2211	2211	69.8	0	786,416
-1	-2211	2211	69.8	0	734,506
-1	-2211	2211	69.8	0	723,837
-1	-2117	2117	66.9	0	812,777
-1	-2117	2117	66.9	0	1,158,579
-1	-2117	2117	66.9	0	1,675,776
0	0	4230	66.8	66.8	202,239
0	0	4230	66.8	66.8	135,864
0	0	3759	59.3	59.3	366,497
0	0	3759	59.3	59.3	395,475
0	0	3759	59.3	59.3	283,696
0	0	3443	54.4	54.4	384,069
0	0	3443	54.4	54.4	424,776
0	0	3345	52.8	52.8	470,594
0	0	3345	52.8	52.8	378,667
0	0	3345	52.8	52.8	338,151
0	0	3238	51.1	51.1	461,822
0	0	3238	51.1	51.1	481,782
0	0	2891	45.6	45.6	796,653
0	0	2891	45.6	45.6	871,396
0.09	383	4448	64.2	76.3	280,705
0.09	383	4448	64.2	76.3	176,107
0.26	1170	4448	51.8	88.7	296,894
0.26	1170	4448	51.8	88.7	343,288
0.26	1170	4448	51.8	88.7	256,863
0.37	1650	4448	44.2	96.3	391,778
0.37	1650	4448	44.2	96.3	590,600
0.40	1788	4448	42.0	98.5	555,037
0.40	1788	4448	42.0	98.5	621,528
0.40	1788	4448	42.0	98.5	674,470
0.44	1939	4448	39.6	100.8	630,037
0.44	1939	4448	39.6	100.8	580,154
0.62	2749	4448	26.8	113.6	5,026,118
0.62	2749	4448	26.8	113.6	3,381,193

Table 8. Cycles to failure for lost foam 356-T6 with as-cast surface

R	Minimum load (N)	Maximum load (N)	Thickness (mm)	Alternating stress (MPa)	Mean stress (MPa)	Cycles to failure
-1	-2291	2291	3.07	73	0	271,370
-1	-2291	2291	3.10	73	0	829,255
-1	-2068	2068	3.10	66	0	778,085
-1	-2068	2068	3.10	66	0	376,818
-1	-2068	2068	3.10	66	0	859,634
-1	-1922	1922	2.87	66	0	494,665
-1	-1922	1922	2.97	64	0	510,187
-1	-1699	1699	3.00	56	0	1,379,271
-1	-1699	1699	3.10	54	0	662,367
-1	-1699	1699	3.10	54	0	1,421,965
-1	-1584	1584	2.87	54	0	1,550,589
-1	-1584	1584	3.00	52	0	2,056,254
0	0	3354	3.05	54	54	226,313
0	0	3354	3.15	52	52	220,236
0	0	3029	3.02	49	49	537,623
0	0	3029	3.00	50	50	257,484
0	0	3029	3.12	48	48	298,635
0	0	2811	3.10	45	45	288,027
0	0	2811	3.12	44	44	306,850
0	0	2487	2.97	41	41	1,210,621
0	0	2487	3.10	39	39	451,319
0	0	2487	2.95	42	42	959,461
0	0	2322	3.00	38	38	1,570,361
0	0	2322	3.15	36	36	942,849
0.09	316	3532	3.02	52	63	425,327
0.09	316	3532	3.05	52	62	101,433
0.09	316	3532	3.07	51	62	180,438
0.26	930	3576	2.95	44	75	250,808
0.26	930	3576	2.92	45	76	192,455
0.26	930	3576	3.10	42	72	365,086
0.31	1139	3625	2.90	42	81	300,408
0.31	1139	3625	3.05	40	77	386,571
0.40	1317	3296	3.12	31	73	850,922
0.40	1317	3296	2.90	34	78	359,927
0.40	1317	3296	3.05	32	74	528,929
0.44	1406	3198	3.05	29	74	2,496,331

Table 9. Cycles to failure for lost foam 356-T7 with machined surface

R	Minimum load (N)	Maximum load (N)	Alternating stress (MPa)	Mean stress (MPa)	Cycles to failure
-1	-2309	2309	72.9	0.0	507,983
-1	-2309	2309	72.9	0.0	706,328
-1	-2051	2051	64.8	0.0	781,135
-1	-2051	2051	64.8	0.0	973,398
-1	-2051	2051	64.8	0.0	1,064,794
-1	-1873	1873	59.1	0.0	1,134,085
-1	-1873	1873	59.1	0.0	1,242,026
-1	-1824	1824	57.6	0.0	1,624,498
-1	-1824	1824	57.6	0.0	1,099,743
-1	-1824	1824	57.6	0.0	1,525,232
-1	-1770	1770	55.9	0.0	2,042,982
-1	-1770	1770	55.9	0.0	1,709,903
-1	-1695	1695	53.5	0.0	2,367,266
-1	-1695	1695	53.5	0.0	1,610,684
-1	-1695	1695	53.5	0.0	1,578,487
0	0	3385	53.4	53.4	559,273
0	0	3385	53.4	53.4	461,839
0	0	3007	47.5	47.5	1,005,070
0	0	3007	47.5	47.5	947,782
0	0	3007	47.5	47.5	684,971
0	0	2753	43.5	43.5	1,034,306
0	0	2753	43.5	43.5	846,376
0	0	2678	42.3	42.3	1,674,938
0	0	2678	42.3	42.3	809,932
0	0	2678	42.3	42.3	873,339
0	0	2589	40.9	40.9	1,781,136
0	0	2589	40.9	40.9	1,178,452
0	0	2313	36.5	36.5	1,694,084
0	0	2313	36.5	36.5	2,286,468
0	0	2313	36.5	36.5	3,566,207
0.09	307	3559	51.3	61.0	414,472
0.09	307	3559	51.3	61.0	358,191
0.26	934	3559	41.4	70.9	880,352
0.26	934	3559	41.4	70.9	819,491
0.26	934	3559	41.4	70.9	1,417,558
0.37	1321	3559	35.3	77.0	1,129,332
0.37	1321	3559	35.3	77.0	1,008,951
0.40	1432	3559	33.6	78.8	848,269
0.40	1432	3559	33.6	78.8	1,298,928
0.44	1552	3559	31.7	80.7	1,295,199
0.44	1552	3559	31.7	80.7	1,567,027
0.62	2197	3559	21.5	90.9	4,361,461
0.62	2197	3559	21.5	90.9	24,870,798
0.62	2197	3559	21.5	90.9	5,329,296

Table 10. Cycles to failure for lost foam 356-T7 with as-cast surface

R	Minimum load (N)	Maximum load (N)	Thickness (mm)	Alternating stress (MPa)	Mean stress (MPa)	Cycles to failure
-1	-2157	2157	3.18	67	0	453,370
-1	-2157	2157	3.18	67	0	734,219
-1	-2157	2157	3.15	67	0	714,100
-1	-1966	1966	3.12	62	0	215,919
-1	-1966	1966	3.18	61	0	317,466
-1	-1837	1837	3.18	57	0	372,640
-1	-1837	1837	3.12	58	0	971,403
-1	-1837	1837	3.23	56	0	880,040
-1	-1646	1646	3.18	51	0	1,346,394
-1	-1646	1646	3.12	52	0	1,823,157
-0.89	-1259	1410	3.15	42	2	697,621
-0.89	-1259	1410	3.20	41	2	5,571,116
-0.89	-1259	1410	3.00	44	2	3,192,819
0	0	3158	3.05	51	51	152,661
0	0	3158	3.25	48	48	345,206
0	0	2887	3.05	47	47	393,661
0	0	2887	2.62	54	54	386,067
0	0	2887	2.62	54	54	317,172
0	0	2887	3.10	46	46	221,445
0	0	2696	2.82	47	47	362,635
0	0	2696	2.90	46	46	421,559
0	0	2424	3.00	40	40	262,855
0	0	2424	2.92	41	41	727,386
0	0	2424	3.07	39	39	693,066
0	0	2068	3.10	33	33	2,413,722
0	0	2068	3.07	33	33	1,914,190
0.09	298	3327	3.10	48	58	385,936
0.09	298	3327	3.20	47	56	439,254
0.09	298	3327	3.20	47	56	332,457
0.26	881	3403	3.07	40	69	489,908
0.26	881	3403	3.23	38	65	1,042,450
0.37	1286	3474	3.15	34	74	345,067
0.37	1286	3474	3.07	35	76	770,908
0.40	1277	3194	3.15	30	70	1,018,546
0.40	1277	3194	3.12	30	70	1,180,591
0.44	1250	2847	3.18	25	64	3,991,069
0.44	1250	2847	3.12	25	65	10,107,592
0.44	1250	2847	3.18	25	64	2,310,185

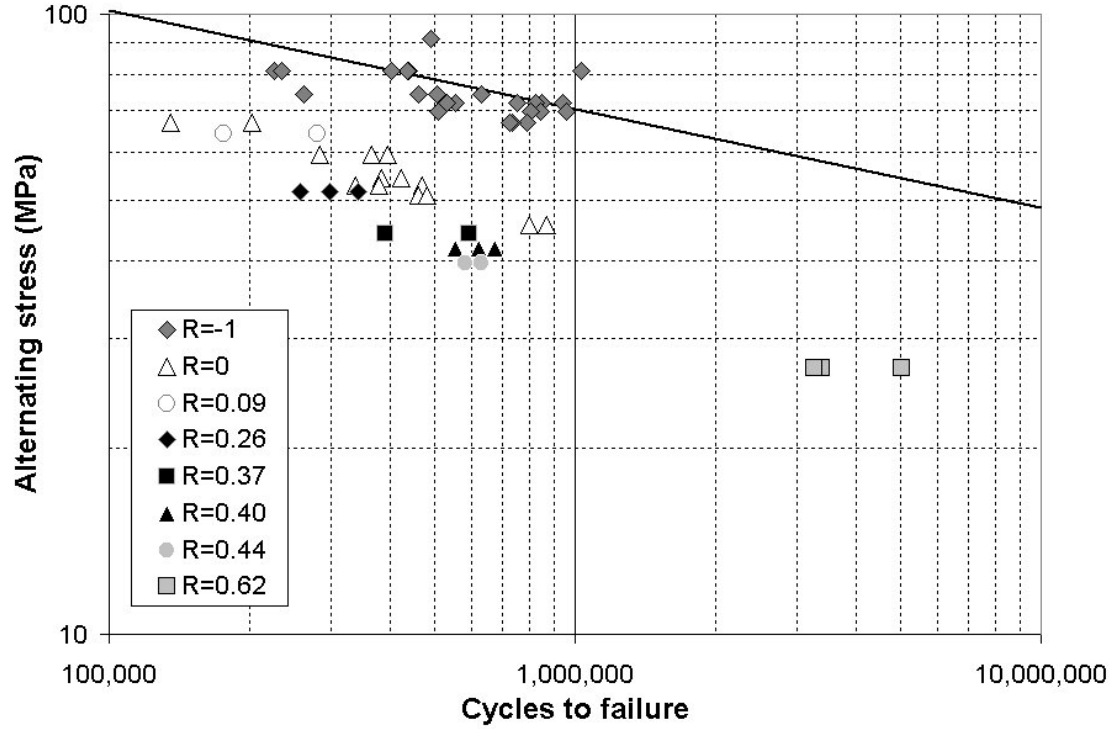

Figure 21. *S-N* curve for lost foam 356-T6 with machined surface. Basquin parameters: σ_f' = 714 MPa; b = -0.1598.

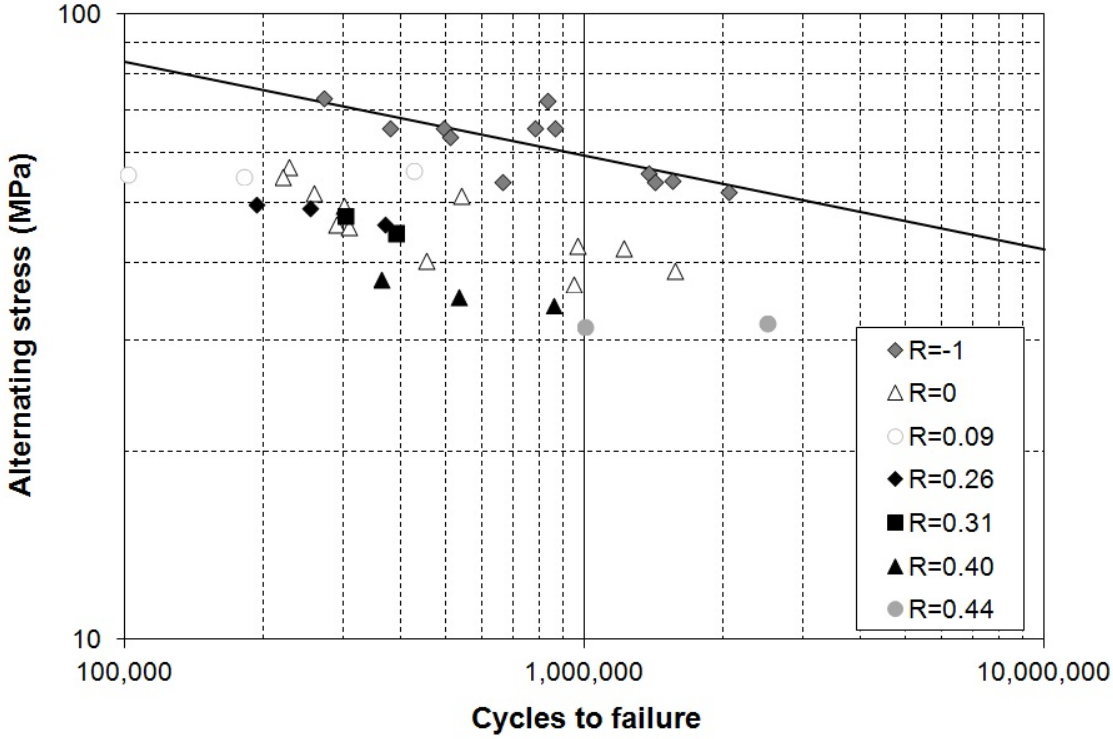

Figure 22. *S-N* curve for lost foam 356-T6 with as-cast surface. Basquin parameters: σ_f' = 522 MPa; b = -0.1498.

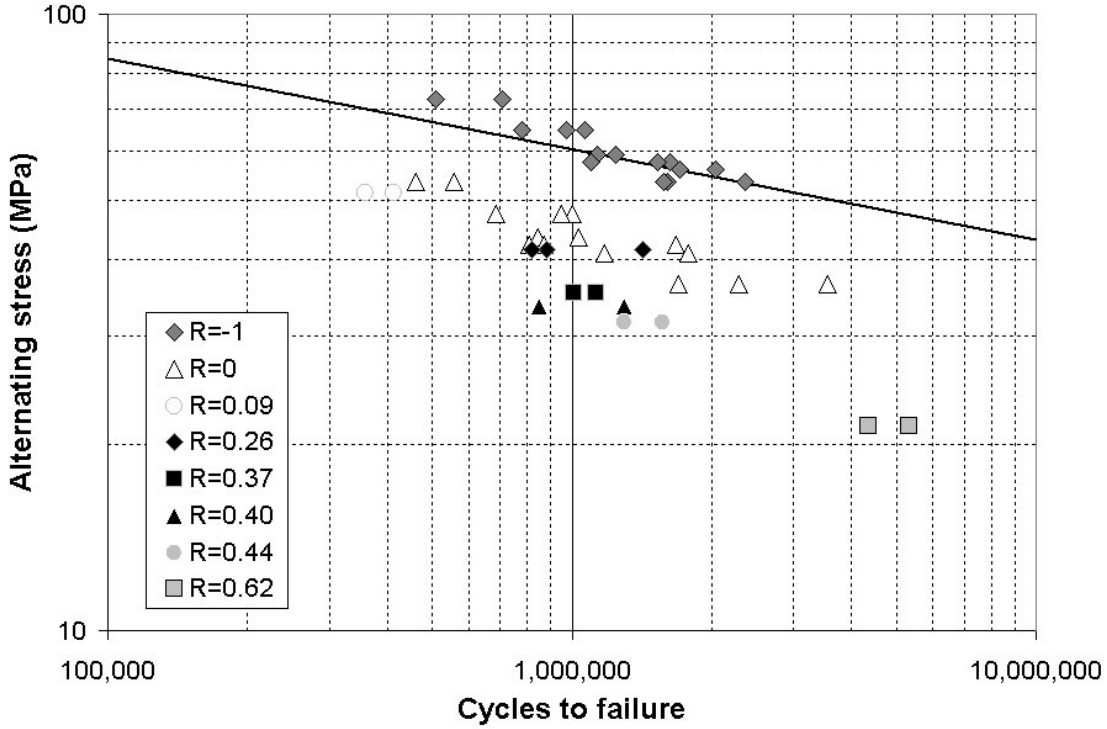

Figure 23. ***S-N*** **curve for lost foam 356-T7 with machined surface. Basquin parameters:** σ_f' **= 509 MPa;** b **= -0.1469.**

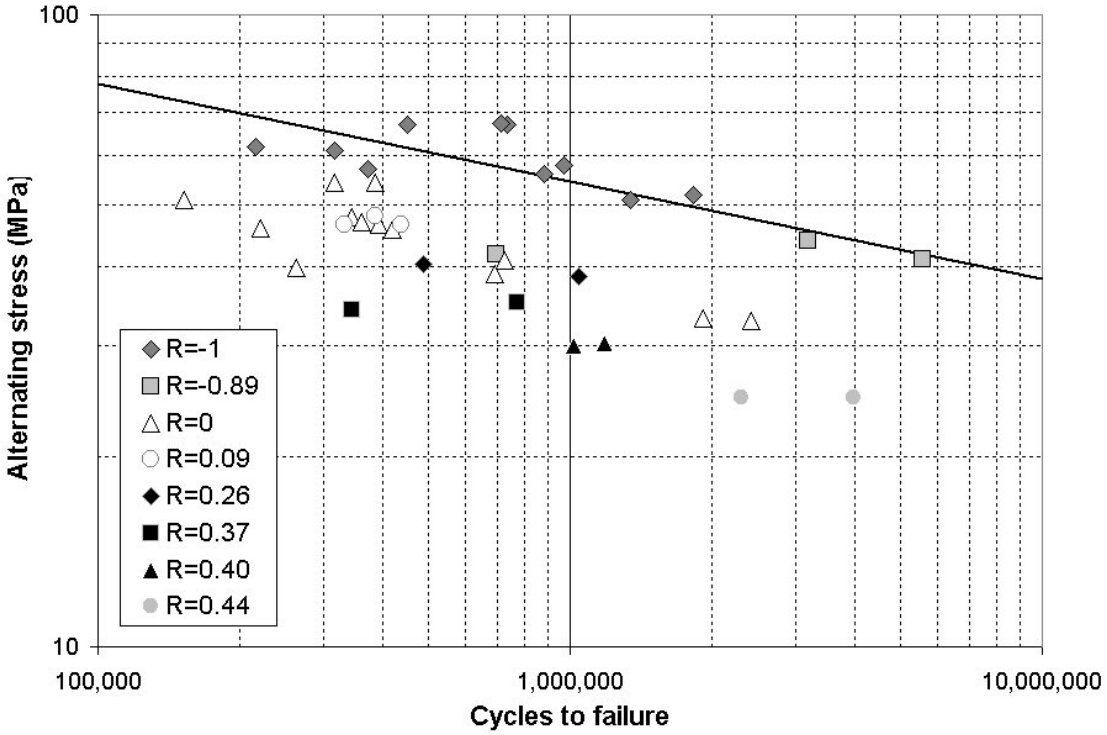

Figure 24. ***S-N*** **curve for lost foam 356-T7 with as-cast surface. Basquin parameters:** σ_f' **= 516 MPa;** b **= -0.1550.**

3.3 SCANNING ELECTRON MICROGRAPHS

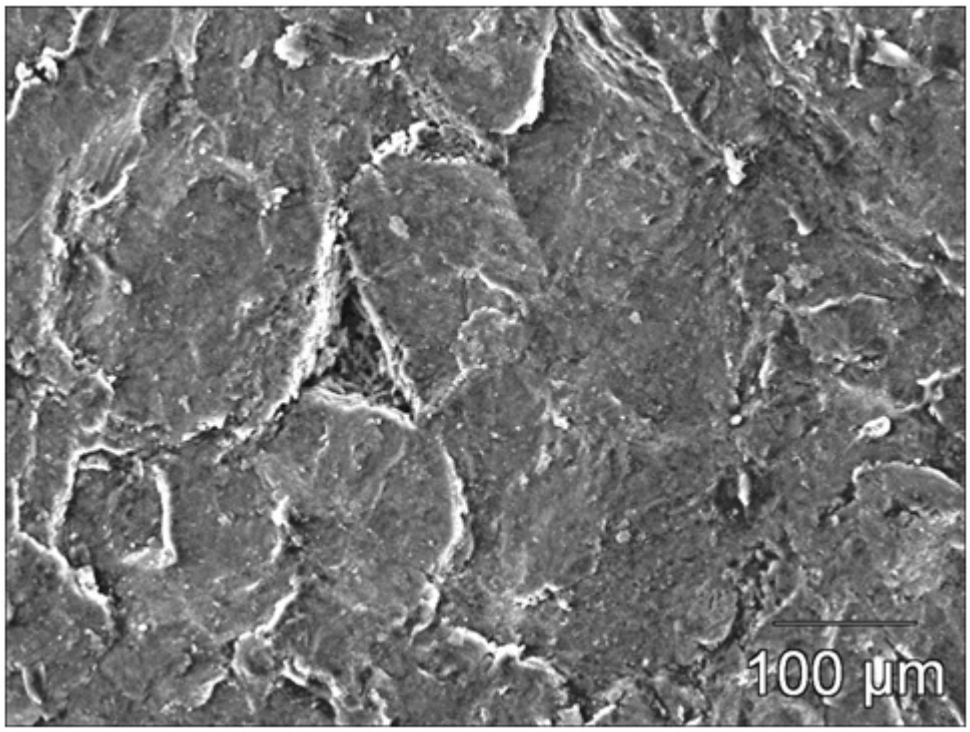

Figure 25. As-cast specimen surface.

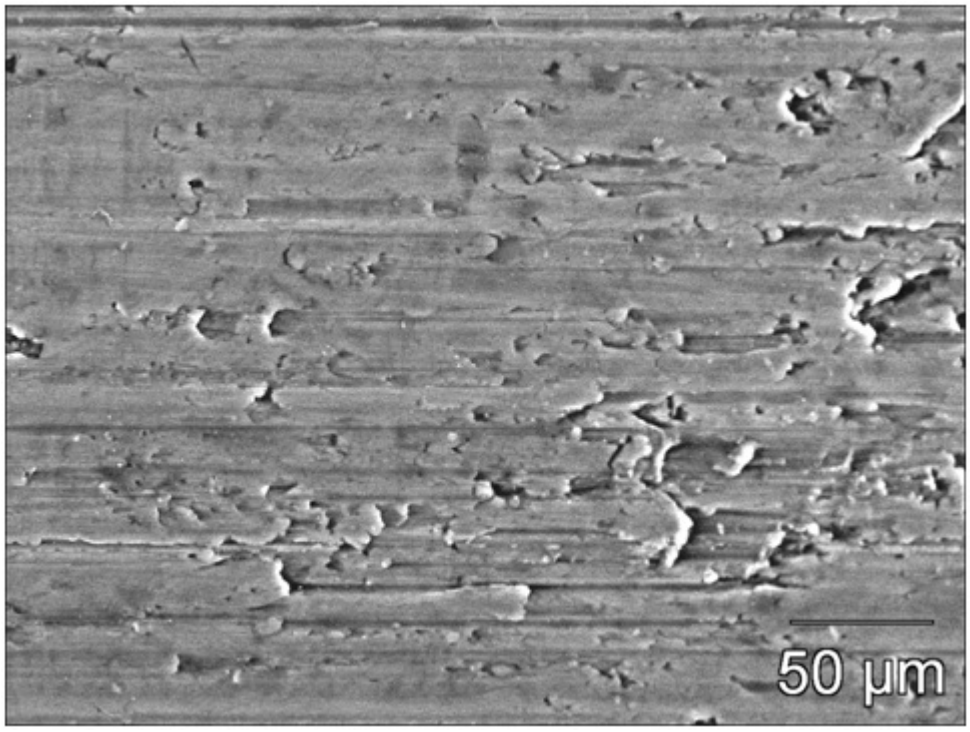

Figure 26. Machined specimen surface.

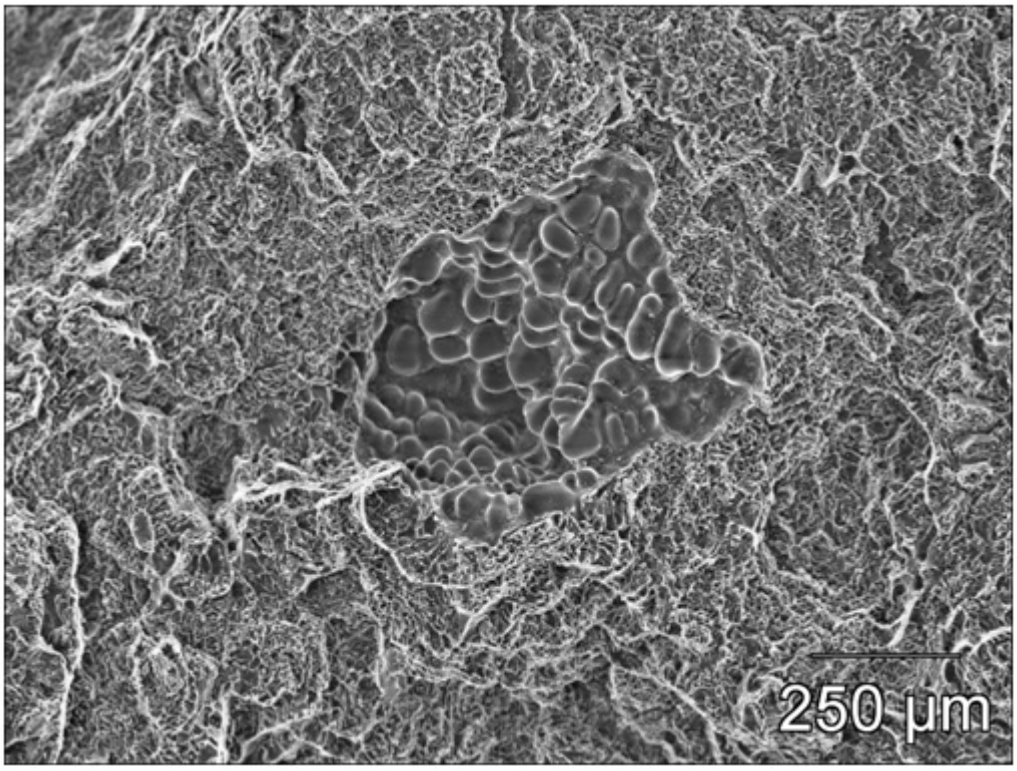

Figure 27. Fracture surface of machined 356-T6 tensile test specimen.

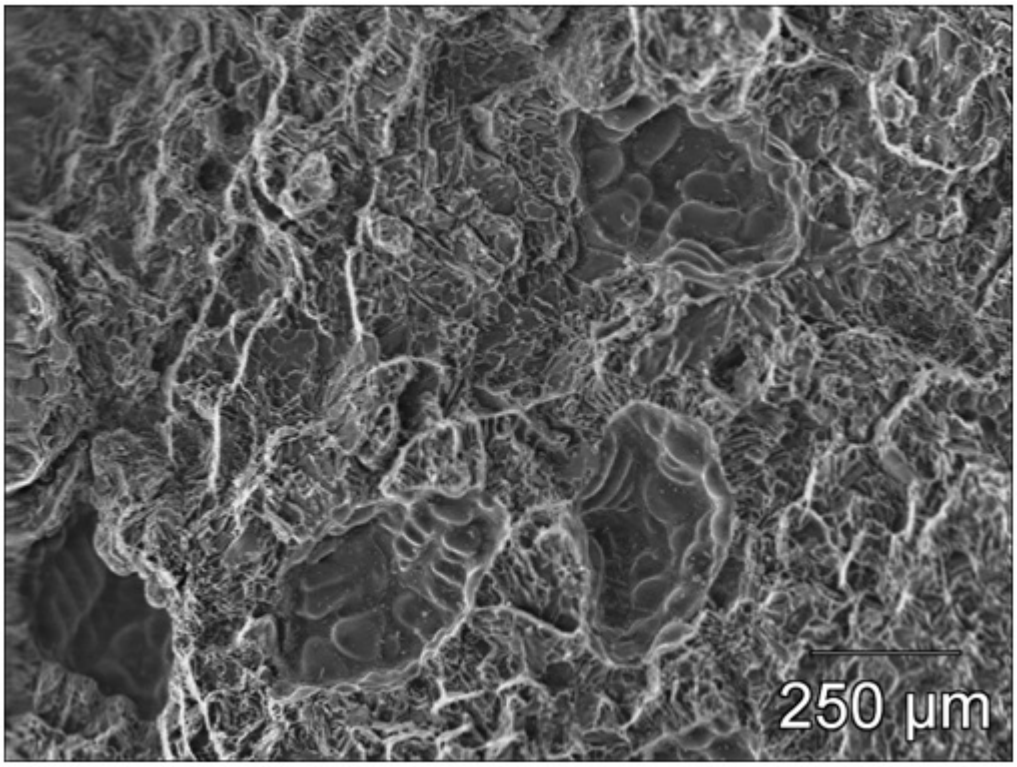

Figure 28. Fracture surface of as-cast 356-T6 tensile test specimen.

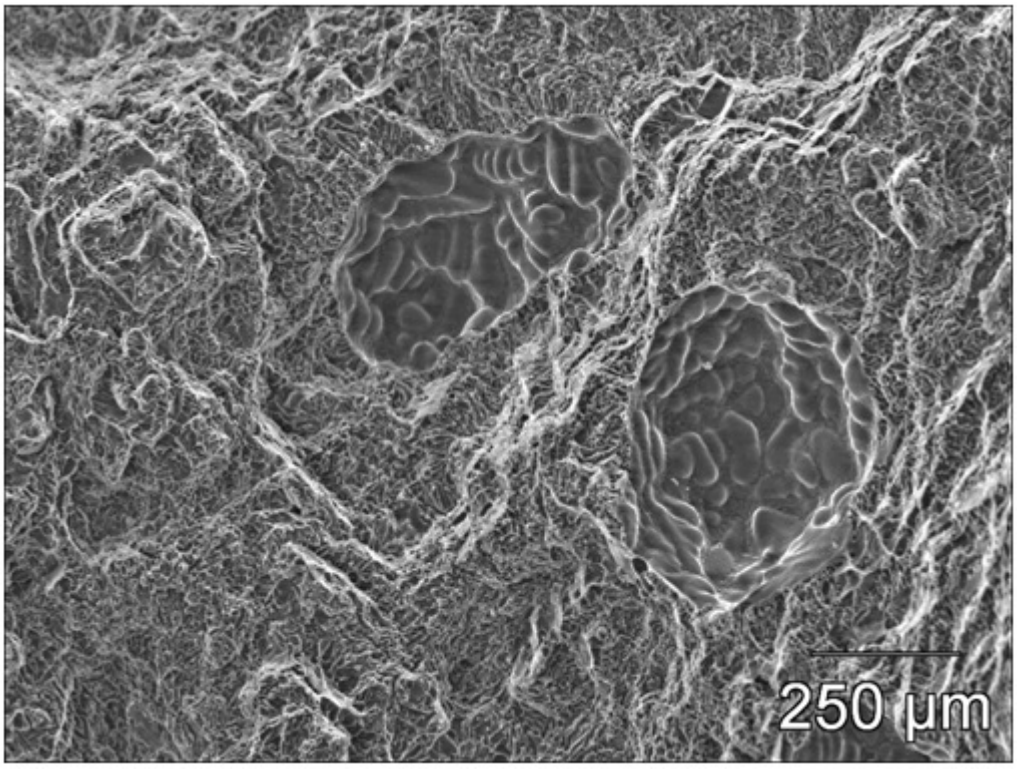

Figure 29. Fracture surface of machined 356-T7 tensile test specimen.

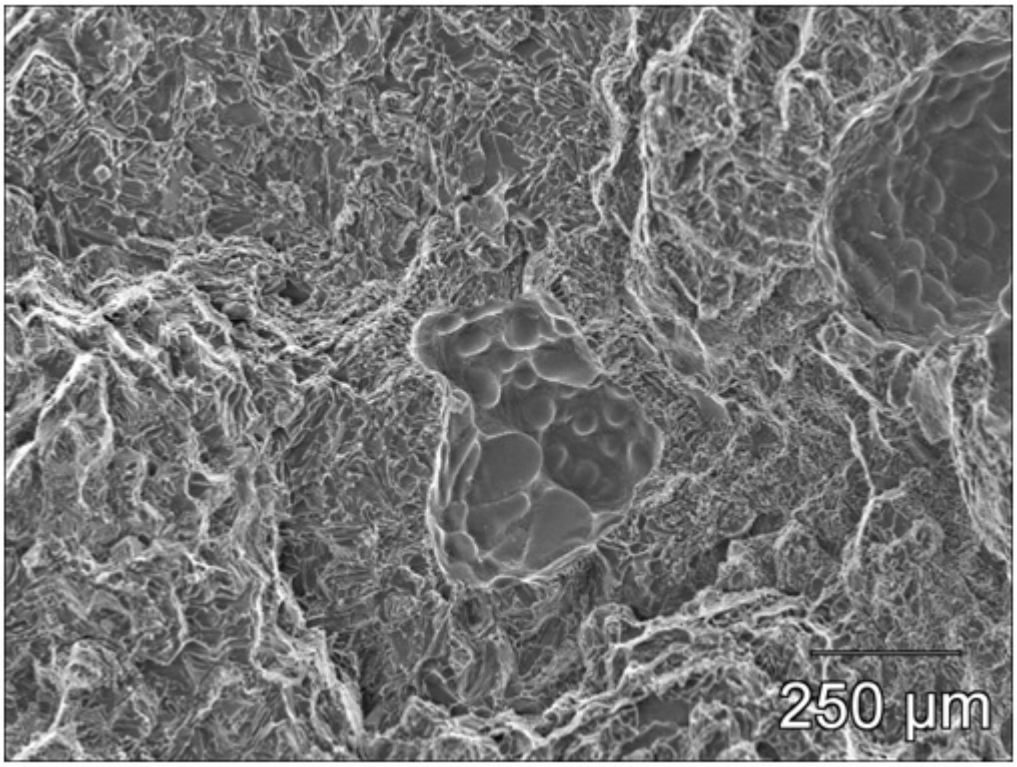

Figure 30. Fracture surface of as-cast 356-T7 tensile test specimen.

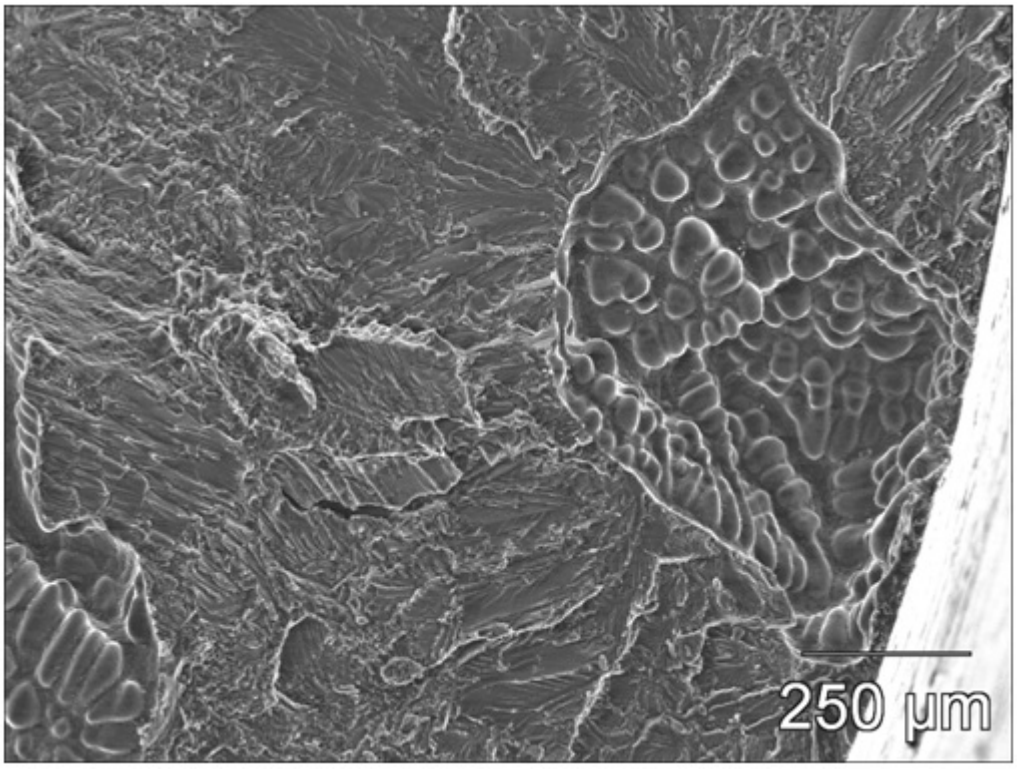

Figure 31. Fracture surface of machined 356-T6 fatigue specimen (*R*=0, maximum load 3345 N, cycles to failure 470,594, defect area 0.10 mm²).

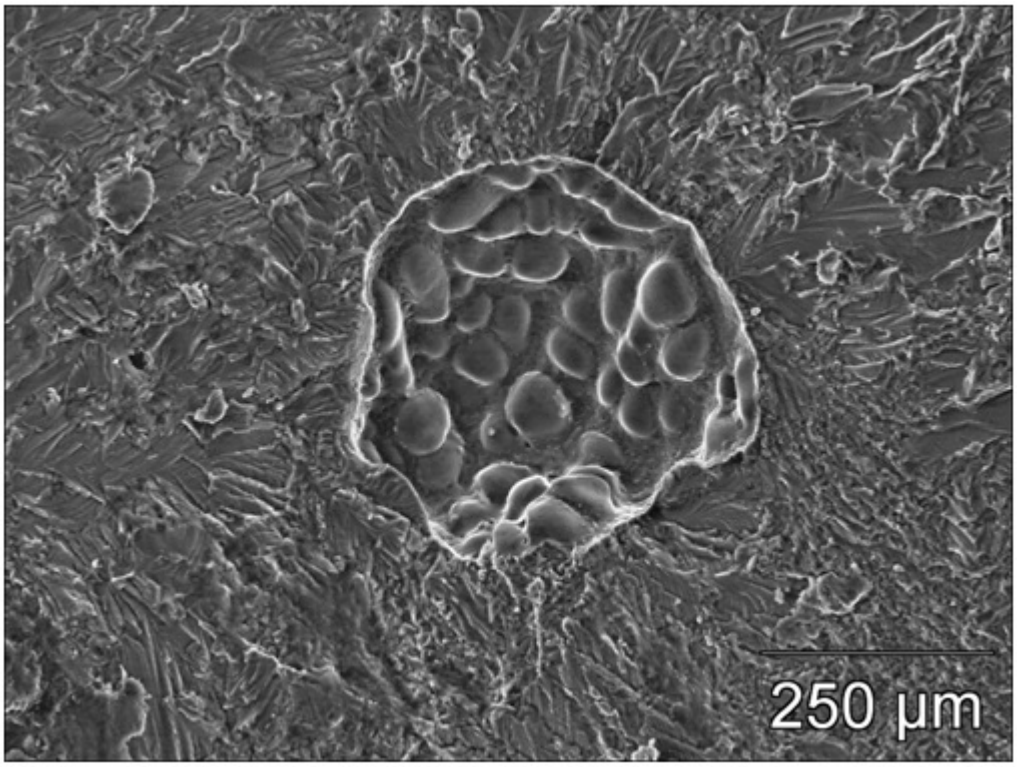

Figure 32. Fracture surface of as-cast 356-T6 fatigue specimen (*R*=-1, minimum load -2068 N, maximum load 2068 N, cycles to failure 859,634, defect area 0.08 mm²).

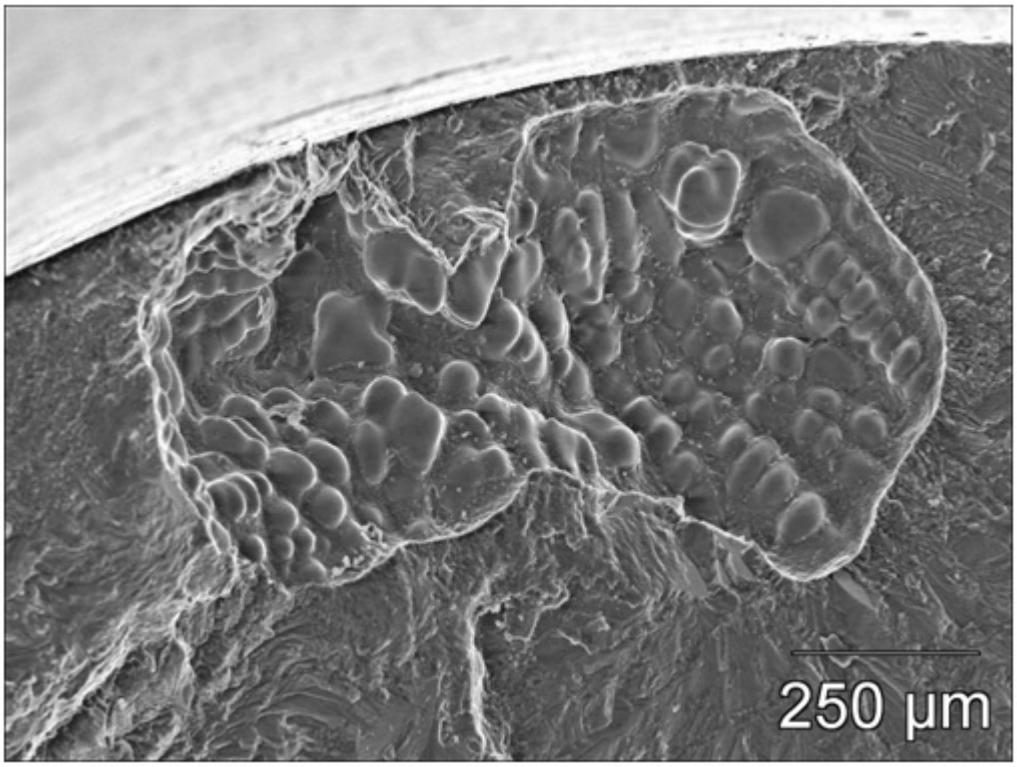

Figure 33. Fracture surface of machined 356-T7 fatigue specimen (*R*=-1, minimum load -2051 N, maximum load 2051 N, cycles to failure 1,064,794, defect area 0.18 mm²).

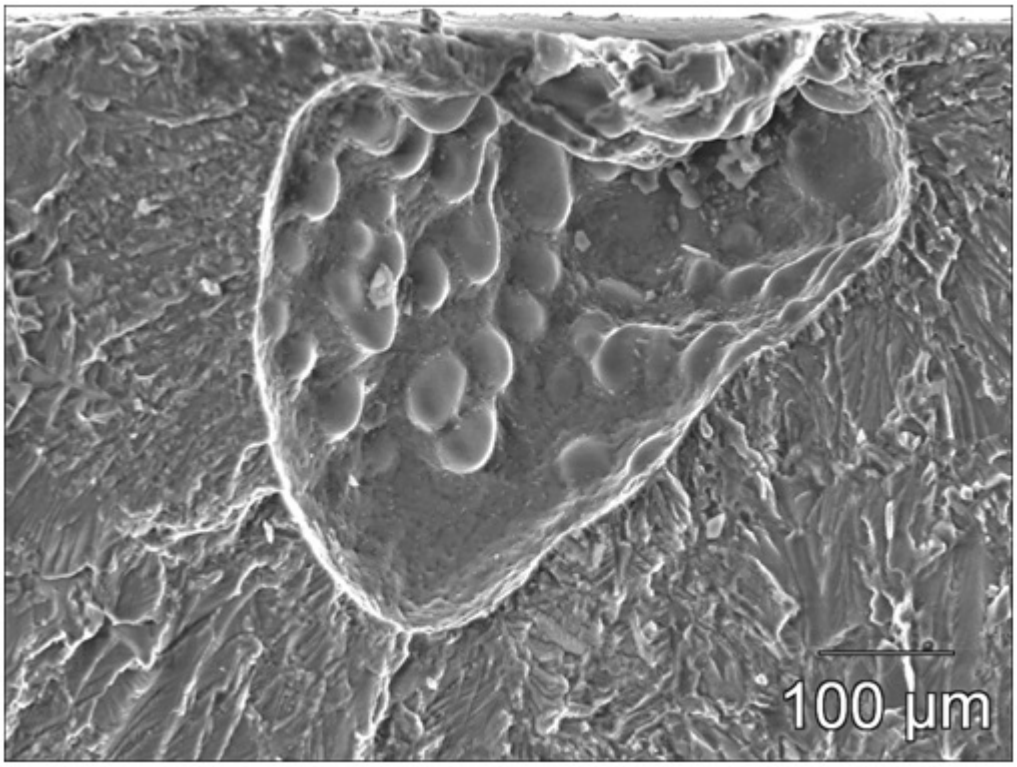

Figure 34. Fracture surface of as-cast 356-T7 fatigue specimen (*R*=0, maximum load 2424 N, cycles to failure 727,386, defect area 0.03 mm²).

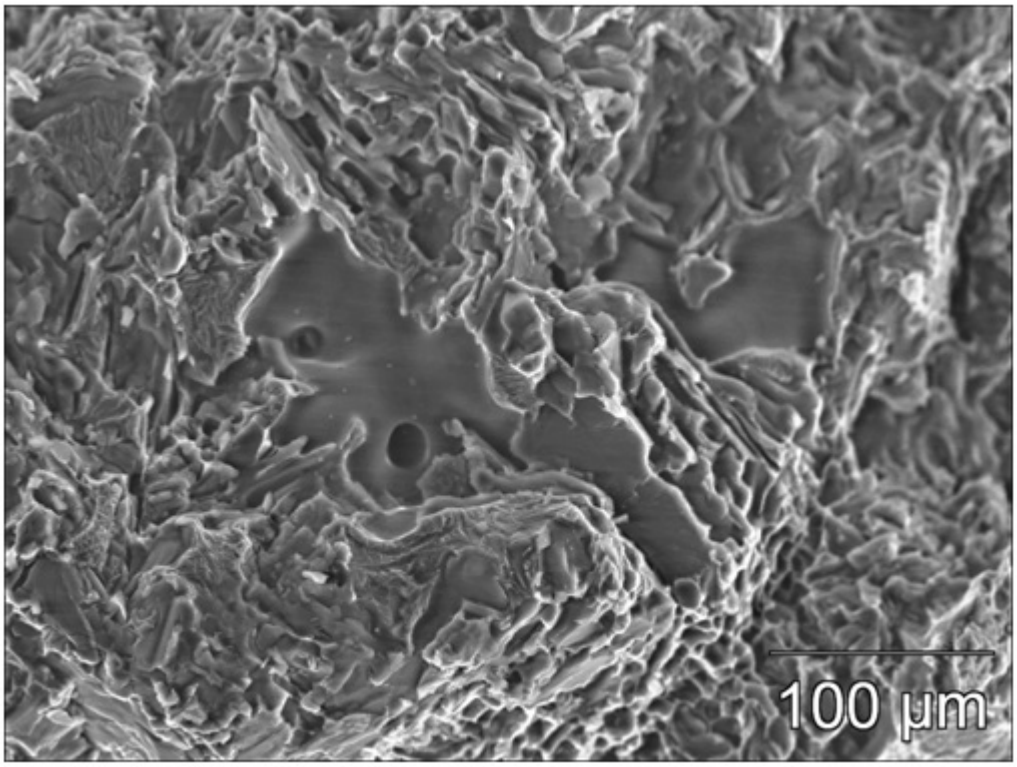

Figure 35. Close-up of fold defect from fracture surface of as-cast 356-T6 tensile specimen.

3.4 PORE SIZE MEASUREMENTS

ImageJ software was used to measure the size of the critical pore (i.e. the pore from which fatigue appeared to initiate). The measured pore areas are given in Tables 11 – 14, on the following page. For all of the machined surface specimens, the fracture appeared to initiate from a defect located at or near the machined surface, as seen in Figures 31 and 33, above. For most of the as-cast surface specimens, the fracture appeared to initiate from a defect located in the bulk, as seen in Figure 32; fractures initiating from defects at the surface, as seen in Figure 34, were more rare. In both the as-cast and machined specimens, all of the fractures appeared to initiate from pores. None of the fractures initiated from surface flaws of the type seen in Figure 3.

Figure 11. Pore size for lost foam 356-T6 with machined surface

R	Minimum load (N)	Maximum load (N)	Cycles to failure	Critical pore area (mm^2)
-1	-2562	2562	261,898	0.279
-1	-2562	2562	404,262	0.097
-1	-2562	2562	437,409	0.090
-1	-2562	2562	462,649	0.152
-1	-2562	2562	504,488	0.039
-1	-2562	2562	1,031,085	0.046
0	0	3345	338,181	0.116
0	0	3345	378,667	0.090
0	0	3345	470,594	0.102
0.40	1788	4448	555,037	0.108
0.40	1788	4448	621,528	0.089
0.40	1788	4448	624,528	0.126

Figure 12. Pore size for lost foam 356-T6 with as-cast surface

R	Minimum load (N)	Maximum load (N)	Cycles to failure	Critical pore area (mm^2)
-1	-2068	2068	376,818	0.083
-1	-2068	2068	778,085	0.117
-1	-2068	2068	859,634	0.077
0	0	2487	451,319	0.080
0	0	2487	959,461	0.020
0	0	2487	1,210,621	0.019
0.40	1317	3296	359,927	0.170
0.40	1317	3296	528,929	0.375
0.40	1317	3296	850,922	0.073

Figure 13. Pore size for lost foam 356-T7 with machined surface

R	Minimum load (N)	Maximum load (N)	Cycles to failure	Critical pore area (mm^2)
-1	-2051	2051	507,983	0.110
-1	-2051	2051	706,328	0.087
-1	-2051	2051	781,135	0.132
-1	-2051	2051	1,064,794	0.185
0	0	3007	684,971	0.110
0	0	3007	947,782	0.090
0	0	3007	1,005,070	0.097
0.26	934	3559	819,491	0.095
0.26	934	3559	880,352	0.083
0.26	934	3559	1,417,558	0.124

Figure 14. Pore size for lost foam 356-T7 with as-cast surface

R	Minimum load (N)	Maximum load (N)	Cycles to failure	Critical pore area (mm^2)
-1	-1837	1837	372,640	0.106
-1	-1837	1837	880,040	0.263
-1	-1837	1837	971,403	0.125
0	0	2424	262,855	0.181
0	0	2424	693,066	0.090
0	0	2424	727,386	0.029
0.26	881	3403	489,908	0.042
0.26	881	3403	1,042,450	0.170
0.37	1286	3474	345,067	0.183
0.037	1286	3474	770,908	0.077

CHAPTER 4 – ANALYSIS AND DISCUSSION

4.1 EFFECT OF HEAT TREATMENT AND SURFACE FINISH ON MONOTONIC MECHANICAL PROPERTIES

Table 15 shows the tensile modulus, yield strength, tensile strength, and elongation for lost foam cast 356 aluminum in conditions T6 and T7 with machined and as-cast surfaces. This data is shown graphically in Figures 36 – 38.

Table 15. Monotonic mechanical properties summary

Condition	Surface	Tensile modulus, GPa	Yield strength, MPa	Tensile strength, MPa	Elongation	Quality index, MPa
T6	Machined	69.5	250	295	2.03%	344
T6	As-cast	66.5	238	239	0.56%	201
T7	Machined	69.8	257	280	1.31%	277
T7	As-cast	68.2	230	235	0.62%	202

The tensile modulus was roughly equal (within ~5%), regardless of heat treatment or surface condition. This result was expected, since the elastic modulus is primarily a function of the interatomic potential, which is not affected by heat treatment or surface condition.

For the machined specimens, the T6 condition had slightly lower yield strength, and significantly higher tensile strength and higher elongation (resulting in a higher quality index) than the T7 condition. For the as-cast specimens, the T6 condition had slightly higher yield strength than the T7 condition, while the tensile strength and

elongation, and therefore the quality index, were essentially equal (within one standard deviation) for both conditions.

The difference between the T6 and T7 conditions was not as great as the difference between the machined-surface and as-cast specimens. The as-cast specimens had significantly lower tensile strength, yield strength, and elongation than the machined-surface specimens. This suggests that the as-cast surface plays a larger role than heat treatment in determining the monotonic tensile properties.

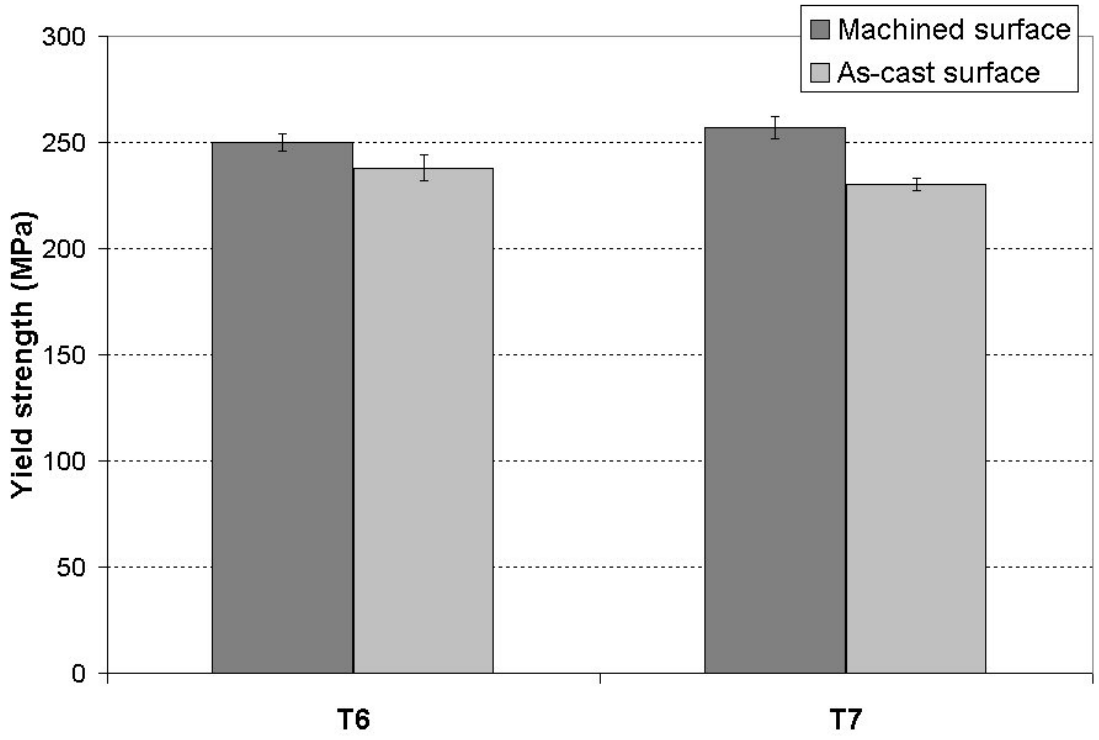

Figure 36. Yield strength for 356-T6 and 356-T7 with as-cast or machined surface.

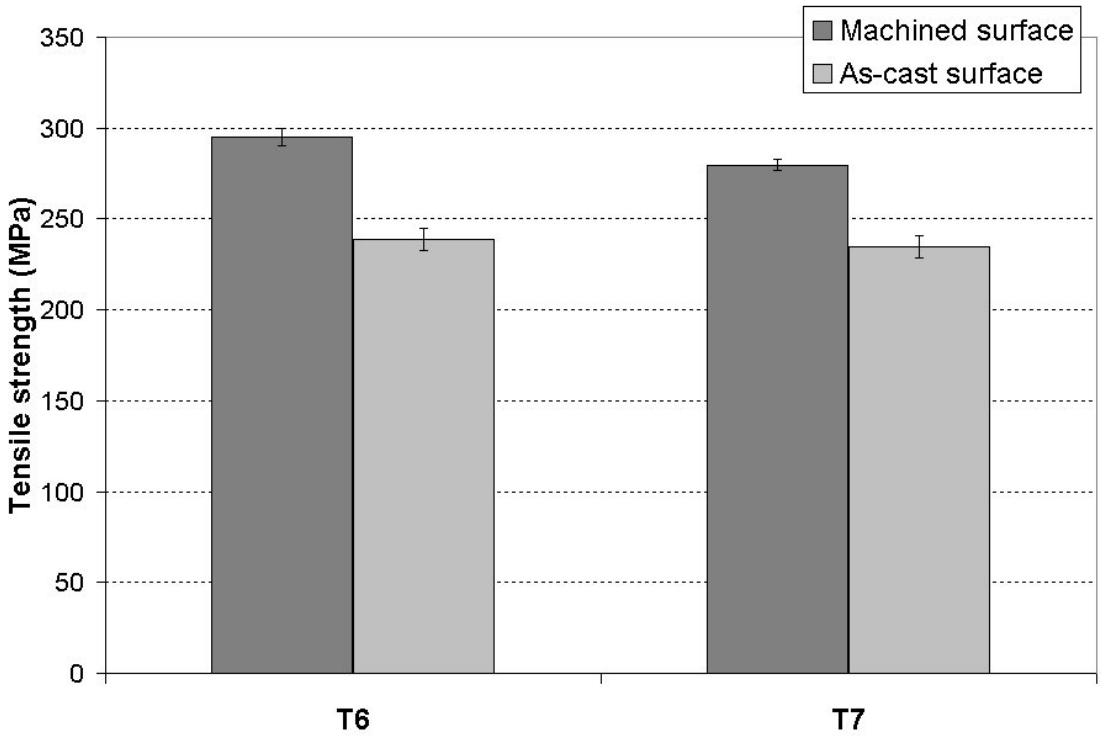

Figure 37. Tensile strength for 356-T6 and 356-T7 with as-cast or machined surface.

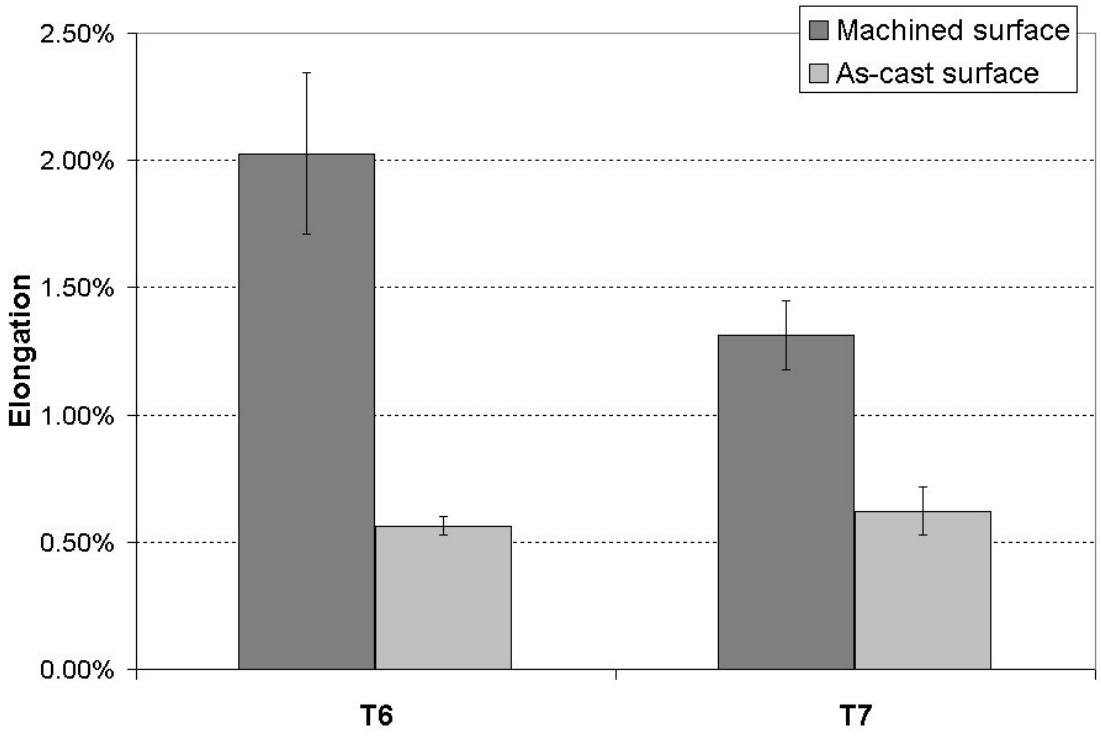

Figure 38. Elongation for 356-T6 and 356-T7 with as-cast or machined surface.

4.2 WEIBULL ANALYSIS OF FATIGUE DATA

The slope of the $S - N$ curve (Basquin exponent b) for the $R = -1$ data for each set of specimens was used to extrapolate each $R = -1$ datapoint to the expected stress at which the given specimen would have failed in 10^5, 10^6, or 10^7 cycles. This data was then fitted using a two-parameter Weibull distribution, with shape parameter β and characteristic life α. The two-parameter Weibull distribution was used to determine a B10 and B50 stress for 10^5, 10^6, and 10^7 for each set of specimens. The B10 and B50 stresses represent the stress at which there is a 10% or a 50% probability of failure, respectively, in the given number of cycles. The results of the Weibull analysis are shown in Table 16, below. Weibull distribution plots for each set of specimens are shown in Figures 39 – 42. (In the interest of space, only the plots for 10^6 cycles are shown).

Table 16. Weibull analysis of fatigue data

Condition	Surface	Shape parameter β	10^5 cycles			10^6 cycles			10^7 cycles		
			α, MPa	B10, MPa	B50, MPa	α, MPa	B10, MPa	B50, MPa	α, MPa	B10, MPa	B50, MPa
T6	Machined	16.99	104.9	91.9	102.7	72.6	63.6	71.1	50.3	44.0	49.2
T6	As-cast	12.83	87.3	73.3	84.9	61.9	51.9	60.1	43.8	36.8	42.6
T7	Machined	20.58	89.0	79.8	87.4	63.4	56.9	62.3	45.2	40.5	44.4
T7	As-cast	8.72	81.7	63.1	78.3	57.1	44.2	54.8	40.0	30.9	38.4

The Weibull shape parameter β is a measure of dispersion. The lower the value of β, the greater the scatter in the data. The as-cast specimens showed significantly greater scatter than the machined-surface specimens. This is expected, based on the distribution of failure-initiating flaws in the as-cast surface. The B50 and B10 stresses for 10^6 cycles for the four sets of specimens are plotted in Figures 43 and 44.

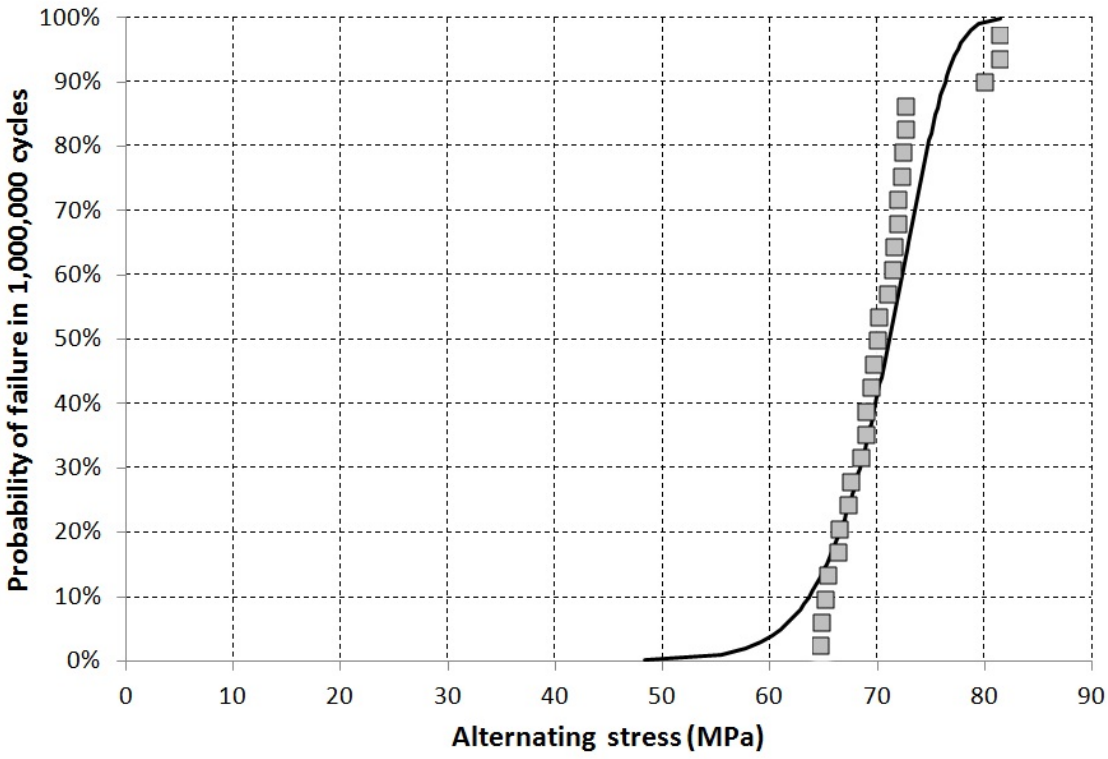

Figure 39. Two-parameter Weibull distribution for 356-T6 with machined surface (*R*=-1).

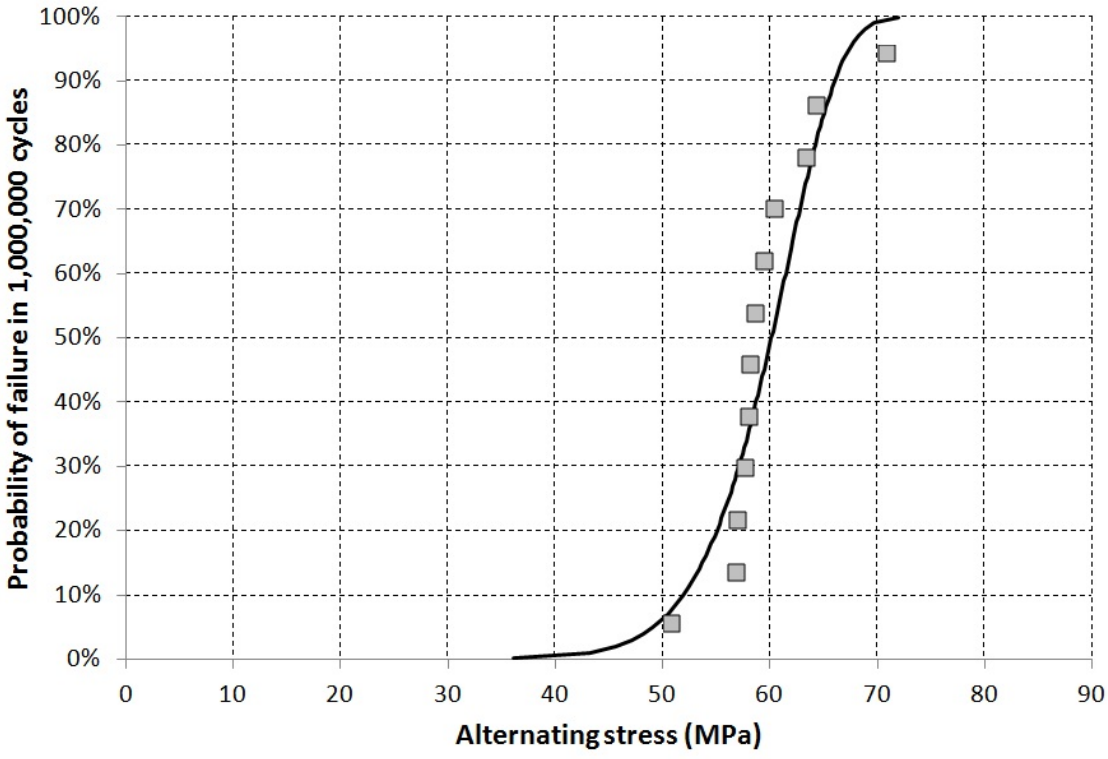

Figure 40. Two-parameter Weibull distribution for 356-T6 with as-cast surface (*R*=-1).

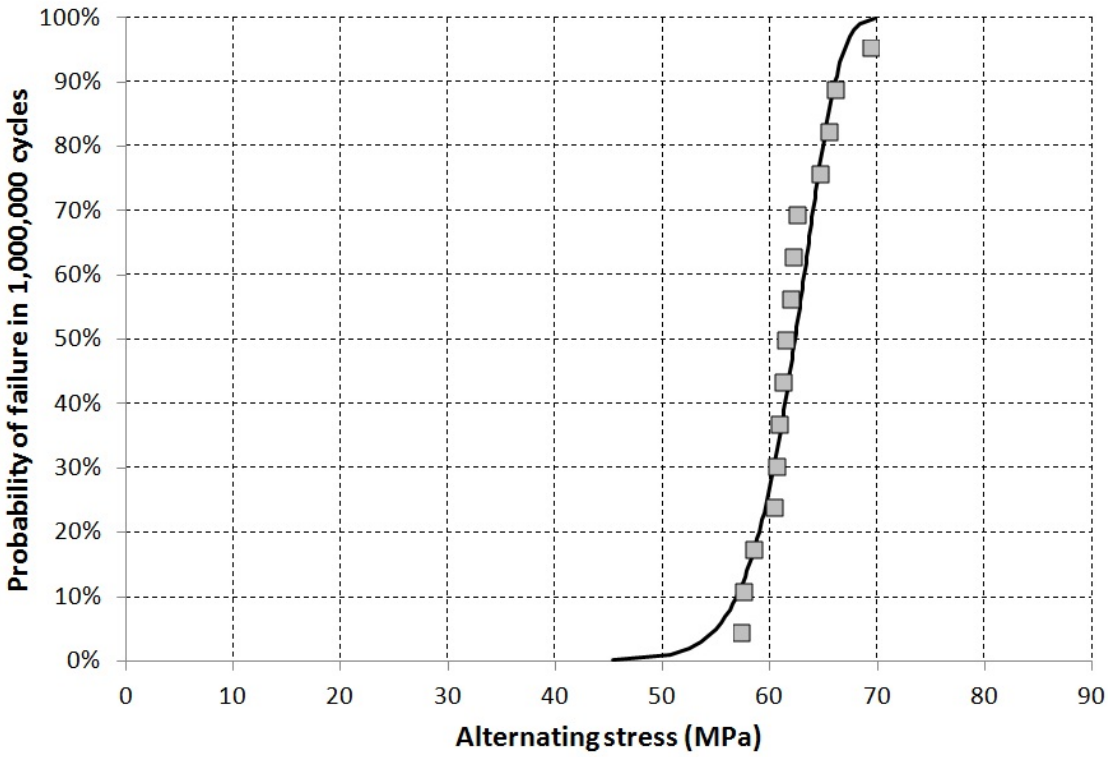

Figure 41. Two-parameter Weibull distribution for 356-T7 with machined surface (*R*=-1).

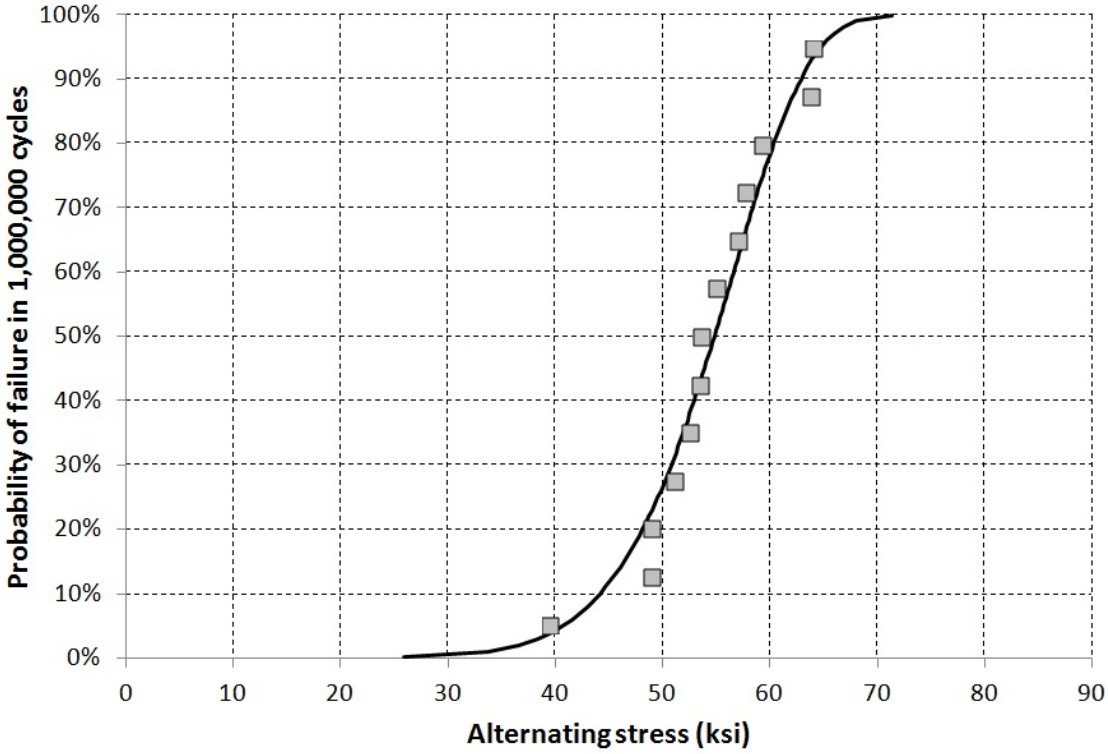

Figure 42. Two-parameter Weibull distribution for 356-T7 with as-cast surface surface (*R*=-1).

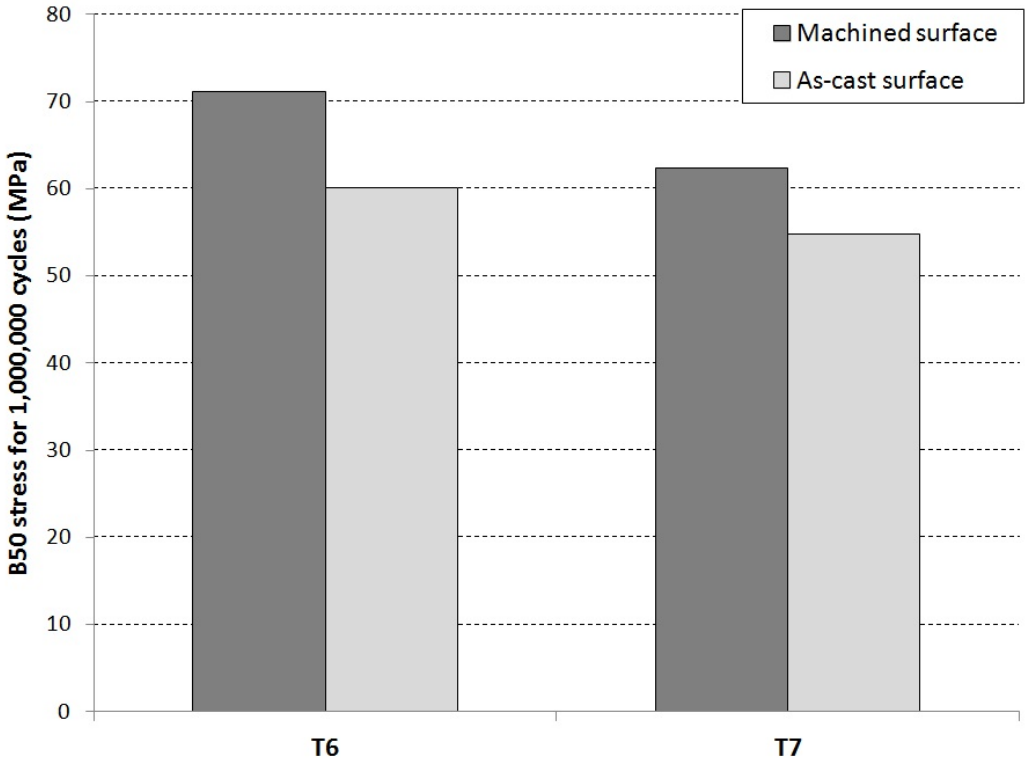

Figure 43. B50 stress for 1,000,000 cycles for 356-T6 and 356-T7 with as-cast or machined surface.

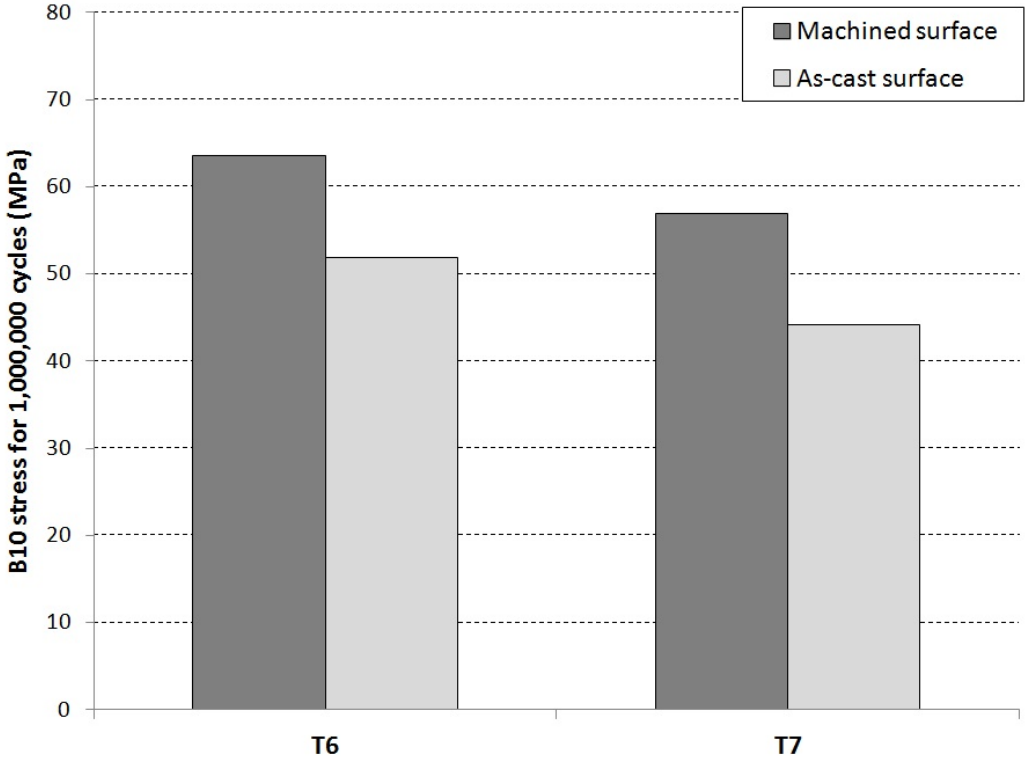

Figure 44. B10 stress for 1,000,000 cycles for 356-T6 and 356-T7 with as-cast or machined surface.

4.3 COMPARISON OF FATIGUE MEAN STRESS EQUATIONS

Nine different mean stress equations were compared: Goodman, Soderberg, Morrow, Gerber, ASME-Elliptic, Smith-Watson-Topper, Stulen, Topper-Sandor, and Walker.

Each equation provides an equivalent fully-reversed stress (σ_{eq}) for a given pair of alternating stress (σ_a) and mean stress (σ_m). This equivalent stress was then substituted into the Basquin equation to provide a predicted number of cycles to failure. The predicted cycles to failure were compared against the actual cycles to failure, and the percentage error is calculated. The relative accuracy of the various mean stress equations can be compared on the basis of the mean error percentage. Fitting parameters, for the three equations that require them (Stulen, Topper-Sandor, and Walker), were determined using an iterative process (Microsoft Excel goal seek) to minimize the mean error percentage. Results for each of the equations are given in the Appendix.

It could be argued, with some justification, that comparing the equations on the basis of the error in the predicted cycles to failure is not a mathematically sophisticated approach. Among other things, since the underlying behavior is exponential in nature, the error percentage will naturally increase as the number of cycles to failure increases. However, the error percentage provides a comparison metric that is intuitively easy to grasp.

A positive error percentage means that the equation is non-conservative, i.e. the number of cycles to failure predicted by the equation is greater than the actual number of cycles to failure. A negative error percentage means that the equation is conservative. With the exception of the Smith-Watson-Topper equation, all of the equations that did not include fitting parameters (Goodman, Soderberg, Morrow, Gerber, and ASME-Elliptic) were consistently non-conservative. The Smith-Watson-Topper equation was conservative for the 356-T7 specimens, but non-conservative for the 356-T6 specimens.

The Goodman, Soderberg, and Morrow equations are all linear in form. The Goodman equation, which is the most widely used of the three, consistently over-estimated fatigue lives by an average of 202 – 343%.

The Soderberg equation is equivalent in form to the Goodman equation, except the ultimate tensile strength σ_u is replaced with the yield strength σ_o. This provided a slightly less non-conservative fit for the machined-surface specimens. For the as-cast surface specimens, the yield strength and tensile strength were very close in value, since these specimens had very little ductility. Therefore, for the as-cast specimens, the Soderberg equation yielded nearly identical results to the Goodman equation.

The Morrow equation is also equivalent in form to the Goodman equation, except that the ultimate tensile strength σ_u is replaced with the Basquin parameter σ_f' (i.e. the intercept of the $S - N$ curve with the stress axis). Since σ_f' is greater than σ_u, by as much as an order of magnitude, and the Goodman equation is already non-conservative, the

Morrow equation yielded results that were even less conservative: it overestimated fatigue lives by an average of 748 – 1347%.

The Gerber and ASME-Elliptic equations are both parabolic in form. Both equations gave highly non-conservative results, predicting lives that exceed the actual life by an order of magnitude or more.

Of the equations that do not include any fitting parameters, the SWT equation is the most accurate by far. It yielded slightly non-conservative results for the 356-T6 specimens, and conservative results for the 356-T7 specimens.

Table 17 compares the error percentages for the six equations that do not include fitting parameters. While there are differences in the error percentages for the different sample groups, the trend with regard to the suitability of the various equations is consistent. In descending order of accuracy, they are: Smith-Watson-Topper (most accurate), Soderberg, Goodman, Morrow, Gerber, and ASME-Elliptic (least accurate).

Table 17. Error percentages for mean stress equations without fitting parameters

Condition	Surface	Goodman equation	Soderberg equation	Morrow equation	Gerber equation	ASME equation	SWT equation
T6	Machined	254%	134%	1238%	1517%	1840%	18%
T6	As-cast	343%	339%	1347%	1947%	2592%	44%
T7	Machined	323%	246%	1040%	1866%	2362%	-23%
T7	As-cast	202%	189%	748%	1091%	1370%	-10%

For the three equations that include fitting parameters (Stulen, Topper-Sandor, and Walker), the mean error percentage is much lower than for the equations that do not

include fitting parameters. This should not be surprising, since the fitting parameters were chosen using an iterative process to minimize the mean error. For these equations, the mean of the absolute value of the error percentage is also compared. This is shown in Table 18. All three equations provide a reasonable degree of accuracy, with the Walker and Topper-Sandor equations performing perhaps slightly better than the Stulen equation.

Table 18. Error percentages for mean stress equations with fitting parameters

Condition	Surface	Stulen equation		Topper-Sandor equation		Walker equation	
		Mean	Absolute	Mean	Absolute	Mean	Absolute
T6	Machined	0.03%	47%	-0.13%	36%	-0.20%	33%
T6	As-cast	0.00%	44%	0.18%	38%	-0.06%	40%
T7	Machined	0.09%	40%	-0.14%	30%	0.04%	34%
T7	As-cast	-0.04%	48%	-0.12%	42%	0.20%	45%

The Stulen, Topper-Sandor, and Walker parameters for each of the four groups of specimens are compared in Table 19. The values of these parameters appear to depend more closely on the heat treatment condition than on the surface finish. In contrast, it should be recalled from Table 15 that the monotonic properties were found to depend more closely on surface finish than on heat treatment. This suggests that, while the monotonic properties are determined largely by macroscale features (e.g. casting defects, oxide folds), the mean stress sensitivity is determined primarily by microstructure.

Table 19. Mean stress sensitivity parameters

Condition	Surface	Stulen parameter (A)	Topper-Sandor parameter (α)	Walker parameter (γ)
T6	Machined	0.417	0.793	0.530
T6	As-cast	0.454	0.803	0.563
T7	Machined	0.341	0.734	0.459
T7	As-cast	0.372	0.749	0.480

4.4 STATISTICAL DISTRIBUTION OF CRITICAL PORES

A histogram of the critical defect area for the as-cast and machined specimens is shown in Figure 45, below. Weibull distribution plots for the critical defect area are shown in Figures 46 and 47. While the characteristic defect size α was the same for both machined and as-cast specimens (0.13 mm²), the as-cast specimens showed significantly greater dispersion in defect size than the machined specimens (β = 2.73 for machined specimens; β = 1.41 for as-cast specimens).

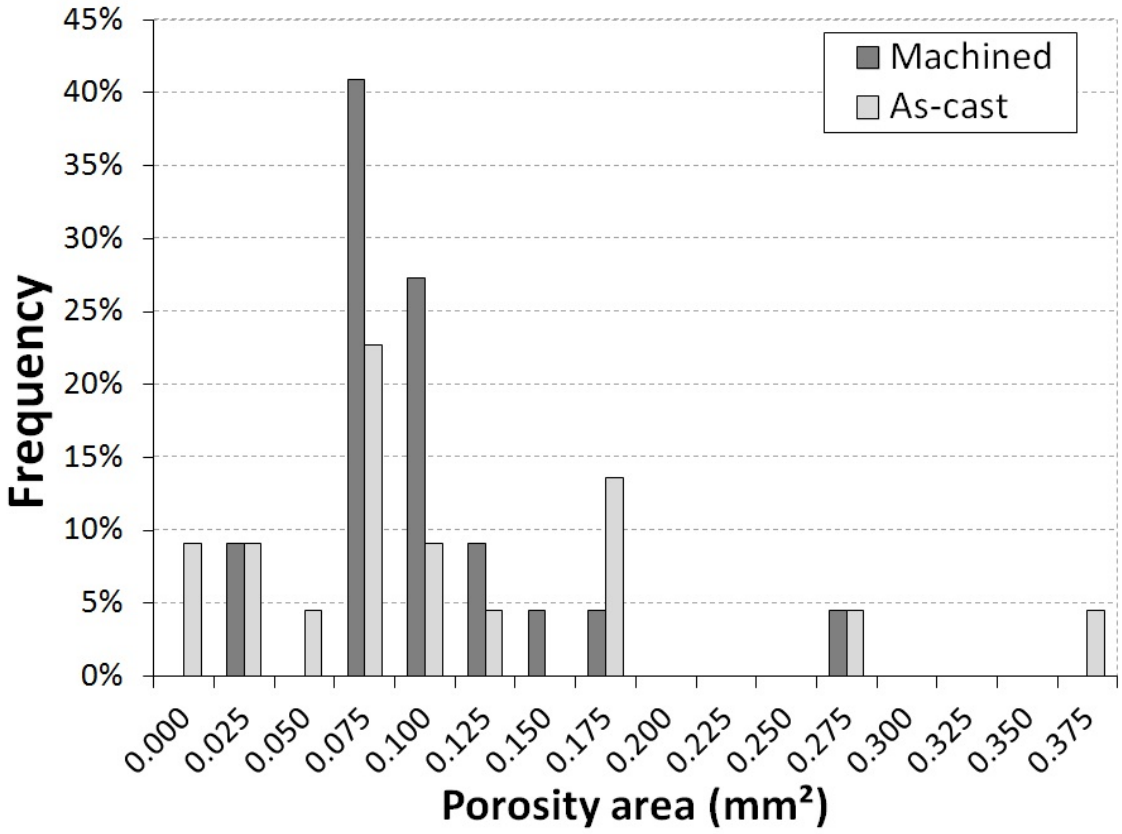

Figure 45. Histogram of critical pore area for machined and as-cast fatigue test specimens.

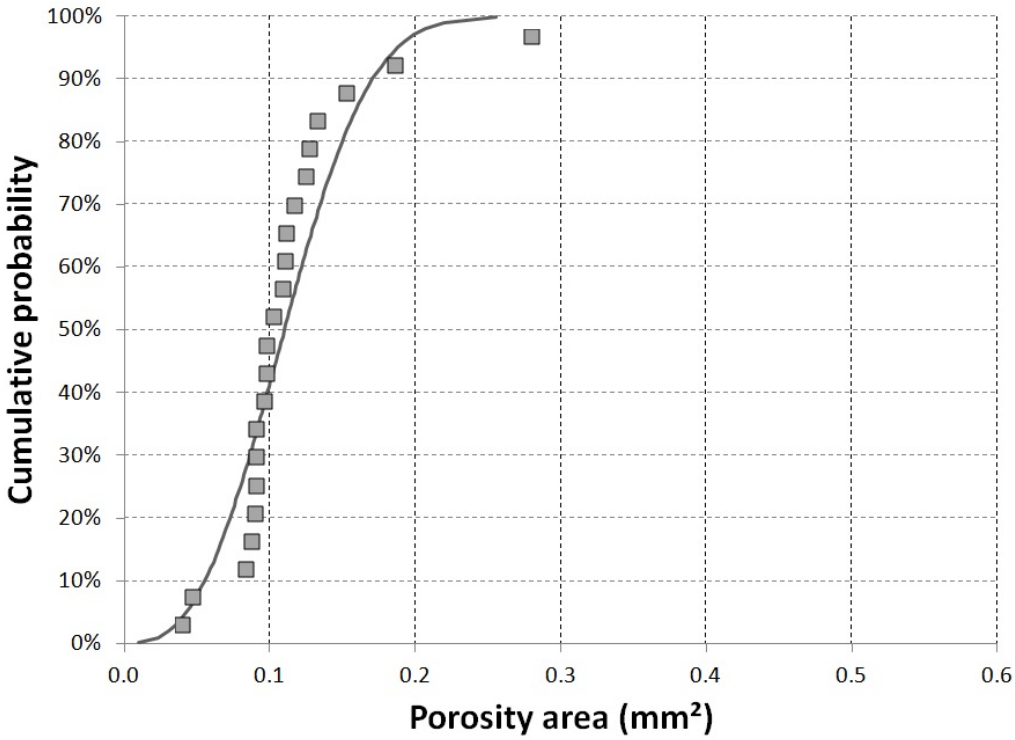

Figure 46. Weibull distribution of critical pore area for machined fatigue test specimens (α=0.13 mm², β=2.73).

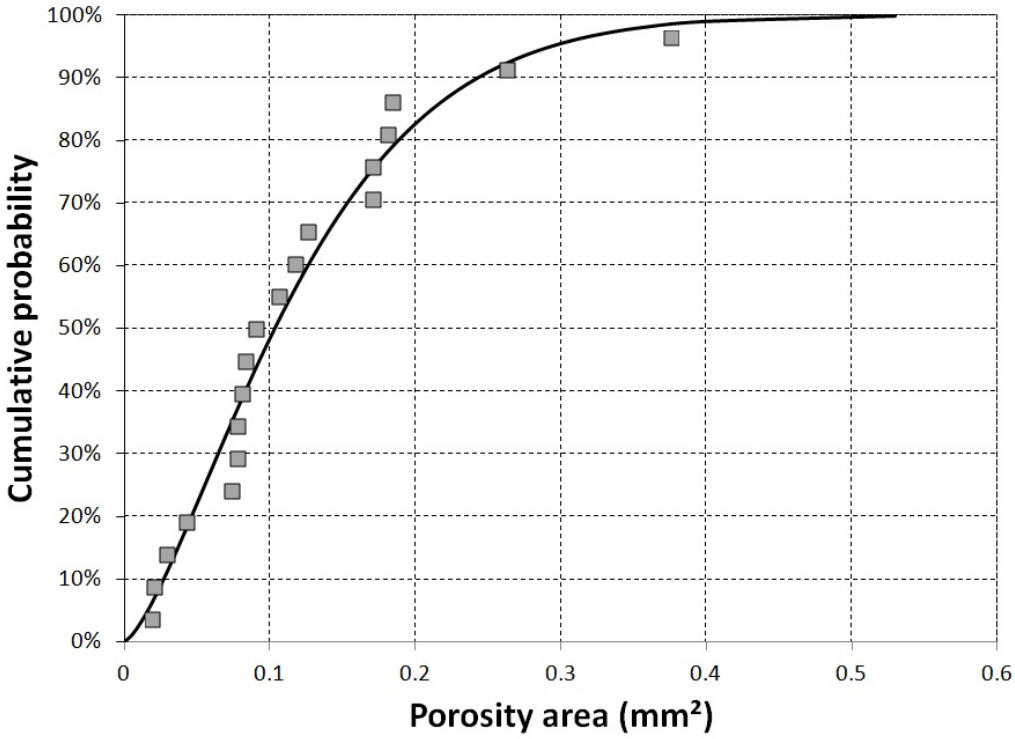

Figure 47. Weibull distribution of critical pore area for as-cast fatigue test specimens (α=0.13 mm², β=1.41).

4.5 EFFECT OF PORE SIZE ON FATIGUE LIFE

In order to evaluate the effect of defect size on fatigue life, the equivalent alternating stress found using the Walker equation was multiplied by the fourth root of the area of the critical pore. This gave a result in units of MPa√m. While these are units as stress intensity, it should not be interpreted as a stress intensity factor. Evaluating the stress intensity factor would require the application of linear elastic fracture mechanics, which is beyond the scope of this thesis. It is simply a means of taking the porosity size into account for comparison purposes.

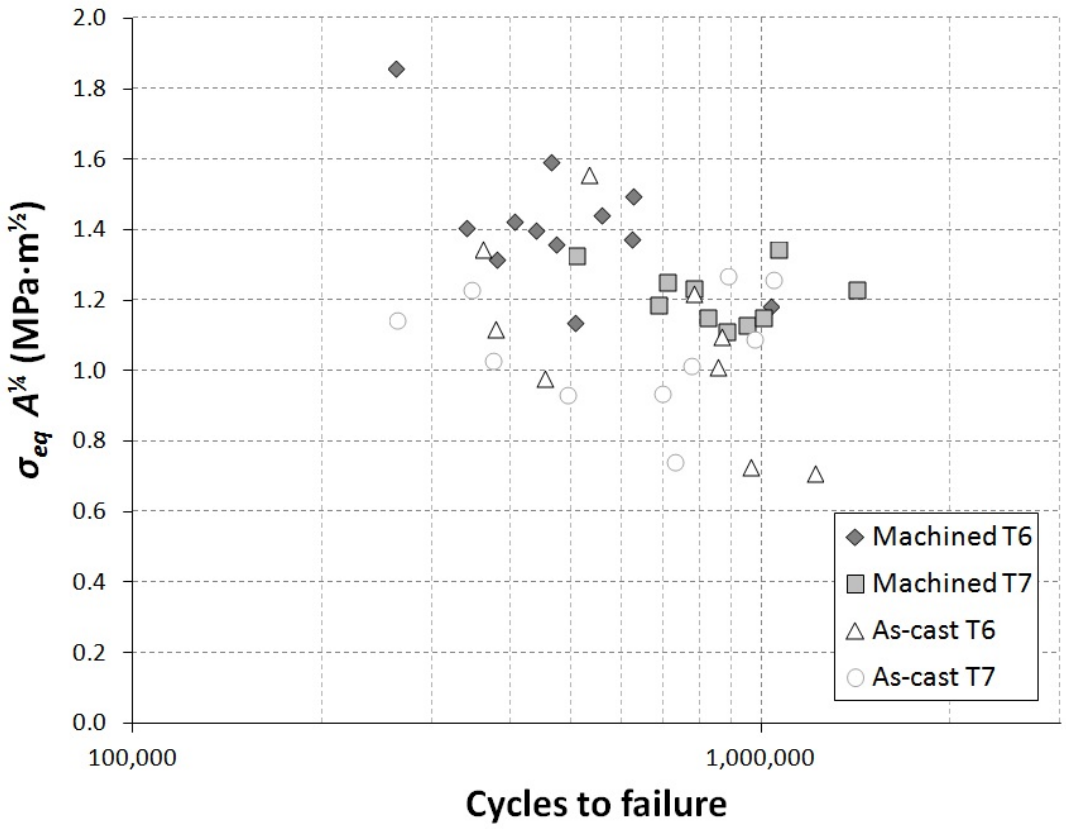

Figure 48. Equivalent stress times fourth root of porosity area vs. cycles to failure for lost foam 356.

CHAPTER 5 – CONCLUSIONS

5.1 EFFECTS OF MEAN STRESS ON FATIGUE BEHAVIOR

The results of this study demonstrate that, for lost foam cast aluminum alloy 356, widely-used mean stress equations (Goodman, Soderberg, Morrow, Gerber, and ASME-Elliptic) give highly non-conservative results, consistently overpredicting fatigue lives by large factors. This is consistent with the findings of Dowling's 2009 meta-analysis, which included 28 separate datasets (18 for steels, nine for wrought aluminum alloys, and one for a titanium alloy), but did not include any cast aluminum alloys. This suggests that Dowling's findings have general applicability, and calls into question the continued use of these equations in engineering education and licensing examinations. Given their poor ability to accurately predict fatigue lives, these equations should be considered as having only historical value.

The three mean stress equations that contain fitting parameters (Stulen, Topper-Sandor, and Walker) all provided reasonably accurate results. The Topper-Sandor and Walker equations performed slightly better than the Stulen equation. Values for the fitting parameters for each equation have been determined. The values of these parameters appear to be determined primarily by the heat treatment condition of the aluminum (T6 or T7), rather than the surface condition (as-cast or machined). This indicates that the underlying behavior is largely related to microstructural parameters.

A possible explanation for this can be found in the results of Kirby and Beevers (115), who noted that *R*-ratio effects disappeared in ultra-high vacuum. The 2011 work of Chawla et al (116), comparing fatigue crack growth rates for 7075-T651 aluminum under different *R*-ratios in ultra-high vacuum, dry air, and moisture, sheds additional light on this. In that study, the formation of oxide on the crack surfaces, the absorption of atomic hydrogen (produced in the oxidation of aluminum by water) at the crack tip, and the possible lubricating effect of water on the crack surface (preventing crack re-welding) were identified as the mechanistic factors responsible for the differences in fatigue crack behaviors.

The works cited above suggest that oxidation phenomena on the crack surface are the key to understanding *R*-ratio effects. Based on this insight, it could be generalized that materials with greater corrosion resistance will have less mean stress sensitivity, while materials with less corrosion resistance with have greater mean stress sensitivity. In the current study, it was found that lost foam aluminum alloy 356, mean stress sensitivity was greater in condition T6 than condition T7. It is hypothesized that this is due to greater corrosion resistance in the T7 condition. For other aluminum alloys (such as the wrought alloys 2024 and 7075), it is known that corrosion resistance is greater in the T7 condition. Future work will include characterization of the corrosion behavior of lost foam cast aluminum alloy 356 in the T6 and T7 conditions.

5.2 EFFECTS OF CAST SURFACE ON STATIC AND FATIGUE PROPERTIES

Specimens with a cast surface had significantly lower yield strength, tensile strength, elongation, and fatigue strength compared to specimens with a machined surface, for both conditions T6 and T7. The fatigue life of as-cast specimens was found to be approximately 60 – 70% lower than that of machined specimens at the same equivalent stress.

Initially, it was expected that fatigue cracks in as-cast specimens would initiate from surface defects of the type seen in Figure 3. In fact, all of the fatigue cracks initiated from pores, in both the as-cast and machined specimens. As Figure 25 shows, the surface of the as-cast specimens was not as "beady" as that of the engine block shown in Figure 3. The simple rectangular geometry of the test plate mold facilitated pattern fusion, resulting in an average pattern permeability of 4.3 cm/sec. Therefore, the test specimens did not replicate the "beady" surface seem in castings with more complex geometry and lower degrees of pattern fusion.

In spite of this, the as-cast specimens still had significantly lower fatigue lives than the machined specimens. This cannot be correlated directly to the pore size. Although the as-cast specimens showed greater variation in the pore size, the average pore size for both as-cast and machined specimens was similar (0.0120 mm^2 for as-cast specimens vs. 0.0115 mm^2 for machined specimens). Even when accounting for the porosity area, as shown in Figure 48, the as-cast specimens still had a lower fatigue life at the same applied stress intensity.

The lower fatigue lives of the as-cast specimens, as well as the lower elongation, may be attributable to the presence of oxide films, as shown in Figure 35. Littleton et al (27) have shown that pattern permeabilities greater than 0.5 cm/sec promote "fingering" during mold filling. For these specimens, the average pattern permeability was 4.3 cm/sec. While this is too low to result in a macroscopically "beady" texture, it is high enough to result in an uneven metal front. This results in film formation, where foam pyrolysis products are trapped between separate metal fronts. As Campbell has argued convincingly in his book (137), films have a deleterious effect on the ductility and fatigue life of castings. Wang et al (133) found that lost foam 356 castings had shorter fatigue lives than lost foam A356 castings, and showed that this was due to more rapid crack propagation in 356 due to the presence of brittle iron-based intermetallics. The effect of foam pyrolysis products near the surface can be seen in a similar way. Based on this, it may be concluded that the best way to improve the fatigue life of lost foam castings in the as-cast state would be to minimize the presence of oxide films.

5.3 EFFECTS OF POROSITY ON FATIGUE BEHAVIOR

As discussed above, all of the fatigue cracks observed could be traced back to pores. In general, under the same conditions of stress, larger pores resulted in a shorter fatigue life. However, there were many exceptions to this. For example, a machined 356-T6 specimen cycled between ±80.9 MPa that failed in 1,031,085 cycles was found to have an initiating pore of 0.05 mm², while another machined 356-T6 specimen cycled in

the same stress range that failed in less than half the number of cycles (504,488) had a smaller initiating pore (0.04 mm²). Furthermore, the initiating pore was not necessarily the largest pore observed in the specimen. More sophisticated approaches, such as the approach described by Tijani et al (31), take into account the location and three-dimensional shape of casting defects, rather than their projected area on the fracture surface. It is possible that such an approach would provide a better correlation to fatigue life. However, the practical application of such an approach is hampered by the fact that the size, geometry, and location of casting defects are not generally known a priori, but must be determined by non-destructive testing. A reduction in porosity would certainly lead to an increase in both monotonic and fatigue properties. However, as Figure 48 shows, the shorter fatigue lives of as-cast specimens as compared to machined specimens cannot be attributed to porosity.

CHAPTER 6 – FUTURE WORK

6.1 IMPROVED TESTING METHODS

One drawback of the constant-radius fatigue specimen used in this study is that the tensile stress is not constant. Due to the presence of porosity, failures did not always occur in the section of least nominal cross-section. The non-uniform stress distribution may have introduced some additional scatter into the data.

Many researchers investigating fatigue in cast materials – for example, Zhai (138) – have made use of a four-point bending setup. In four-point bending, there is a constant stress at the outer surface of the specimen between the two upper rollers. However, typical four-point bending fixtures are only capable of load ratios of $R \geq 0$. Therefore, a four-point bending fixture capable of fully-reversed loading has been designed and built. This fixture will be described below.

The present study has found a difference in stress ratio sensitivity between 356-T6 and 356-T7, and it has been hypothesized that this difference may be related to differences in corrosion resistance. Certainly, there is a significant body of literature showing that stress ratio effects are influenced by environmental conditions. Based on this, it seems reasonable to suspect that fatigue testing results performed on a given material in laboratory air may not reflect the behavior of the same material under other environmental conditions. Particularly with marine outboard engine applications in

mind, it appears that there is a need to understand the fatigue behavior of lost foam cast aluminum alloy 356 in saltwater. To this end, means of conducting corrosion-fatigue experiments in simulated seawater have been developed, which will also be described below.

6.1.1 FULLY-REVERSED FOUR POINT BENDING FATIGUE FIXTURE

A shear force and bending moment diagram for four point bending is shown in Figure 49, on the following page. A rectangular specimen is supported on rollers at *A* and *D*, while a load of *F*/2 is applied at *B* and *C*. From static equilibrium, it can be seen that the reactions at the supports *A* and *D* are also equal to *F*/2. The shear force V_y in the span *AB* is *F*/2. Since the shear force is constant in this span, the bending moment M_z increases linearly with distance, reaching a maximum value of $FL_a/2$ at *B*. In the span *BC* (i.e. between the two load rollers), the shear force is zero, and the bending moment is constant. In the span *CD*, the shear force is –*F*/2, and the bending moment decreases linearly, to a value of zero at *D*.

The normal stress (σ_x) in the specimen is a function of the bending moment M_z, the distance *y* from the neutral axis, and the moment of inertia I_x. Since the bending moment is constant in the span *BC*, the normal stress as a function of distance from the neutral axis is also constant in this span. The maximum tensile stress occurs along the lower surface in the span *BC*; the minimum stress has an equal magnitude but is compressive in sign, and occurs along the upper surface. For a rectangular specimen of width *b* and thickness *h*, the maximum stress is given by Equation 21.

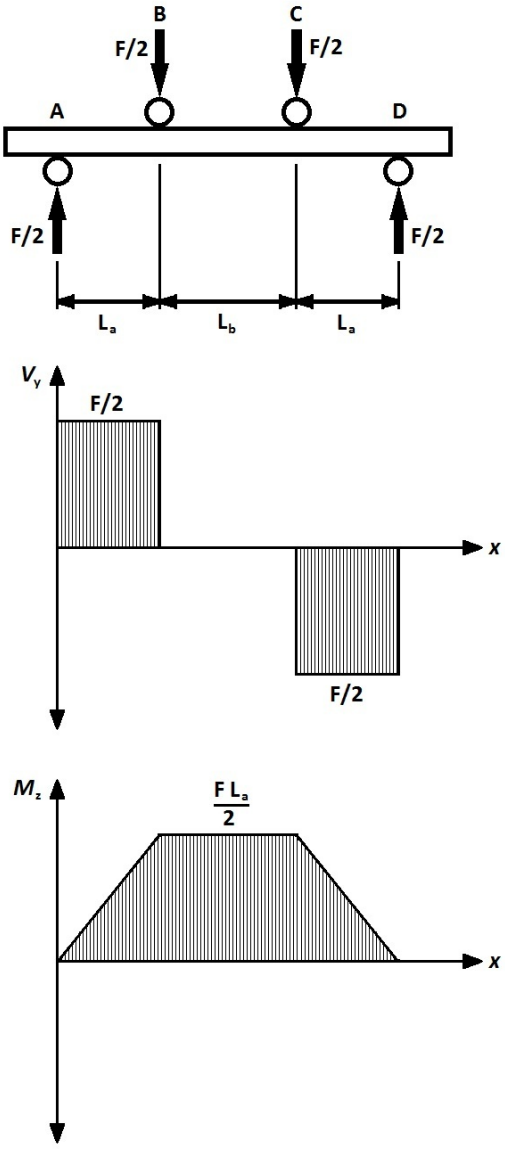

Figure 49. Shear force and bending moment diagram for four-point bending.

$$\sigma_{max} = \frac{M_z y}{I_x} = \frac{3FL_a}{bh^2}$$

Equation 13. Maximum stress for four-point bending of rectangular specimen, where:
σ_{max} = maximum normal stress (MPa)
M_z = bending moment about z-axis (N·mm)
y = distance from neutral axis (mm)
I_x = area moment of inertia about x-axis (mm^4)
F = applied load (N)
L_a = distance from support roller to load roller (mm)
b = specimen width (mm)
h = specimen thickness (mm)

An advantage of this test setup is that the normal stress (at the specimen surface) is constant between the two load rollers. Unlike a cyclic tension or tension-compression test, the stress is not constant through the specimen thickness; however, since fatigue cracks nearly always initiate at or near the specimen surface, this may not be a problem. Four-point bending tests are often used for ceramics and other brittle materials, which would break at the grips in a tension test.

Zhai et al (138), among others, have performed four point bending fatigue tests on cast aluminum alloys. However, the setup shown in Figure 49 is only capable of load ratios of $R \geq 0$, since the force applied by the load rollers can only be in one direction. Therefore, a four point bending fatigue fixture capable of fully-reversed loading was designed and built. This fixture has an additional set of rollers, two directly above the support rollers and two directly below the load rollers. The distance between the two sets of rollers is such that the distance from the specimen surface to the second set of rollers is $h/2$, where h is the specimen thickness. This is shown in Figure 50, below.

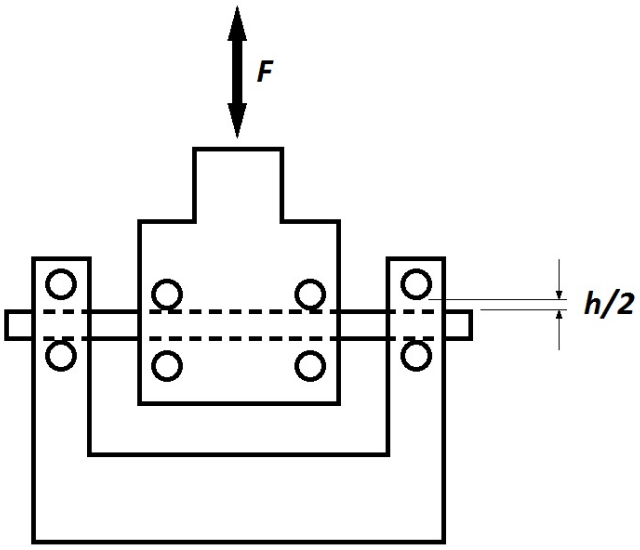

Figure 50. Schematic of fully-reversing four-point bending fatigue fixture.

The gap between the specimen and the second set of rollers is necessary in order to ensure that the specimen can bend freely at the loading points and supports during each load cycle. As a result of the gap, there will be a slight interruption between the tensile and compressive portions of the load cycle, as illustrated in Figure 51. This interruption represents the time between when the first set of rollers disengages from the specimen and when the second set of rollers engages with the specimen.

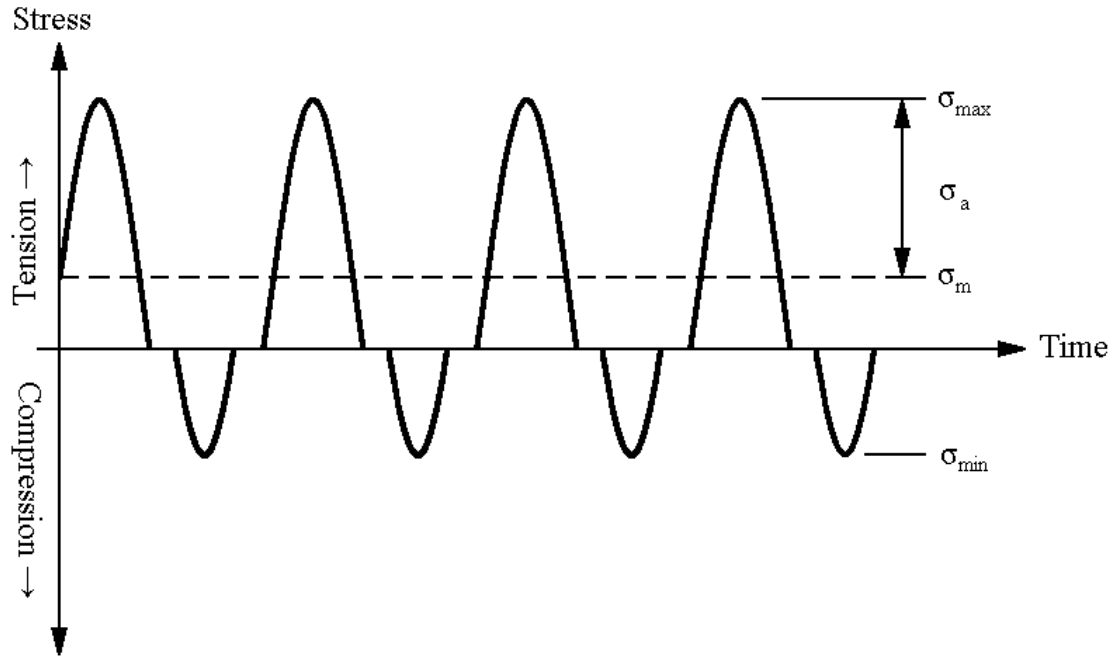

Figure 51. Stress vs. time for fully-reversing four-point bending fatigue fixture.

A fully-reversing four-point bending fatigue fixture, as described above, has been built. The fixture is made from 17-4 PH stainless steel hardened to condition H1075, while the rollers are made from type 416 stainless steel. This ensures that the fixture and the rollers will be substantially harder than a cast aluminum specimen, and will not wear during testing.

The four-point bending fatigue fixture will be used in the next round of testing. In the next round of testing, specimens with both higher pattern permeability (to replicate the "beady" texture of actual lost foam castings) and lower pattern permeability than the specimens used in the current study will be tested. In addition, chills will be used, in order to vary the solidification rate and DAS.

Since the fully-reversed four-point bending fatigue fixture described above was designed, Amiri and Cavalli (139) have described the use of a similar fixture in the testing of carbon fiber reinforced plastics. However, it does not appear that such a fixture has been used in the testing of metallic materials until now. It is believed that this fixture will be of benefit in testing stress ratio effects in the fatigue of specimens with an as-cast surface.

6.1.2 CORROSION-FATIGUE TESTING IN SIMULATED SEAWATER

In the present study, it was found that the stress ratio sensitivity of lost foam cast 356-T6 was greater than that of lost foam cast 356-T7, regardless of the surface condition (as-cast or machined). Based on the work of Kirby and Beevers (115) and Chawla et al (116), it is hypothesized that this is due to differences in corrosion resistance between the two tempers. In the next round of testing, polarization resistance testing will be performed in order to verify this hypothesis.

The work of the previously-cited authors highlights the importance of environmental effects in fatigue. This suggests that fatigue tests performed in laboratory air may not be representative of the performance of castings in marine applications.

There is no reason why fatigue testing must be performed in air. The four-point bending fatigue fixture described above may be immersed in a fluid, such as salt water. (A sacrificial anode may be attached to the test fixture in order to ensure that it does not corrode). A recirculating pump may be attached to the container of fluid in order to obtain a desired water velocity. The temperature of the water may be controlled by means of a heater and temperature controller. In addition, the specimen may be polarized to a desired potential (relative to a standard electrode) by means of a potentiostat. Wet/dry cycles could be also incorporated into the test by pumping the fluid out of the container at regular intervals, then pumping it back in.

In this way, fatigue tests may be performed under conditions more accurately representing marine service.

6.2 METHODS OF IMPROVING PROPERTIES OF LOST FOAM CASTINGS

As discussed above, this study revealed that the ductility and fatigue life of as-cast specimens were significantly lower than those of machined specimens. This reduction could not be attributed to pore size alone, and is thought to be due to the presence of

films. Therefore, reducing film formation may be the best way to improve the fatigue strength of lost foam castings.

According to Littleton et al (27), uneven mold filling and multiple flow fronts occur when pattern permeability exceeds 0.5 cm/sec. The average pattern permeability for the test plates used in this study was 4.3 cm/sec., well beyond the suggested limit. Littleton has suggested that applying mechanical vibration to the pattern tool during the blowing process can increase pattern fusion. The results of the present study suggest that increasing pattern fusion could improve the fatigue properties of lost foam castings. Future work will investigate the effect of pattern fusion.

Film formation is believed to occur when liquid pyrolysis products are trapped between two advancing metal fronts. Therefore, more effective removal of pyrolysis products may also reduce film formation. The application of vacuum during mold filling (65, 75, 77) may provide a means of removing pyrolysis products. However, the application of vacuum will need to be carefully controlled to avoid high metal velocities that promote collapse mode (25).

Campbell (137) has suggested that reduced dendrite arm spacing can mitigate some of the deleterious effects of films. Fan et al (87, 88) have shown that the application of mechanical vibration during solidification can reduce DAS and improve the mechanical properties of lost foam castings. Since vibrating tables are already present in the melt area of all lost foam foundries, this is a technique that could be applied

without much additional expenditure in existing foundries. It is definitely worthy of future study.

Another possible means of reducing DAS is the use of chills. A U.S. patent for a chill-enhanced lost foam casting process was issued to Ryntz and Bommarito in 1985 (140). However, Ryntz and Bommarito proposed directly gluing a copper chill to an EPS pattern prior to coating. In 1997, Simpson (141) measured the effect of copper, steel, and graphite chills on DAS in lost foam cast A356, and found a reduction in DAS of up to 50% using a 25 mm thick copper chill. However, a drawback of this method is that the pattern and glue pyrolysis products have no way to escape into the sand. An alternative means of applying a chill to lost foam castings is to clamp a metal plate to the EPS pattern after it has been coated. This is shown in Figure 52, on the following page. This method is said to be used by a European automotive manufacturer. An advantage of this method is that pyrolysis products may be drawn into the coating, rather than being trapped on the surface of the casting. Preliminary testing at BRP using a 9.5 mm steel plate showed a 30% reduction in DAS in a thick section of an engine block casting, and a 50% reduction in DAS in a thin section.

Campbell (86, 137) has also suggested that solidification under pressure may partially "heal" films. Solidification under pressure has been applied to lost foam castings with great success in the past few years (50, 70, 71, 72, 73). It is known to reduce porosity, and is claimed to have resulted in a 100% increase in elongation and a 50% increase in fatigue strength for A356 castings at Mercury Marine, although the data

supporting these claims have not been published. Although the initial capital cost associated with this process would be high, it appears to be worthy of further study.

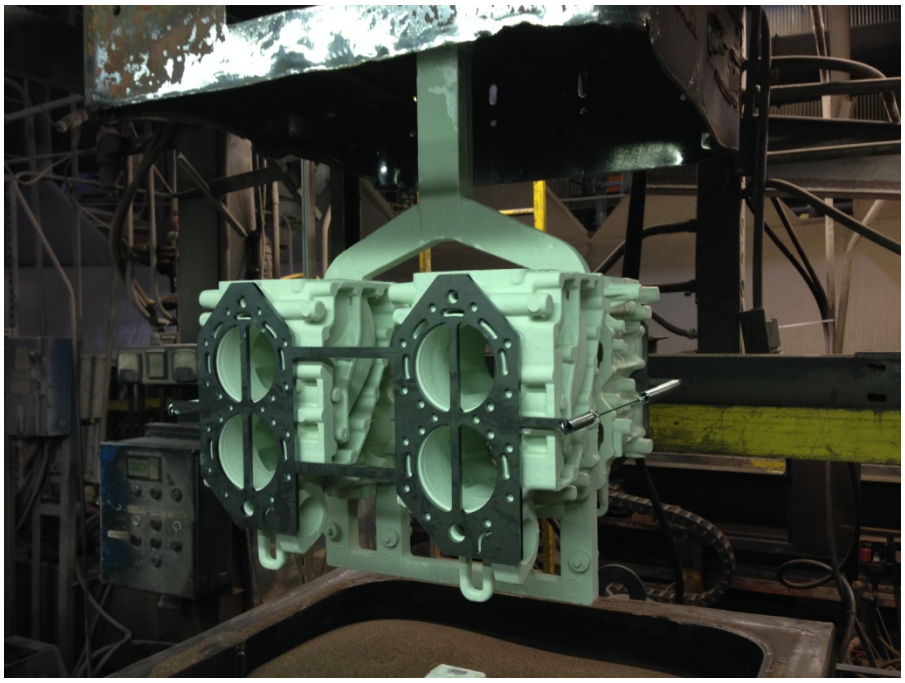

Figure 52. Steel chill clamped to the deck face of a coated EPS engine block pattern.

CHAPTER 7 – FINAL THOUGHTS

What follows are a series of brief reflections on the implications of this work as they relate to industry, engineering education, the engineering profession, and society as a whole.

Lost foam casting is a highly versatile manufacturing process that offers significant benefits in terms of design flexibility, energy consumption, and environmental impact. One of the major impediments to the more widespread adoption of the lost foam casting process is the perception of inferior mechanical properties compared to other casting techniques. As this study shows, for aluminum alloy 356, this perception is justified, particularly for specimens with an as-cast surface. However, the results of this study suggest that reductions in oxide films, along with reductions in porosity, could potentially improve the mechanical properties of lost foam aluminum castings. If this can be achieved – and there are many promising techniques for doing so – the lost foam casting process might be adopted on an even larger scale.

The Goodman diagram is a mainstay of engineering education. Some version of it can be found in nearly every textbook on mechanical engineering design or mechanical properties of materials. It is included in engineering licensure examinations, including the NCEES Fundamentals of Engineering and Principles and Practice of Engineering exams. The results of this study add to a growing body of work suggesting that it is time for this diagram to be retired. More accurate equations are now available, which better

reflect the underlying physical behavior. The use of these newer equations should be encouraged. If the Goodman, Gerber, and Soderberg equations are discussed at all, it should only be in the context of the historical development of our present understanding of fatigue.

Since the work of Kirby and Beevers in the 1970s, which showed that *R*-ratio effects disappear in ultra-high vacuum, it has been recognized – at least, in the fatigue and fracture literature – that mean stress sensitivity is largely a function of oxidation at crack surfaces. However, the implications of this do not seem to have been broadly recognized in day-to-day engineering practice. Corrosion fatigue continues to be viewed as a specialized failure mode, and the influence of environment on fatigue tends not to be considered unless a fatigue crack initiates from a corrosion pit. In fact, an ample body of work demonstrates that all fatigue (except in ultra-high vacuum) is influenced by corrosion to some extent. As described in Chapter 6, future work will explicitly include environmental effects.

Fatigue failures cause many billions of dollars of losses to the world economy each year. This represents a loss, not only of physical objects, but of the human effort (mental and physical) embodied in them. Much more importantly, fatigue failures under certain circumstances may lead to injury or loss of life. Preventing fatigue failures, to the greatest extent possible, is therefore a moral imperative for engineers. To the extent that the present work leads to improvements in current engineering practice, it will have been successful.

REFERENCES

1. H.F. Shroyer, "Cavityless Casting Mold and Method of Making Same," U.S. Patent 2,830,343, April 15, 1958.

2. A. Duca, M.C. Flemings, and H.F. Taylor, Art Casting, Massachusetts Institute of Technology, Cambridge, MA, 1963.

3. The lost foam process was adopted in the United States by General Motors in 1980, by Ford in 1982, by Outboard Marine Corporation in 1983, and by Mercury Marine in 1985; in Italy by Teksid (a division of Fiat) in 1983; and in Germany by BMW in 1993. See M.J. Lessiter, "A look back at the 20th century – lost foam casting," Modern Casting 90, 11:54-55, November 2000.

4. For a brief account of fatigue intended for the general reader, see D. Palmer, "Understanding Fatigue Failures," Design News (online edition), April 9, 2012, http://www.designnews.com/author.asp?section_id=1365&doc_id=241687.

5. Y. Murikami, Metal Fatigue: Effect of Small Defects and Nonmetallic Inclusions, Elsevier, Oxford, UK, 2002.

6. ASTM Standard E1823, 2010a, "Standard Terminology Relating to Fatigue and Fracture Testing," ASTM International, West Conshohocken, PA, 2010, DOI: 10.1520/E1823-10A.

7. See, for example, J.E. Shigley, C.R. Mischke, and R. Budynas, Mechanical Engineering Design (7th ed.), McGraw-Hill, New York, NY, 2004. This text also includes the ASME elliptic criteria.

8. J. Goodman, Mechanics Applied to Engineering, Longman, Green, and Company, London, UK, 1899.

9. B.P. Haigh, "Experiments on the fatigue of brasses," Journal of the Institute of Metals 18:55-86, 1917.

10. C.R. Soderberg, "Factor of safety and working stress," Transactions of the American Society of Mechanical Engineers 52, 1930.

11. H.G. Gerber, "Bestimmung der zulässigen spannungen in eisen-constructionen," Zeitschrift des Bayerischen Architekten und Ingenieur Vereins 6:101, 1874. A contemporary English-language account of Gerber's work can be found in the appendix to J.J. Weyrauch and R.H. Thurston, Strength and Determination of the Dimensions of Structures of Iron and Steel with Reference to the Latest Investigations, John Wiley and Sons, New York, 1877.

12. C. Bagci, "Fatigue design of machine elements using the 'Bagci line' defining the fatigue failure surface line (mean stress diagram)," Mechanism and Machine Theory 16(4):339-359, 1981, DOI: 10.1016/0094-114X(81)90009-4.

13. S.-J. Wang, M.W. Dixon, C.O. Huey, Jr., and S.-C. Chen, "The Clemson limit stress diagram for ductile parts subjected to positive fatigue loading," Journal of Mechanical Design 122(1):143-146, 2000, DOI: 10.1115/1.533557.

14. F.B. Stulen, "Fatigue life data displayed by a single quantity relating alternating and mean stress," Technical Report AFML-TR-65-121, Air Force Materials Laboratory, Wright-Patterson Air Force Base, OH, 1965.

15. J. Morrow, in Fatigue Design Handbook, vol. 4, Society of Automotive Engineers, Warrendale, PA, 1968.

16. K.N. Smith, P. Watson, and T.H. Topper, "A stress-strain function for the fatigue of metals," ASTM Journal of Materials 5, 4:767-778, 1970.

17. K. Walker, "The effect of stress ratio during crack propagation and fatigue for 2024-T3 and 7075-T6 aluminum," Effects of Environment and Complex Load History on Fatigue Life, ASTM STP 462, American Society for Testing and Materials, West Conshohocken, PA, 1970, pp. 1-14.

18. T.H. Topper and B.I. Sandor, "Effects of mean stress and prestrain on fatigue-damage summation," Effects of Environment and Complex Load History on Fatigue Life, ASTM STP 462, American Society for Testing and Materials, West Conshohocken, PA, 1970, pp. 93-104.

19. B.N. Leis, "An energy based fatigue and creep-fatigue damage parameter," Journal of Pressure Vessel Technology (Transactions of the American Society of Mechanical Engineers) 99: 524-533, 1977.

20. American Foundrymen's Society, Final Report on Expendable Pattern Casting Technology – Phase I, National Technical Information Service, Springfield, VA, 1990.

21. American Foundrymen's Society, Expendable Pattern Casting Research – Phase II, National Technical Information Service, Springfield, VA, 1993.

22. H.E. Littleton, J. Griffin, D. Askeland, and C. Bates, Advanced Precision Expandable Casting Technology – Summary Report, University of Alabama at Birmingham, Birmingham, AL, 1995.

23. C.E. Bates, H.E. Littleton, D. Askeland, J. Griffin, B.A. Miller, and D.S. Sheldon, Advanced Lost Foam Casting Technology, University of Alabama at Birmingham, Birmingham, AL, 1996.

24. T. Molibog, B. Vatankhah, H.E. Littleton, C.E. Bates, and D. Askeland, Advanced Lost Foam Casting – 1997 Summary Report, University of Alabama at Birmingham, Birmingham, AL, 1997.

25. C.E. Bates, H.E. Littleton, D. Askeland, T. Molibog, J. Hopper, and B. Vatankhah, Advanced Lost Foam Casting Technology – Phase IV, University of Alabama at Birmingham, Birmingham, AL, 2000.

26. W. Sun, H.E. Littleton, and C.E. Bates, Final Report on Advanced Lost Foam Casting Technology – Phase V, University of Alabama at Birmingham, Birmingham, AL, 2005.

27. H.E. Littleton and J. Griffin, Final Report: Manufacturing Advanced Engineered Components Using Lost Foam Casting Technology, University of Alabama at Birmingham, Birmingham, AL, 2011.

28. W.A.J. Albert, "Über Treibseile am Harz," Archiv für Mineralogie, Geognosie, Bergbau, und Hüttenkunde 10: 215–234, 1838.

29. R.E. Peterson, "The interaction effect of neighboring holes or cavities, with particular reference to rocket cases and pressure vessels," Transactions of the ASME: Journal of Basic Engineering 87(4): 879-886, 1965.

30. O. Caty, J.-Y. Buffiere, E. Maire, and J. Adrien, "3D characterization of the influence of porosity on fatigue properties of a cast Al alloy," Advanced Engineering Materials 13(3): 194-198, 2011, DOI: 10.1002/adem.201000236.

31. Y. Tijani, A. Heinrietz, T. Bruder, and H. Hanselka, "Quantitative evaluation of fatigue life of cast aluminum alloys by non-destructive testing and parameter model," International Journal of Fatigue 57:73-78, 2013, DOI:10.1016/j.ijfatigue.2013.05.017.

32. R.A. Hardin and C. Beckermann, "Prediction of the fatigue life of cast steel containing shrinkage porosity," Metallurgical and Materials Transactions A 40 (3): 581-597, 2009, DOI: 10.1007/s11661-008-9755-3.

33. R. Kočená, S. Fintová, and G. Nicoletto, "Shrinkage pores and fatigue behavior of cast Al-Si alloys," Key Engineering Materials 465: 354-357, 2011, DOI:10.4028/www.scientific.net/KEM.465.354.

34. M.C. Flemings, "Metal casting innovations, 1952 – 2012 and beyond: a personal view," 60th Indian Foundry Congress, Bangalore, India, March 2–4, 2012.

35. T.R. Smith, "Method of casting," U.S. Patent 3,157,924, November 24, 1964.

36. A. Wittmoser, E. Krzyzanowski, and J. Schade, "Gassifiable casting pattern," U.S. Patent 3,314,116, April 18, 1967.

37. Full Mold Process v. Central Iron Foundry, 489 F. Supp. 893, May 13, 1980.

38. S. Gibbs, "BRP sells lost foam inside and out," Modern Casting 102, 2:24-28, February 2012.

39. K. Siavashi, C. Topping, and W.D. Griffiths, "The effect of reducing molecular weight of the foam pattern on the porosity of Al alloy castings in the lost foam casting process," 11th International Aluminum Conference (INALCO 2010), Eindhoven, Netherlands, June 23 – 25, 2010.

40. See J.G. Santangelo, R.G. Sinclair, R.D. Tenaglia, and J.J. Weber, "Method for producing metal castings," U.S. Patent 4,633,929, October 16, 1985; M.J. Cannarsa, H.S. Kesling Jr., and H.-N. Sun, "Process for preparing polycarbonate copolymer foam suitable for lost foam casting," U.S. Patent 4,773,466, December 14, 1987; and R.J. Donahue, "Method of lost foam casting of aluminum-silicon alloys," U.S. Patent 5,950,851, August 4, 1998.

41. M. Patz and T.S. Piwonka, "Lost foam casting," in D.M. Stefanescu, ed., ASM Handbook (9th ed.), vol. 15: Casting, ASM International, Materials Park, OH, 1992.

42. S. Kumar, P. Kumar, and H.S. Shan, "Density optimization of slurry of coating material used in the EPC process through Taguchi's parameter design approach," Materials and Manufacturing Processes 23(7):719-725, 2008, DOI: 10.1080/10426910802317128.

43. C.A. Goria, G. Serramoglia, G. Caironi, and G. Tosi, "Coating permeability: a critical parameter of the evaporative casting process," Transactions of the American Foundrymen's Society 94:589-600, 1986.

44. G. del Gaudio, G. Serramoglia, G. Caironi, and G. Tosi, "Aspects concerning the role of coatings in the production of iron castings by the 'Policast' process," Metallurgical Science and Technology 3(3):76-86, 1985.

45. C. Ravindran, B. Jue, and J. Karpynczyk, "Permeability of coating in EPC process," Transactions of the American Foundrymen's Society 101:955-959, 1993.

46. X. Chen and D. Penumadu, "Permeability measurement and numeric modeling for refractory porous materials," Transactions of the American Foundry Society 116:1045-1059, 2008.

47. B. Matz and D.C. Kearney, “Method of drying refractory coated foam patterns,” U.S. Patent Number 4,728,531, March 1, 1988.

48. R.D. Butler and R.J. Pope, "Some factors involved in full mould casting with unbonded sand molds," British Foundryman 4:178-191, 1964.

49. Q. Zhao, J.T. Burke, and T.W. Gustafson, "Foam removal mechanism in lost foam casting," Transactions of the American Foundry Society 110:1399-1414, 2002.

50. F. Sonnenberg, ed., Lost Foam Casting Made Simple, American Foundry Society, Schaumburg, IL, 2008.

51. M.R. Barone and D.A. Caulk, "A foam ablation model for lost foam casting of aluminum," International Journal of Heat and Mass Transfer 48:4132-4149, 2005, DOI:10.1016/j.ijheatmasstransfer.2005.03.031.

52. D.A. Caulk, "A foam melting model for lost foam casting of aluminum," International Journal of Heat and Mass Transfer 49:2124-2136, 2006, DOI:10.1016/j.ijheatmasstransfer.2005.12.007.

53. D.A. Caulk, "A pattern decomposition model for lost foam casting of aluminum, part III – Collapse mode," Transactions of the American Foundry Society 115:833-844, 2007.

54. D.A. Caulk, "A foam engulfment model for lost foam casting of aluminum," International Journal of Heat and Mass Transfer 49:3831-3845, 2006, DOI:10.1016/j.ijheatmasstransfer.2006.04.015.

55. M.J. Ainsworth, "Metal-foam interface stability during the filling of lost foam moulds with aluminum alloys," Ph.D. thesis, University of Birmingham, 2010.

56. R. Ajdar, "The effect of mold materials on solidification, microstructure, and fluidity of A356 alloy in lost foam casting," M.S. thesis, University of Toronto, 2001.

57. K. Siavashi, "The effect of casting parameters on fluidity and porosity in the lost foam casting process," Ph.D. thesis, University of Birmingham, 2011.

58. R. Albonetti, "Porosity and intermetallic formation in lost foam casting of 356 alloy," M.S. thesis, University of Western Ontario, 2001.

59. R.D. Stephens, C.S. Wheeler, and M. Pryor, "Life cycle assessment of aluminum casting processes," 2001 SAE Environmental Sustainability Conference and Exhibition, Graz, Austria, April 8, 2001.

60. M.C. Ashton, S.G. Sharman, and A.J. Brookes, "The Replicast FM (full mold) and CS (ceramic shell) process," Transactions of the American Foundrymen's Society 92:271-280, 1984.

61. K.A. Guler, Z. Taslicukur, and G. Ozer, "Expanded polystyrene (EPS) pattern application in investment casting and chemical removing," Materiały Ceramiczne 63(1): 138-142, 2011.

62. R. Hoffman and A. Wittmoser, "Magnetizable mass casting device," U.S. Patent 3,619,866, November 16, 1971.

63. E.I. Belov and B.V. Rabinovich, "The structure of magnetic mold iron castings," Liteinoye Proizvodsto (7):11-12, 1982.

64. J. Goñi, "The innovative casting process for the improvement of the competitiveness and working conditions of the European foundries," Fundación INASMET, Bizkaia, Euskal Herria, Spain, 2006.

65. S.-R. Shin, S.-W. Han, and K.-W. Lee, "Gas pore formation in lost foam casting of AZ91H Mg alloy in comparison with A356 Al alloy," Materials Transactions 46(10):2204-2210, 2005.

66. J.T. Berry, R. Luck, B. Zhang, and R.P. Taylor, The Effect of Applied Pressure During Feeding of Critical Cast Aluminum Alloy Components With Particular Reference to Fatigue Resistance, Mississippi State University, Mississippi State, MS, 2003.

67. H.M. Howe, "Metallurgy of steel," Engineering and Mining Journal 46(3):47-48, 1888.

68. D. Hanson and I.G. Slater, "Unsoundness in aluminium sand-castings, part III – Solidification in sand moulds under pressure," Journal of the Institute of Metals 56:103-124, 1935.

69. M. Garat, "Process for lost foam casting of metal parts," U.S. Patent 5,058,653, October 22, 1991.

70. R. Donahue, "New developments that improve competitiveness and open market opportunities," AFS International Lost Foam Conference, Frankenmuth, MI, October 24, 2001.

71. B. Kang, Y. Kim, K. Kim, G. Cho, K. Choe, and K. Lee, "Density and mechanical properties of aluminum lost foam casting by pressurization during solidification," Journal of Material Science and Technology 23(6):828-832, 2007.

72. R. Donahue and K. Anderson, "Lost foam casting," in ASM Handbook (10th ed.), vol. 15: Casting, ASM International, Materials Park, OH, 2008.

73. S.B. Ghanti, E.A. Druschitz, A.P. Druschitz, and J.A. Griffin, "The effects of solidification under pressure on the properties of A206-T6 cast aluminum alloy," Transactions of the American Foundry Society 119:109-116, 2011.

74. J.A. Taylor, "The effect of iron in Al-Si casting alloys," 35th Australian Foundry Institute National Conference, Adelaide, Australia, November 3, 2004.

75. H. Littleton, J. Griffin, and R. Foley, "Effect of vacuum assisted filling and solidification under pressure of A356, A206, 319M, and 535 aluminum alloys on tensile properties using the lost foam casting process," 118th Metalcasting Congress, Schaumburg, IL, April 8, 2014.

76. L. Lang, "Development and testing of a low pressure lost foam casting machine and an examination of the process," Ph.D. thesis, Freiburg University of Mining and Technology, 1999.

77. Z.-T. Fan and S. Li, "Low pressure lost foam process for casting magnesium alloys," Materials Science and Technology 21(6):727-734, 2005.

78. A.A. Luo, "Magnesium casting for structural applications," Journal of Magnesium and Alloys 1(1):2-22, 2013.

79. M.C. Flemings, Solidification Processing, McGraw-Hill, New York, NY, 1974.

80. http://en.cnki.com.cn.

81. P. Rohatgi, "Cast aluminum metal-matrix composites for automotive applications," Journal of Materials 43(4):10-15, April 1991.

82. K.A. Guler, A. Kisasoz, and A. Karaaslan, "A novel method for Al/SiC composite fabrication: lost foam casting," International Journal of Materials Research 102(3):304-308, 2011.

83. H.R. Pakzaman, M. Divandari, and A.R. Khavandi, "Effect of nickel coating of wire reinforcement on mechanical properties of aluminum matrix composites produced by lost foam casting," Iran International Aluminum Conference, Arak, Iran, May 15, 2012.

84. S.S.C. Ho, "Lost foam casting of periodic cellular materials with aluminum and magnesium alloys," M.S. thesis, University of Toronto, 2009.

85. D.K. Chernov, "Studies relating to the structure of cast steel billets," Zapiski Russkogo Tehnicheskogo Obshhestva 1:140-152, 1879.

86. J. Campbell, "Effects of vibration during solidification," International Materials Reviews 26(1):71-108, 1981.

87. Z. Zhao, Z.-T. Fan, X. Dong, B. Tang, D. Pan, and J. Li, "Influence of mechanical vibration on the solidification of a lost foam cast 356 alloy," China Foundry 7(1):24-29, 2010.

88. J. Li, Z.-T. Fan, X. Dong, W. Liu, X. Li, "Microstructure and mechanical properties of lost foam casting AZ91D alloy produced with mechanical vibration," Advanced Materials Research 213:5-8, 2011, DOI:10.4028/www.scientific.net/AMR.213.5.

89. V.R. Gervasi, F.Z. Shaikh, "Indirect rapid molds for prototype lost-foam pattern production," 11th Solid Freeform Fabrication Symposium, Austin, TX, August 10, 2000.

90. T. Grimm, User's Guide to Rapid Prototyping, Society of Manufacturing Engineers, Dearborn, MI, 2004.

91. C.W. Hirt and M.R. Barkhudarov, "Lost foam casting simulation with defect prediction," Modeling of Casting, Welding, and Advanced Solidification VIII Conference, San Diego, CA, June 7-12, 1998.

92. D. Zheng, Y. Wang, Y.-M. Deng, A. Yu, and W. Li, "Numerical simulation of lost foam casting in special-shaped stainless steel stirrer," Applied Mechanics and Materials 101-102:479-483, 2011.

93. E. Hepp, "Lost foam – möglichkeiten der simulation," 2nd Paderborn Symposium on Lost Foam, Paderborn, Germany, September 25-26, 2002.

94. G. Houzeaux and R. Codina, "Finite element modeling of the lost foam casting process tackling backpressure effects," International Journal of Numerical Methods for Heat and Fluid Flow 16(5):579-589, June 2006, DOI: 10.1108/09615530610669111.

95. S.M.H. Mirbagheri, R. Babai, M. Dadaszhadeh, M.T. Ahmadian, and P. Davami, "Simulation of mould filling in the EPC process," Scientia Iranica 11:69-80, April 2004.

96. K.A. Williams and D.M. Snider, Final Report: Development of a Computational Fluid Dynamics (CFD) Software Package to Support the Engineering of Lost Foam Pattern Blowing and Steaming, Arena-flow LLC, Albuquerque, NM, 2003.

97. J. Jiang, Z. Wu, L. Chen, and J. Hao, "Numerical simulation and analysis of mould filling process in lost foam casting," China Foundry 5(3):175-175, 2008.

98. W.D. Griffiths, "Lost foam at the crossroads," Foundry Trade Journal 3655:155-157, June 2008.

99. D.A. Caulk, "Modeling foam decomposition in lost foam casting," SIAM Great Lakes Section Spring Meeting, Rochester, MI, April 16, 2011.

100. M.A. Ainsworth, "Fundamentals of the lost foam casting process," presentation to the South African Institute of Foundrymen, Kempton Park, Guateng, South Africa, April 9, 2013.

101. Z.-M. Li and G.-Z. Liang, "Development and prospects of China's lost foam casting," International Lost Foam Conference, Asheville, NC, October 21, 2008.

102. M. Shahmiri and Y.H.K. Kharrazi, "The effects of gating systems on the soundness of lost foam casting (LFC) process of Al-Si alloy (A413.0)," International Journal of Engineering Transactions B 20(2):157-166, August 2007.

103. M. Karimian, A. Ourdjini, M. Hasbullah Idris, and H. Jafari, "Effect of pattern coating thickness on characteristics of lost foam Al-Si-Cu alloy casting," Transactions of Nonferrous Metals Society of China 22:2092-2097, 2012.

104. S.M. Emami, M. Divandari, E. Hajjari, and H. Arabi, "Comparison between conventional and lost foam compound casting of Al/Mg light metals," International Journal of Cast Metals Research 26(1):43-50, February 2013.

105. M. Khodai and S.M.H. Mirbagheri, "Behavior of generated gas in lost foam casting," World Academy of Science and Engineering 5:431-435, 2011.

106. A. Sharifi and M. Mansouri Hasan Abadi, "Investigation of gating parameters, temperature, and density effects on mold filling in the lost foam casting (LFC) process by direct observation method," Metallurgical and Materials Engineering 19(1):1-10, 2013.

107. S. Mohite, "Lost foam metal casting technology," Foundry Review 1(2):10-11, October 2012.

108. C. Neuebauer and M. Kölldorfer, "Fabricating the steel bull of Spielberg," in S. Brell-Cokcan and J. Braumann, eds., Rob | Arch 2012: Robotic fabrication in architecture, art, and design, Springer-Verlag, Vienna, Austria, 2013, pp. 131-138.

109. J.V. Poncelet, Introduction à la Méchanique Industrielle, Physique ou Expérimentale, 2nd Edition, L. Mathias, Paris, France, 1841.

110. S.P. Timoshenko, History of Strength of Materials, McGraw-Hill, New York, NY, 1953, pp. 162-173.

111. G.P. Sendeckyj, "Constant life diagrams – a historical review," International Journal of Fatigue 23:347-353, 2001.

112. S.H. Loewenthal, "Proposed design procedure for transmission shafting under fatigue loading," 5th Annual Meeting of the National Conference on Power Transmission, Philadelphia, PA, November 8, 1978.

113. ASME Standard B106.1M, "Design of transmission shafting," American Society of Mechanical Engineers, New York, NY, 1985.

114. N. Dowling, C.A. Calhoun, and A. Arcari, "Mean stress effects in stress-life fatigue and the Walker parameter," Fatigue and Fracture of Engineering Materials and Structures 32:163-179, 2009, DOI: 10.1111/j.1460-2695.2008.01322.x.

115. B.R. Kirby and C.J. Beevers, "Slow crack growth and threshold behaviour in air and vacuum of commercial aluminum alloys," Fatigue of Engineering Materials and Structures 1:203-215, 1979.

116. A. Bondakar, F. Wang, J.J. Williams, and N. Chawla, "Environmental effects on fatigue crack growth in 7075 aluminum alloy," Metallurgical and Materials Transactions A 43(8):2799-2809, 2011, DOI:10.1007/s11661-011-0810-0.

117. H.R. Larson, "Comparison of x-ray quality and tensile properties in cast high strength steel," Transactions of the American Foundrymen's Society 67: 676-684, 1959.

118. H. Greenberg, "An engineering basis for establishing radiographic acceptance standards for porosity in steel weldments," Transactions of the ASME: Journal of Basic Engineering 87(4): 887-893, December 1965.

119. M. Kohno and M. Makioka, "Some studies on the manufacture of cast 13 chrome stainless steel Francis type runners for hydraulic turbines, " Transactions of the American Foundrymen's Society 78: 9-16, 1970.

120. R. McCallum and W. Lang, "Influence of processing route on the fatigue behavior of investment cast high strength steels," 6th World Conference on Investment Casting, Washington, D.C., October 10-13, 1984.

121. P. Heuler, C. Berger, and J. Motz, "Fatigue behavior of steel castings containing near-surface defects," Fatigue and Fracture of Engineering Materials and Structures 16:115-136, 1992.

122. Q.G. Wang, D. Apelian, and D.A. Lados, "Fatigue behavior of A356-T6 aluminum cast alloys, part I – effect of casting defects," Journal of Light Metals 1:73-84, 2001.

123. Q.G. Wang, D. Apelian, and D.A. Lados, "Fatigue behavior of A356/357 aluminum cast alloys, part II – effect of microstructural consitituents," Journal of Light Metals 1:85-97, 2001.

124. Y.X. Gao, J.Z. Yi, P.D. Lee, and T.C. Lindley, "The effect of porosity on the fatigue life of cast aluminum-silicon alloys," Fatigue and Fracture of Engineering Materials and Structures 27:559-570, 2004.

125. Y. Murakami and M. Endo, "Effect of defects, inclusions, and inhomogeneities on fatigues strength," Fatigue 16:163-182, 1994.

126. M. Rosso and M.A. Grande, "Influence of the casting process on the properties of Al based automotive components," Advanced Materials Research 23:25-32, 2007.

127. M. Romano and M. Russo, "The effect of liquid hot isostatic pressing on fatigue properties of Al based castings," Metallurgical Science and Technology 19(1):21-27, June 2001.

128. G. Ran, J.-E. Zhou, Y.-F. Wang, and S.-Q. Xi, "Microstructure and tensile properties of cast A356 aluminum alloy," Jinshu Rechuli 32(3):22-26, March 2007.

129. European Aluminum Association, The Aluminum Automotive Manual, European Aluminum Association, Brussels, Belgium, 2002.

130. C.J. Davidson, J.R. Griffiths, and A. Zanada, "Fatigue properties of squeeze, semisolid, and gravity diecast Al-S-Mg alloy," SIF2004 Structural Integrity and Fracture, Brisbane, Australia, September 26-29, 2004.

131. M. Garat and G. Laslaz, "Improved aluminum alloys for common rail diesel cylinder heads," Transactions of the American Foundry Society 115:89-96, 2007.

132. W. Jiang, Z. Fan, D. Liao, D. Liu, Z. Zhao, and X. Dong, "Investigation of microstructures and mechanical properties of A356 aluminum alloy produced by expendable pattern shell casting process with vacuum and low pressure," Materials and Design 32(2):926-934, February 2011.

133. Q.G. Wang, P.E. Jones, and M. Osborne, "Effect of iron on the microstructure and mechanical properties of an Al-7%Si-0.4%Mg casting alloy," 2003 SAE World Congress, Detroit, MI, March 3-6, 2003.

134. J.E. Hatch, ed., Aluminum: Properties and Physical Metallurgy, American Society for Metals, Metals Park, OH, 1984.

135. ASTM Standard E466, 2007, "Standard practice for conducting force-controlled constant amplitude fatigue tests of metallic materials," ASTM International, West Conshohocken, PA, 2010, DOI: 10.1520/E0466-07, http://www.astm.org.

136. M. Drouzy, S. Jacob, and M. Richard, "Interpretation of tensile results by means of a quality index," International Cast Metals Journal 5:43-50, 1980.

137. J. Campbell, Castings (2nd ed.), Butterworth-Heinemann, New York, 2003.

138. Y. Zhang, J. Xu, and T. Zhai, "Distributions of pore size and fatigue weak link strength in an A713 sand cast aluminum alloy," Materials Science and Engineering A 527:3639-3644, 2010, DOI:10.1016/j.msea.2010.03.104.

139. A. Amiri and M.N. Cavalli, "Experimental investigation of fatigue behavior of carbon fiber composites using fully reversed four point bending test," in E. Patterson, D. Backman, and G. Cloud, eds., Composite Materials and Joining Technologies for Composites, vol. 7, Springer, New York, NY, 2013, pp. 131-137.

140. E.F. Ryntz, Jr., and J.J. Bommarito, "Chill-enhanced lost foam casting process," U.S. Patent 4,520,858, June 4, 1985.

141. R.J. Simpson, "The use of chills as a means of influencing solidification in lost foam cast aluminum alloy A356," M.S. thesis, University of Western Ontario, 1997.

APPENDIX – MEAN STRESS EQUATIONS

A.1.1 GOODMAN EQUATION

Table A1. Goodman equivalent stress for 356-T6 with machined surface

R	Goodman equivalent stress (MPa)	Predicted cycles to failure	Actual cycles to failure	Error
0	86.3	276,616	202,239	37%
0	86.3	276,616	135,864	104%
0	74.3	708,419	366,497	93%
0	74.3	708,419	395,475	79%
0	74.3	708,419	283,696	150%
0	66.6	1,398,675	384,069	264%
0	66.6	1,398,675	424,776	229%
0	64.3	1,743,724	470,594	271%
0	64.3	1,743,724	378,667	360%
0	64.3	1,743,724	338,151	416%
0	61.8	2,230,884	461,822	383%
0	61.8	2,230,884	481,782	363%
0	54.0	5,210,088	796,653	554%
0	54.0	5,210,088	871,396	498%
0.09	86.6	271,898	280,705	-3%
0.09	86.6	271,898	176,107	54%
0.26	74.0	725,047	296,894	144%
0.26	74.0	725,047	343,288	111%
0.26	74.0	725,047	256,863	182%
0.37	65.6	1,545,992	391,778	295%
0.37	65.6	1,545,992	590,600	162%
0.40	63.0	1,979,810	555,037	257%
0.40	63.0	1,979,810	621,528	219%
0.40	63.0	1,979,810	674,470	194%
0.44	60.2	2,645,389	630,037	320%
0.44	60.2	2,645,389	580,154	356%
0.62	43.6	19,784,718	5,026,118	294%
0.62	43.6	19,784,718	3,381,193	485%
0.62	43.6	19,784,718	3,267,615	505%
Mean error				254%

Table A2. Goodman equivalent stress for 356-T6 with as-cast surface

R	Goodman equivalent stress (MPa)	Predicted cycles to failure	Actual cycles to failure	Error
0	70.0	332,182	226,313	47%
0	67.1	440,259	220,236	100%
0	62.1	736,456	537,623	37%
0	62.8	685,939	257,484	166%
0	59.6	971,422	298,635	225%
0	54.9	1,684,211	288,027	485%
0	54.4	1,800,830	306,850	487%
0	49.7	3,252,472	1,210,621	169%
0	47.3	4,551,582	451,319	909%
0	50.3	3,034,737	959,461	216%
0	45.4	6,022,888	1,570,361	284%
0	42.8	8,914,524	942,849	845%
0.09	71.0	303,704	425,327	-29%
0.09	70.2	327,553	101,433	223%
0.09	69.4	352,975	180,438	96%
0.26	64.5	572,961	250,808	128%
0.26	65.3	526,518	192,455	174%
0.26	60.0	931,411	365,086	155%
0.31	63.9	610,698	300,408	103%
0.31	59.2	1,018,282	386,571	163%
0.40	44.8	6,544,414	850,922	669%
0.40	50.1	3,117,663	359,927	766%
0.40	46.4	5,157,604	528,929	875%
0.44	42.0	10,055,285	2,496,331	303%
0.44	41.5	10,895,570	1,002,257	987%
Mean error				343%

Table A3. Goodman equivalent stress for 356-T7 with machined surface

R	Goodman equivalent stress (MPa)	Predicted cycles to failure	Actual cycles to failure	Error
0	66.1	546,837	559,273	-2%
0	66.1	546,837	461,839	18%
0	57.2	1,461,854	1,005,070	45%
0	57.2	1,461,854	947,782	54%
0	57.2	1,461,854	684,971	113%
0	51.5	2,990,815	1,034,306	189%
0	51.5	2,990,815	846,376	253%
0	49.8	3,741,140	1,674,938	123%
0	49.8	3,741,140	809,932	362%
0	49.8	3,741,140	873,339	328%
0	47.9	4,901,266	1,781,136	175%
0	47.9	4,901,266	1,178,452	316%
0	42.0	11,930,807	1,694,084	604%
0	42.0	11,930,807	2,286,468	422%
0	42.0	11,930,807	3,566,207	235%
0.09	65.6	570,287	414,472	38%
0.09	65.6	570,287	358,191	59%
0.26	55.5	1,789,821	880,352	103%
0.26	55.5	1,789,821	819,491	118%
0.26	55.5	1,789,821	1,417,558	26%
0.37	48.7	4,332,744	1,129,332	284%
0.37	48.7	4,332,744	1,008,951	329%
0.40	46.7	5,778,195	848,269	581%
0.40	46.7	5,778,195	1,298,928	345%
0.44	44.5	8,048,092	1,295,199	521%
0.44	44.5	8,048,092	1,567,027	414%
0.62	31.8	78,954,688	4,361,461	1710%
0.62	31.8	78,954,688	24,870,798	217%
0.62	31.8	78,954,688	5,329,296	1382%
Mean error				323%

Table A4. Goodman equivalent stress for 356-T7 with as-cast surface

R	Goodman equivalent stress (MPa)	Predicted cycles to failure	Actual cycles to failure	Error
0	65.1	316,707	152,661	107%
0	60.0	536,540	345,206	55%
0	58.1	658,094	393,661	67%
0	70.6	187,689	386,067	-51%
0	70.6	187,689	317,172	-41%
0	57.0	751,524	221,445	239%
0	58.8	610,048	362,635	68%
0	56.9	755,935	421,559	79%
0	47.9	2,290,748	262,855	771%
0	49.4	1,874,459	727,386	158%
0	46.5	2,782,611	693,066	301%
0	38.2	9,915,132	2,413,722	311%
0	38.6	9,321,207	1,914,190	387%
0.09	63.7	364,555	385,936	-6%
0.09	61.1	479,591	439,254	9%
0.09	61.1	479,591	332,457	44%
0.26	57.0	745,412	489,908	52%
0.26	53.3	1,153,551	1,042,450	11%
0.37	50.0	1,735,990	345,067	403%
0.37	51.9	1,375,870	770,908	78%
0.40	42.6	4,876,990	1,018,546	379%
0.40	43.1	4,527,025	1,180,591	283%
0.44	33.9	21,307,131	3,991,069	434%
0.44	34.7	18,467,662	10,107,592	83%
0.44	33.9	21,307,131	2,310,185	822%
Mean error				202%

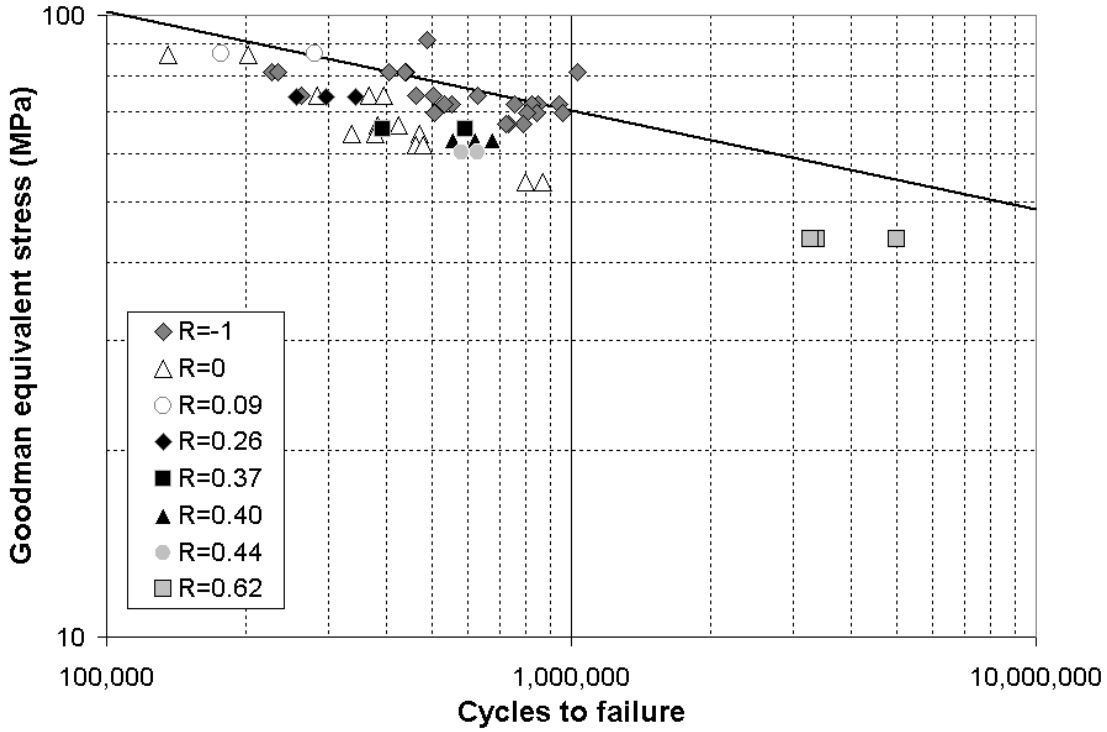

Figure A1. Goodman equivalent stress vs. cycles to failure for 356-T6 with machined surface.

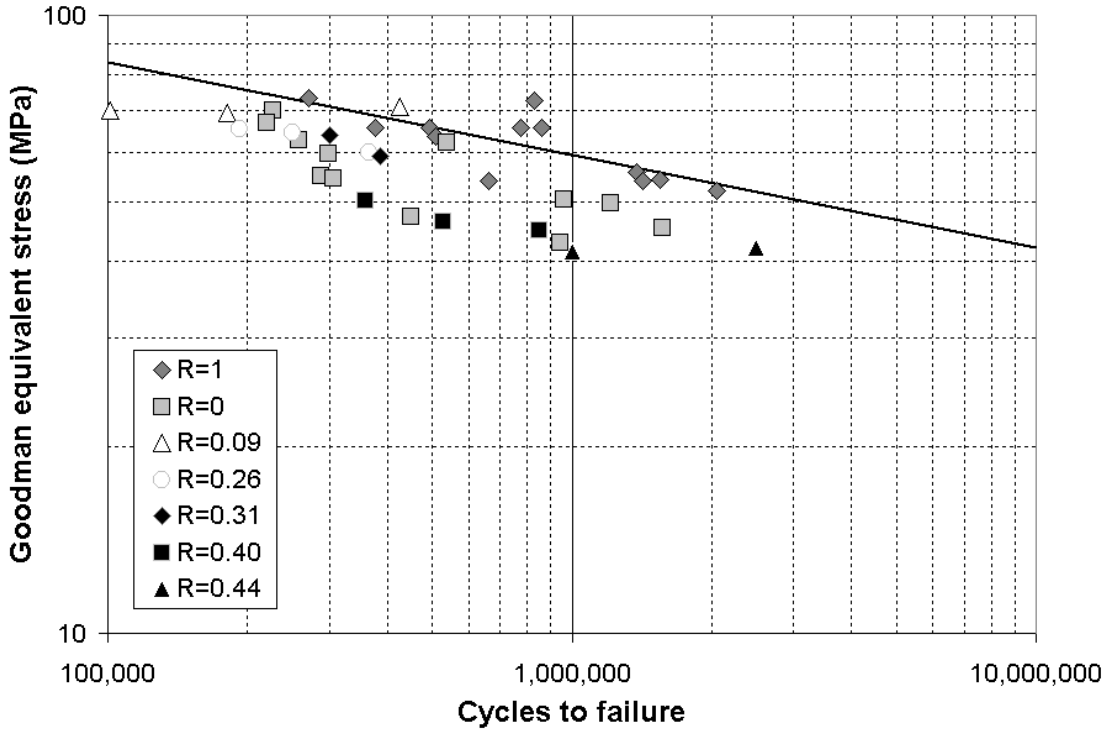

Figure A2. Goodman equivalent stress vs. cycles to failure for 356-T6 with as-cast surface.

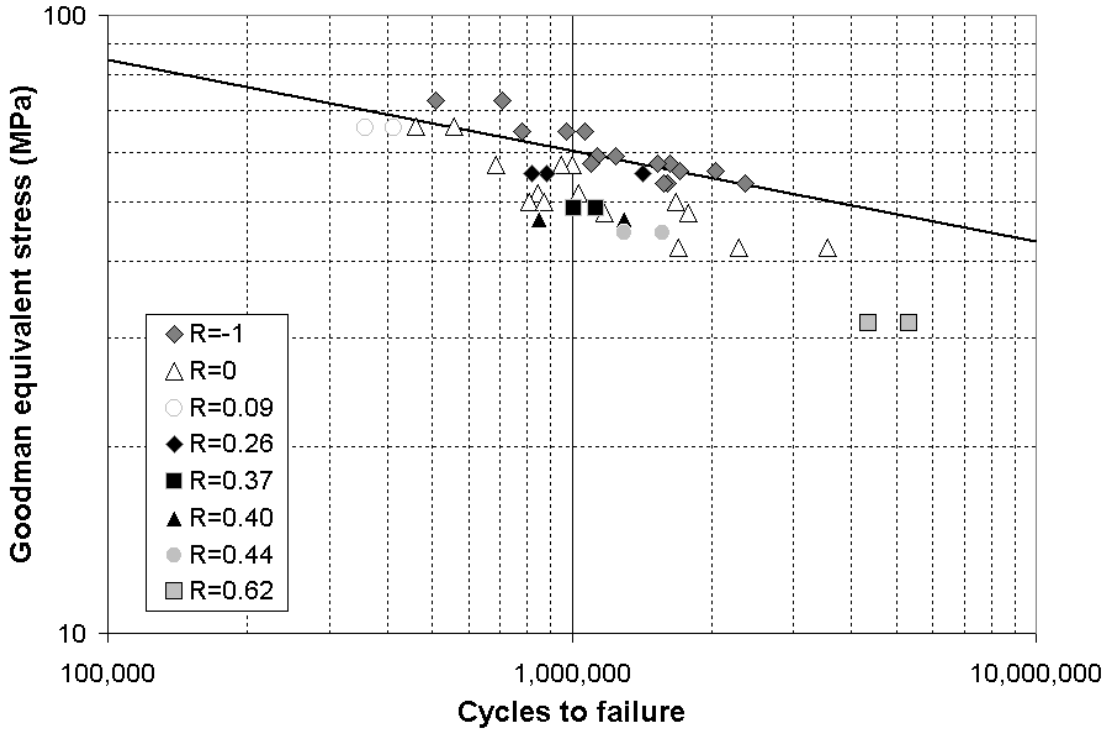

Figure A3. Goodman equivalent stress vs. cycles to failure for 356-T7 with machined surface.

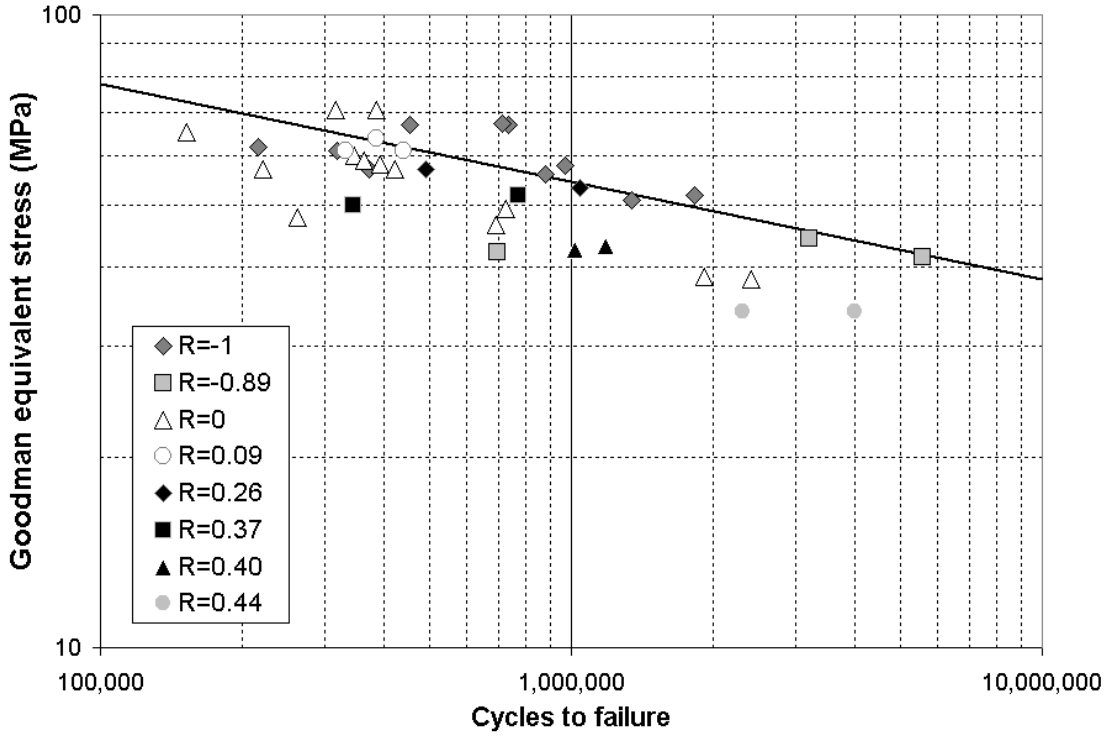

Figure A4. Goodman equivalent stress vs. cycles to failure for 356-T7 with as-cast surface.

A1.2 GERBER EQUATION

Table A5. Gerber equivalent stress for 356-T6 with machined surface

R	Gerber equivalent stress (MPa)	Predicted cycles to failure	Actual cycles to failure	Error
0	70.4	992,024	202,239	391%
0	70.4	992,024	135,864	630%
0	61.8	2,230,647	366,497	509%
0	61.8	2,230,647	395,475	464%
0	61.8	2,230,647	283,696	686%
0	56.3	4,030,345	384,069	949%
0	56.3	4,030,345	424,776	849%
0	54.6	4,887,167	470,594	939%
0	54.6	4,887,167	378,667	1191%
0	54.6	4,887,167	338,151	1345%
0	52.7	6,065,326	461,822	1213%
0	52.7	6,065,326	481,782	1159%
0	46.8	12,819,372	796,653	1509%
0	46.8	12,819,372	871,396	1371%
0.09	68.8	1,146,451	280,705	308%
0.09	68.8	1,146,451	176,107	551%
0.26	56.9	3,756,807	296,894	1165%
0.26	56.9	3,756,807	343,288	994%
0.26	56.9	3,756,807	256,863	1363%
0.37	49.4	9,054,376	391,778	2211%
0.37	49.4	9,054,376	590,600	1433%
0.40	47.3	12,004,783	555,037	2063%
0.40	47.3	12,004,783	621,528	1831%
0.40	47.3	12,004,783	674,470	1680%
0.44	44.9	16,659,566	630,037	2544%
0.44	44.9	16,659,566	580,154	2772%
0.62	31.5	152,009,673	5,026,118	2924%
0.62	31.5	152,009,673	3,381,193	4396%
0.62	31.5	152,009,673	3,267,615	4552%
Mean error				1517%

Table A6. Gerber equivalent stress for 356-T6 with as-cast surface

R	Gerber equivalent stress (MPa)	Predicted cycles to failure	Actual cycles to failure	Error
0	57.1	1,298,586	226,313	474%
0	55.1	1,653,772	220,236	651%
0	51.5	2,576,667	537,623	379%
0	52.0	2,423,242	257,484	841%
0	49.7	3,274,509	298,635	996%
0	46.3	5,283,489	288,027	1734%
0	45.9	5,601,246	306,850	1725%
0	42.4	9,398,506	1,210,621	676%
0	40.6	12,632,588	451,319	2699%
0	42.8	8,843,762	959,461	822%
0	39.1	16,177,172	1,570,361	930%
0	37.1	22,899,823	942,849	2329%
0.09	56.2	1,436,663	425,327	238%
0.09	55.7	1,531,664	101,433	1410%
0.09	55.2	1,631,846	180,438	804%
0.26	49.1	3,563,013	250,808	1321%
0.26	49.6	3,319,987	192,455	1625%
0.26	46.2	5,351,602	365,086	1366%
0.31	47.7	4,282,317	300,408	1326%
0.31	44.8	6,558,505	386,571	1597%
0.40	34.4	38,500,165	850,922	4425%
0.40	37.7	20,715,606	359,927	5656%
0.40	35.4	31,541,955	528,929	5863%
0.44	32.0	61,306,465	2,496,331	2356%
0.44	31.7	65,565,004	1,002,257	6442%
Mean error				1947%

Table A7. Gerber equivalent stress for 356-T7 with machined surface

R	Gerber equivalent stress (MPa)	Predicted cycles to failure	Actual cycles to failure	Error
0	55.5	1,795,984	559,273	221%
0	55.5	1,795,984	461,839	289%
0	48.9	4,245,625	1,005,070	322%
0	48.9	4,245,625	947,782	348%
0	48.9	4,245,625	684,971	520%
0	44.5	7,988,503	1,034,306	672%
0	44.5	7,988,503	846,376	844%
0	43.3	9,744,237	1,674,938	482%
0	43.3	9,744,237	809,932	1103%
0	43.3	9,744,237	873,339	1016%
0	41.8	12,391,934	1,781,136	596%
0	41.8	12,391,934	1,178,452	952%
0	37.2	27,485,775	1,694,084	1522%
0	37.2	27,485,775	2,286,468	1102%
0	37.2	27,485,775	3,566,207	671%
0.09	53.9	2,182,892	414,472	427%
0.09	53.9	2,182,892	358,191	509%
0.26	44.3	8,324,724	880,352	846%
0.26	44.3	8,324,724	819,491	916%
0.26	44.3	8,324,724	1,417,558	487%
0.37	38.2	22,664,861	1,129,332	1907%
0.37	38.2	22,664,861	1,008,951	2146%
0.40	36.5	31,252,483	848,269	3584%
0.40	36.5	31,252,483	1,298,928	2306%
0.44	34.5	45,119,917	1,295,199	3384%
0.44	34.5	45,119,917	1,567,027	2779%
0.62	24.0	535,011,449	4,361,461	12167%
0.62	24.0	535,011,449	24,870,798	2051%
0.62	24.0	535,011,449	5,329,296	9939%
Mean error				1866%

Table A8. Gerber equivalent stress for 356-T7 with as-cast surface

R	Gerber equivalent stress (MPa)	Predicted cycles to failure	Actual cycles to failure	Error
0	53.5	1,124,333	152,661	636%
0	49.9	1,771,904	345,206	413%
0	48.5	2,114,808	393,661	437%
0	57.4	717,694	386,067	86%
0	57.4	717,694	317,172	126%
0	47.7	2,373,085	221,445	972%
0	49.0	1,980,286	362,635	446%
0	47.6	2,385,178	421,559	466%
0	41.0	6,286,568	262,855	2292%
0	42.1	5,270,839	727,386	625%
0	39.9	7,461,190	693,066	977%
0	33.5	23,061,795	2,413,722	855%
0	33.8	21,822,534	1,914,190	1040%
0.09	51.2	1,498,823	385,936	288%
0.09	49.4	1,893,648	439,254	331%
0.09	49.4	1,893,648	332,457	470%
0.26	44.1	3,890,054	489,908	694%
0.26	41.7	5,617,301	1,042,450	439%
0.37	38.0	10,231,191	345,067	2865%
0.37	39.2	8,425,704	770,908	993%
0.40	32.9	26,140,430	1,018,546	2466%
0.40	33.2	24,557,740	1,180,591	1980%
0.44	26.7	99,701,681	3,991,069	2398%
0.44	27.2	88,361,815	10,107,592	774%
0.44	26.7	99,701,681	2,310,185	4216%
Mean error				1091%

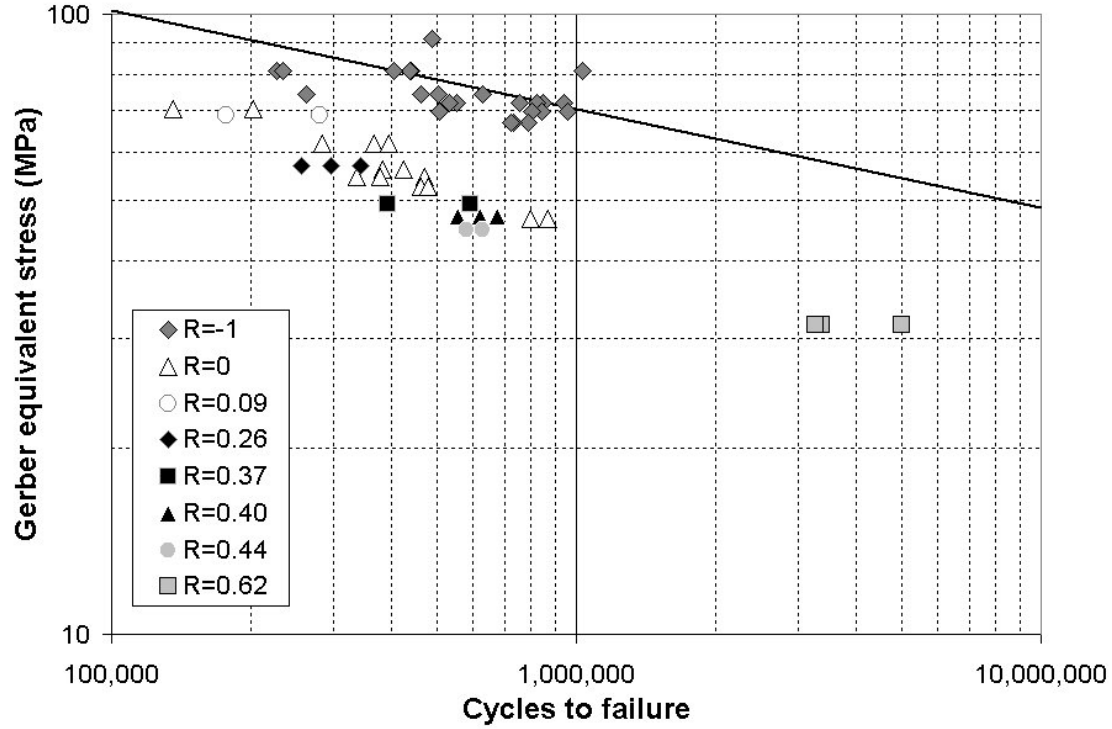

Figure A5. Gerber equivalent stress vs. cycles to failure for 356-T6 with machined surface.

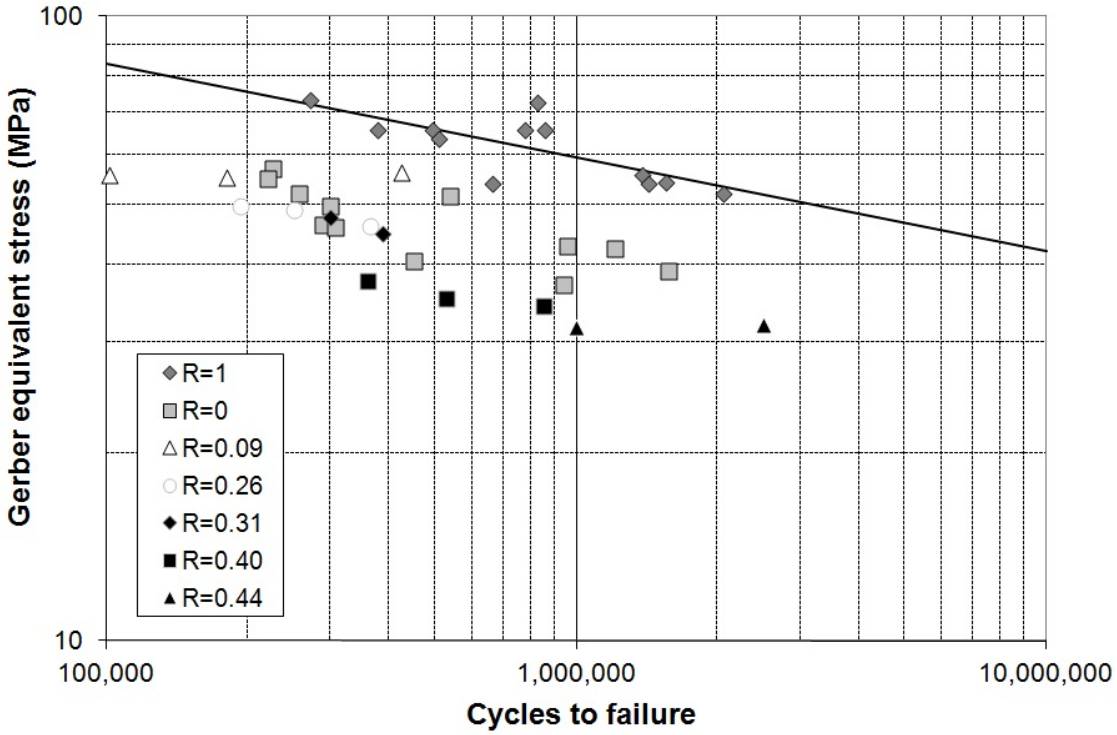

Figure A6. Gerber equivalent stress vs. cycles to failure for 356-T6 with as-cast surface.

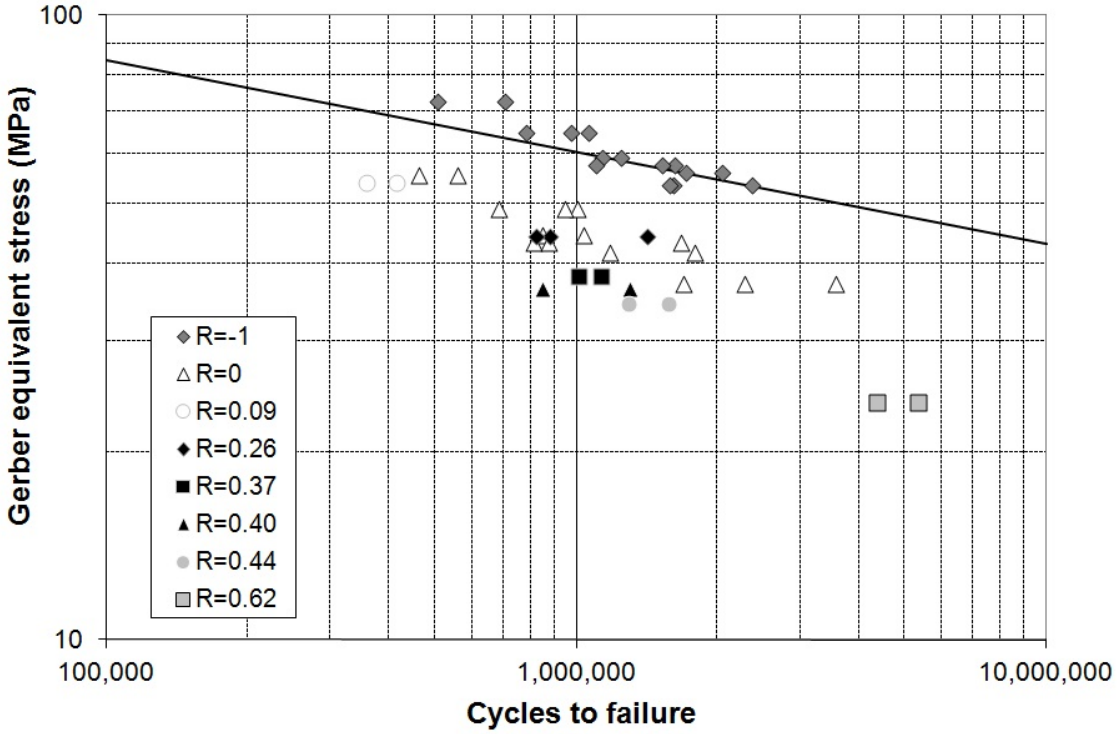

Figure A7. Gerber equivalent stress vs. cycles to failure for 356-T7 with machined surface.

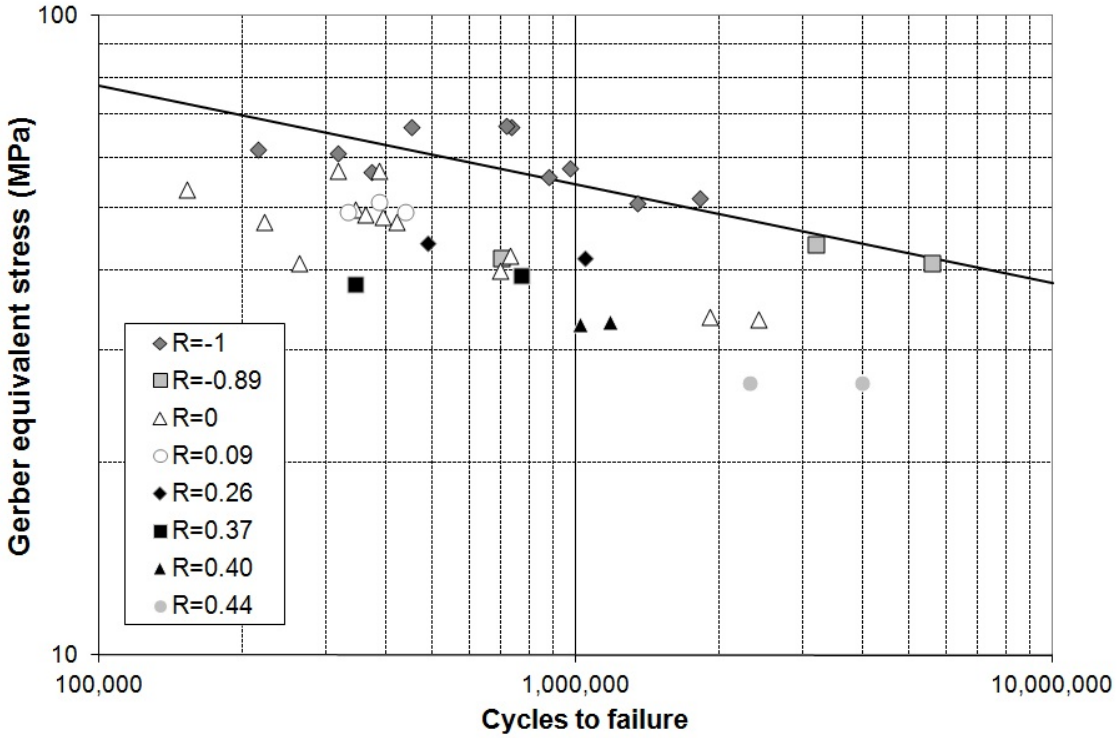

Figure A8. Gerber equivalent stress vs. cycles to failure for 356-T7 with as-cast surface.

A1.3 SMITH-WATSON-TOPPER EQUATION

Table A9. SWT equivalent stress for 356-T6 with machined surface

R	SWT equivalent stress (MPa)	Predicted cycles to failure	Actual cycles to failure	Error
0	94.5	157,626	202,239	-22%
0	94.5	157,626	135,864	16%
0	83.9	330,219	366,497	-10%
0	83.9	330,219	395,475	-17%
0	83.9	330,219	283,696	16%
0	76.9	571,905	384,069	49%
0	76.9	571,905	424,776	35%
0	74.7	685,001	470,594	46%
0	74.7	685,001	378,667	81%
0	74.7	685,001	338,151	103%
0	72.3	839,155	461,822	82%
0	72.3	839,155	481,782	74%
0	64.6	1,705,452	796,653	114%
0	64.6	1,705,452	871,396	96%
0.09	95.0	152,504	280,705	-46%
0.09	95.0	152,504	176,107	-13%
0.26	85.3	299,066	296,894	1%
0.26	85.3	299,066	343,288	-13%
0.26	85.3	299,066	256,863	16%
0.37	78.8	491,008	391,778	25%
0.37	78.8	491,008	590,600	-17%
0.40	76.8	575,131	555,037	4%
0.40	76.8	575,131	621,528	-7%
0.40	76.8	575,131	674,470	-15%
0.44	74.6	690,733	630,037	10%
0.44	74.6	690,733	580,154	19%
0.62	61.4	2,337,605	5,026,118	-53%
0.62	61.4	2,337,605	3,381,193	-31%
0.62	61.4	2,337,605	3,267,615	-28%
Mean error				18%

Table A10. SWT equivalent stress for 356-T6 with as-cast surface

R	SWT equivalent stress (MPa)	Predicted cycles to failure	Actual cycles to failure	Error
0	76.6	182,597	226,313	-19%
0	74.1	227,277	220,236	3%
0	69.7	340,764	537,623	-37%
0	70.3	322,098	257,484	25%
0	67.5	424,915	298,635	42%
0	63.1	662,407	288,027	130%
0	62.6	699,506	306,850	128%
0	58.2	1,136,700	1,210,621	-6%
0	55.8	1,503,030	451,319	233%
0	58.7	1,073,397	959,461	12%
0	53.9	1,900,465	1,570,361	21%
0	51.3	2,646,364	942,849	181%
0.09	77.6	167,170	425,327	-61%
0.09	77.0	176,775	101,433	74%
0.09	76.3	186,844	180,438	4%
0.26	72.7	259,083	250,808	3%
0.26	73.3	244,533	192,455	27%
0.26	69.1	362,783	365,086	-1%
0.31	72.2	271,513	300,408	-10%
0.31	68.6	382,383	386,571	-1%
0.40	56.9	1,326,422	850,922	56%
0.40	61.4	798,705	359,927	122%
0.40	58.3	1,124,848	528,929	113%
0.44	54.7	1,731,774	2,496,331	-31%
0.44	54.2	1,830,420	1,002,257	83%
Mean error				44%

Table A11. SWT equivalent stress for 356-T7 with machined surface

R	SWT equivalent stress (MPa)	Predicted cycles to failure	Actual cycles to failure	Error
0	75.6	218,481	559,273	-60.93%
0	75.6	218,481	461,839	-52.69%
0	67.1	489,295	1,005,070	-51.32%
0	67.1	489,295	947,782	-48.37%
0	67.1	489,295	684,971	-28.57%
0	61.5	891,237	1,034,306	-13.83%
0	61.5	891,237	846,376	5.30%
0	59.8	1,077,264	1,674,938	-35.68%
0	59.8	1,077,264	809,932	33.01%
0	59.8	1,077,264	873,339	23.35%
0	57.8	1,355,845	1,781,136	-23.88%
0	57.8	1,355,845	1,178,452	15.05%
0	51.6	2,918,927	1,694,084	72.30%
0	51.6	2,918,927	2,286,468	27.66%
0	51.6	2,918,927	3,566,207	-18.15%
0.09	76.0	211,344	414,472	-49.01%
0.09	76.0	211,344	358,191	-41.00%
0.26	68.2	438,282	880,352	-50.22%
0.26	68.2	438,282	819,491	-46.52%
0.26	68.2	438,282	1,417,558	-69.08%
0.37	63.0	754,352	1,129,332	-33.20%
0.37	63.0	754,352	1,008,951	-25.23%
0.40	61.4	897,288	848,269	5.78%
0.40	61.4	897,288	1,298,928	-30.92%
0.44	59.7	1,093,652	1,295,199	-15.56%
0.44	59.7	1,093,652	1,567,027	-30.21%
0.62	49.1	4,094,925	4,361,461	-6.11%
0.62	49.1	4,094,925	24,870,798	-83.54%
0.62	49.1	4,094,925	5,329,296	-23.16%
Mean error				-23%

Table A12. SWT equivalent stress for 356-T7 with as-cast surface

R	SWT equivalent stress (MPa)	Predicted cycles to failure	Actual cycles to failure	Error
0	72.1	164,045	152,661	7%
0	67.6	248,767	345,206	-28%
0	65.9	292,863	393,661	-26%
0	76.8	109,304	386,067	-72%
0	76.8	109,304	317,172	-66%
0	64.8	325,820	221,445	47%
0	66.5	275,614	362,635	-24%
0	64.8	327,358	421,559	-22%
0	56.3	810,803	262,855	208%
0	57.8	686,688	727,386	-6%
0	54.9	953,366	693,066	38%
0	46.5	2,799,740	2,413,722	16%
0	46.8	2,654,952	1,914,190	39%
0.09	71.3	176,464	385,936	-54%
0.09	69.0	217,294	439,254	-51%
0.09	69.0	217,294	332,457	-35%
0.26	66.3	281,042	489,908	-43%
0.26	63.2	384,037	1,042,450	-63%
0.37	60.9	486,588	345,067	41%
0.37	62.4	415,470	770,908	-46%
0.40	54.7	978,213	1,018,546	-4%
0.40	55.1	928,423	1,180,591	-21%
0.44	46.7	2,692,301	3,991,069	-33%
0.44	47.5	2,426,223	10,107,592	-76%
0.44	46.7	2,692,301	2,310,185	17%
Mean error				-10%

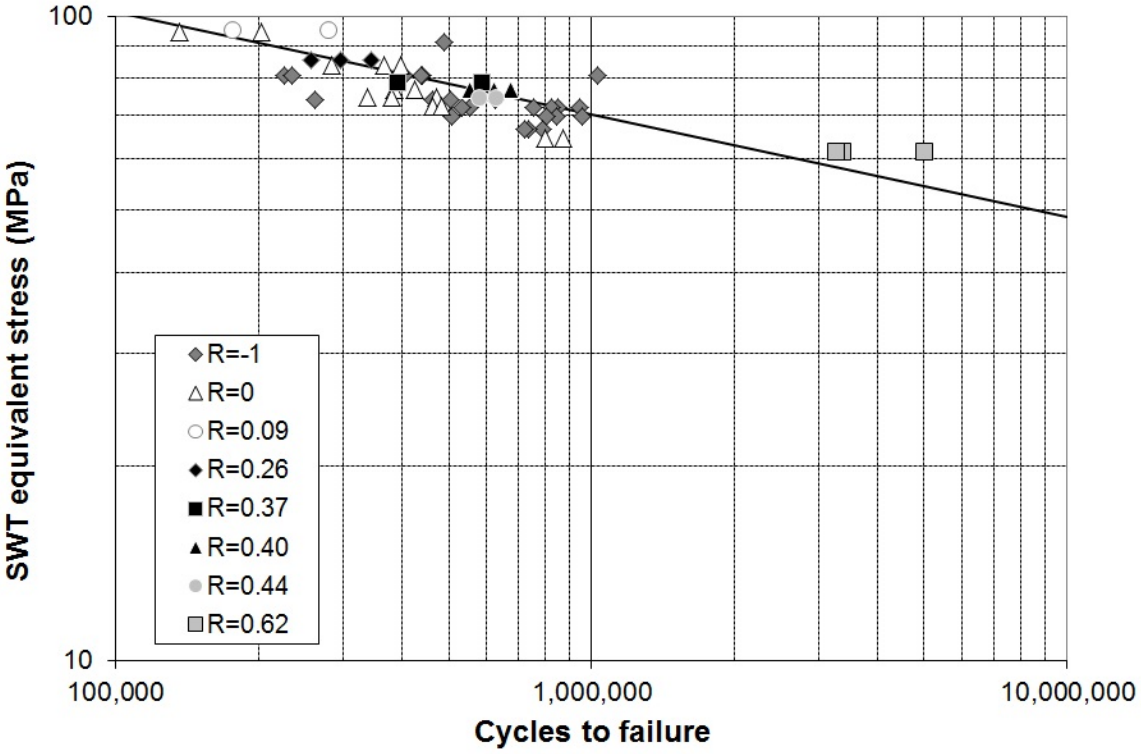

Figure A9. Smith-Watson-Topper equivalent stress vs. cycles to failure for 356-T6 with machined surface.

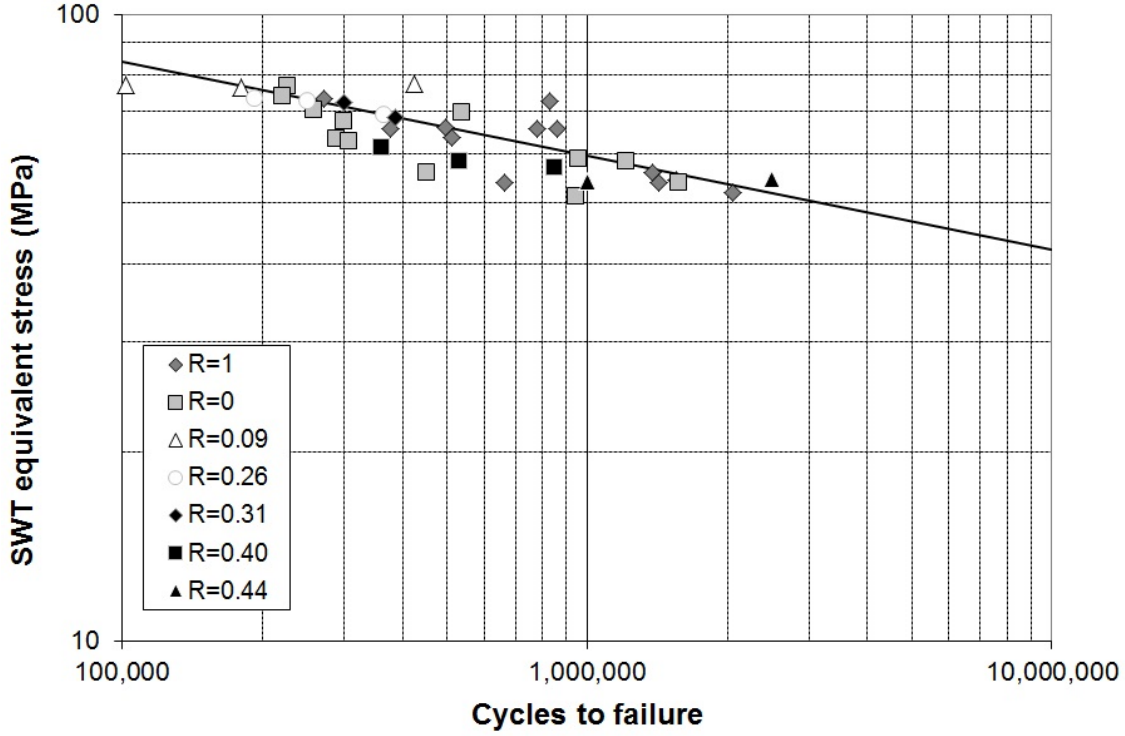

Figure A10. Smith-Watson-Topper equivalent stress vs. cycles to failure for 356-T6 with as-cast surface.

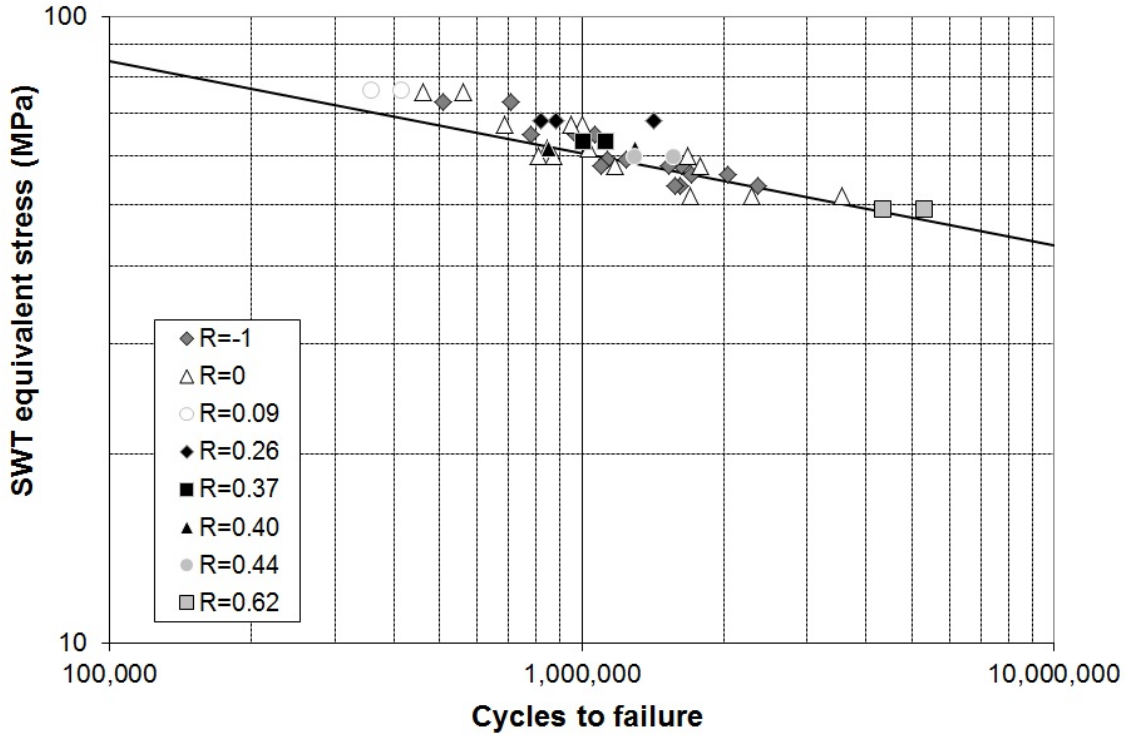

Figure A11. Smith-Watson-Topper equivalent stress vs. cycles to failure for 356-T7 with machined surface.

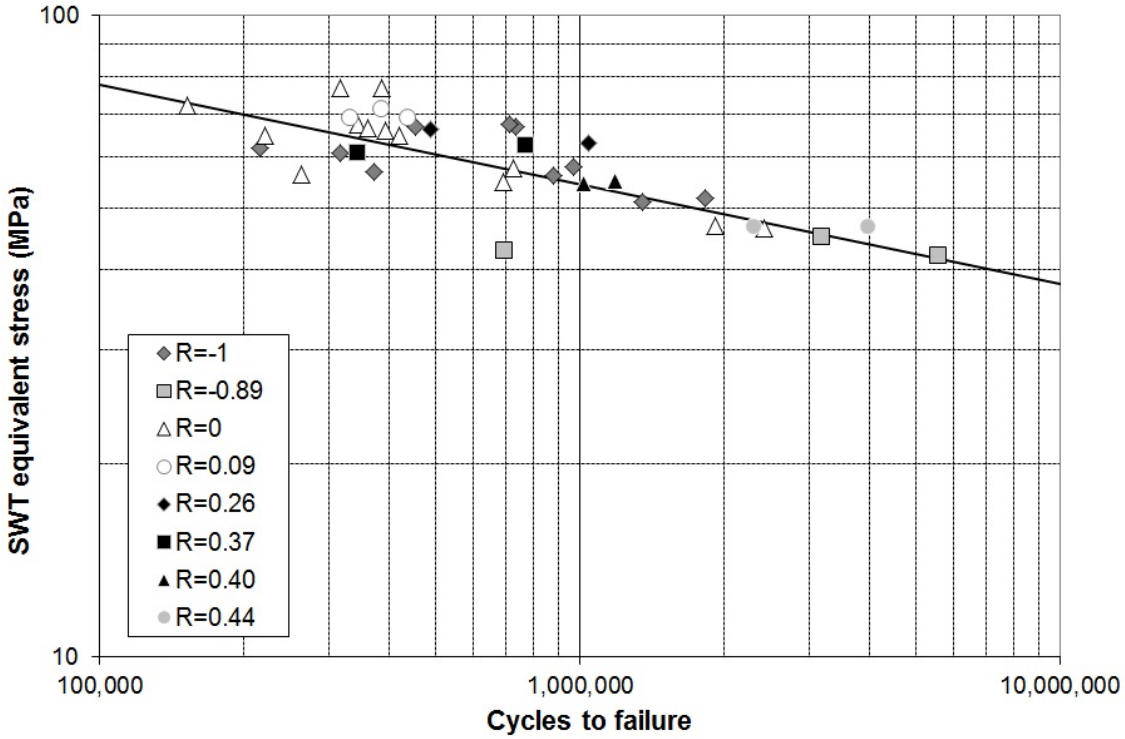

Figure A12. Smith-Watson-Topper equivalent stress vs. cycles to failure for 356-T7 with as-cast surface.

A1.4 STULEN EQUATION

Table A13. Stulen equivalent stress for 356-T6 with machined surface

R	Stulen equivalent stress (MPa)	Predicted cycles to failure	Actual cycles to failure	Error	Absolute error
0	94.6	155,696	202,239	-23%	15%
0	94.6	155,696	135,864	15%	11%
0	84.1	326,177	366,497	-11%	18%
0	84.1	326,177	395,475	-18%	15%
0	84.1	326,177	283,696	15%	47%
0	77.0	564,904	384,069	47%	33%
0	77.0	564,904	424,776	33%	44%
0	74.8	676,615	470,594	44%	79%
0	74.8	676,615	378,667	79%	100%
0	74.8	676,615	338,151	100%	79%
0	72.4	828,881	461,822	79%	72%
0	72.4	828,881	481,782	72%	111%
0	64.7	1,684,574	796,653	111%	93%
0	64.7	1,684,574	871,396	93%	49%
0.09	96.0	142,443	280,705	-49%	19%
0.09	96.0	142,443	176,107	-19%	22%
0.26	88.7	232,795	296,894	-22%	32%
0.26	88.7	232,795	343,288	-32%	9%
0.26	88.7	232,795	256,863	-9%	18%
0.37	84.3	320,537	391,778	-18%	46%
0.37	84.3	320,537	590,600	-46%	36%
0.40	83.1	352,449	555,037	-36%	43%
0.40	83.1	352,449	621,528	-43%	48%
0.40	83.1	352,449	674,470	-48%	38%
0.44	81.7	391,772	630,037	-38%	32%
0.44	81.7	391,772	580,154	-32%	86%
0.62	74.2	712,984	5,026,118	-86%	79%
0.62	74.2	712,984	3,381,193	-79%	78%
0.62	74.2	712,984	3,267,615	-78%	15%
Mean error				0.03%	31%

Table A14. Stulen equivalent stress for 356-T6 with as-cast surface

R	Stulen equivalent stress (MPa)	Predicted cycles to failure	Actual cycles to failure	Error	Absolute error
0	78.7	151,725	226,313	-33%	33%
0	76.2	188,851	220,236	-14%	14%
0	71.7	283,150	537,623	-47%	47%
0	72.3	267,640	257,484	4%	4%
0	69.4	353,074	298,635	18%	18%
0	64.9	550,412	288,027	91%	91%
0	64.4	581,239	306,850	89%	89%
0	59.9	944,516	1,210,621	-22%	22%
0	57.4	1,248,909	451,319	177%	177%
0	60.4	891,915	959,461	-7%	7%
0	55.4	1,579,150	1,570,361	1%	1%
0	52.8	2,198,937	942,849	133%	133%
0.09	80.8	127,631	425,327	-70%	70%
0.09	80.1	134,964	101,433	33%	33%
0.09	79.5	142,652	180,438	-21%	21%
0.26	78.4	156,462	250,808	-38%	38%
0.26	79.1	147,676	192,455	-23%	23%
0.26	74.5	219,087	365,086	-40%	40%
0.31	79.0	148,143	300,408	-51%	51%
0.31	75.1	208,636	386,571	-46%	46%
0.40	64.2	594,630	850,922	-30%	30%
0.40	69.2	358,056	359,927	-1%	1%
0.40	65.8	504,265	528,929	-5%	5%
0.44	62.7	694,670	2,496,331	-72%	72%
0.44	62.2	734,240	1,002,257	-27%	27%
Mean error				0.00%	44%

Table A15. Stulen equivalent stress for 356-T7 with machined surface

R	Stulen equivalent stress (MPa)	Predicted cycles to failure	Actual cycles to failure	Error	Absolute error
0	71.7	313,740	559,273	-44%	44%
0	71.7	313,740	461,839	-32%	32%
0	63.7	702,630	1,005,070	-30%	30%
0	63.7	702,630	947,782	-26%	26%
0	63.7	702,630	684,971	3%	3%
0	58.3	1,279,821	1,034,306	24%	24%
0	58.3	1,279,821	846,376	51%	51%
0	56.7	1,546,957	1,674,938	-8%	8%
0	56.7	1,546,957	809,932	91%	91%
0	56.7	1,546,957	873,339	77%	77%
0	54.8	1,947,000	1,781,136	9%	9%
0	54.8	1,947,000	1,178,452	65%	65%
0	49.0	4,191,594	1,694,084	147%	147%
0	49.0	4,191,594	2,286,468	83%	83%
0	49.0	4,191,594	3,566,207	18%	18%
0.09	72.1	299,817	414,472	-28%	28%
0.09	72.1	299,817	358,191	-16%	16%
0.26	65.6	571,648	880,352	-35%	35%
0.26	65.6	571,648	819,491	-30%	30%
0.26	65.6	571,648	1,417,558	-60%	60%
0.37	61.6	879,688	1,129,332	-22%	22%
0.37	61.6	879,688	1,008,951	-13%	13%
0.40	60.4	1,000,898	848,269	18%	18%
0.40	60.4	1,000,898	1,298,928	-23%	23%
0.44	59.2	1,153,863	1,295,199	-11%	11%
0.44	59.2	1,153,863	1,567,027	-26%	26%
0.62	52.5	2,617,657	4,361,461	-40%	40%
0.62	52.5	2,617,657	24,870,798	-89%	89%
0.62	52.5	2,617,657	5,329,296	-51%	51%
Mean error				0.09%	40%

Table A16. Stulen equivalent stress for 356-T7 with as-cast surface

R	Stulen equivalent stress (MPa)	Predicted cycles to failure	Actual cycles to failure	Error	Absolute error
0	70.0	199,467	152,661	31%	31%
0	65.6	302,484	345,206	-12%	12%
0	64.0	356,101	393,661	-10%	10%
0	74.5	132,907	386,067	-66%	66%
0	74.5	132,907	317,172	-58%	58%
0	62.9	396,174	221,445	79%	79%
0	64.6	335,128	362,635	-8%	8%
0	62.9	398,045	421,559	-6%	6%
0	54.6	985,880	262,855	275%	275%
0	56.0	834,965	727,386	15%	15%
0	53.3	1,159,227	693,066	67%	67%
0	45.1	3,404,290	2,413,722	41%	41%
0	45.4	3,228,238	1,914,190	69%	69%
0.09	69.5	207,681	385,936	-46%	46%
0.09	67.3	255,735	439,254	-42%	42%
0.09	67.3	255,735	332,457	-23%	23%
0.26	65.9	293,347	489,908	-40%	40%
0.26	62.8	400,852	1,042,450	-62%	62%
0.37	61.9	441,233	345,067	28%	28%
0.37	63.4	376,744	770,908	-51%	51%
0.40	55.9	844,371	1,018,546	-17%	17%
0.40	56.4	801,394	1,180,591	-32%	32%
0.44	48.4	2,156,282	3,991,069	-46%	46%
0.44	49.2	1,943,178	10,107,592	-81%	81%
0.44	48.4	2,156,282	2,310,185	-7%	7%
Mean error				-0.04%	48%

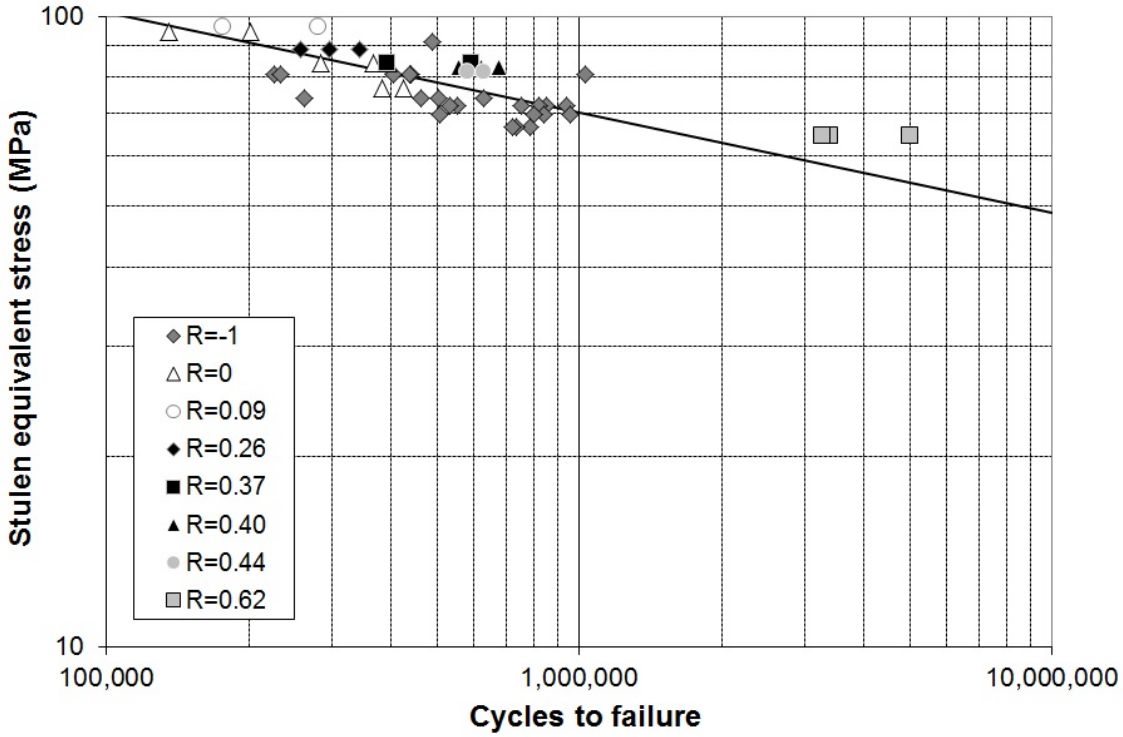

Figure A13. Stulen equivalent stress vs. cycles to failure for 356-T6 with machined surface.

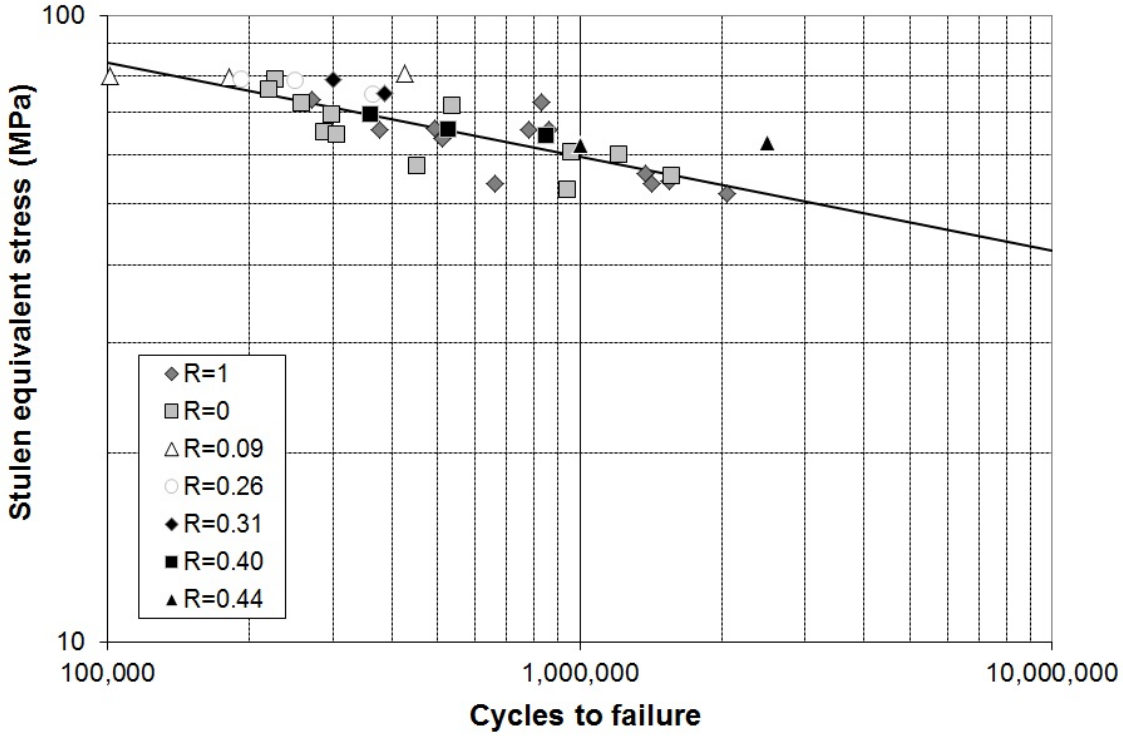

Figure A14. Stulen equivalent stress vs. cycles to failure for 356-T6 with as-cast surface.

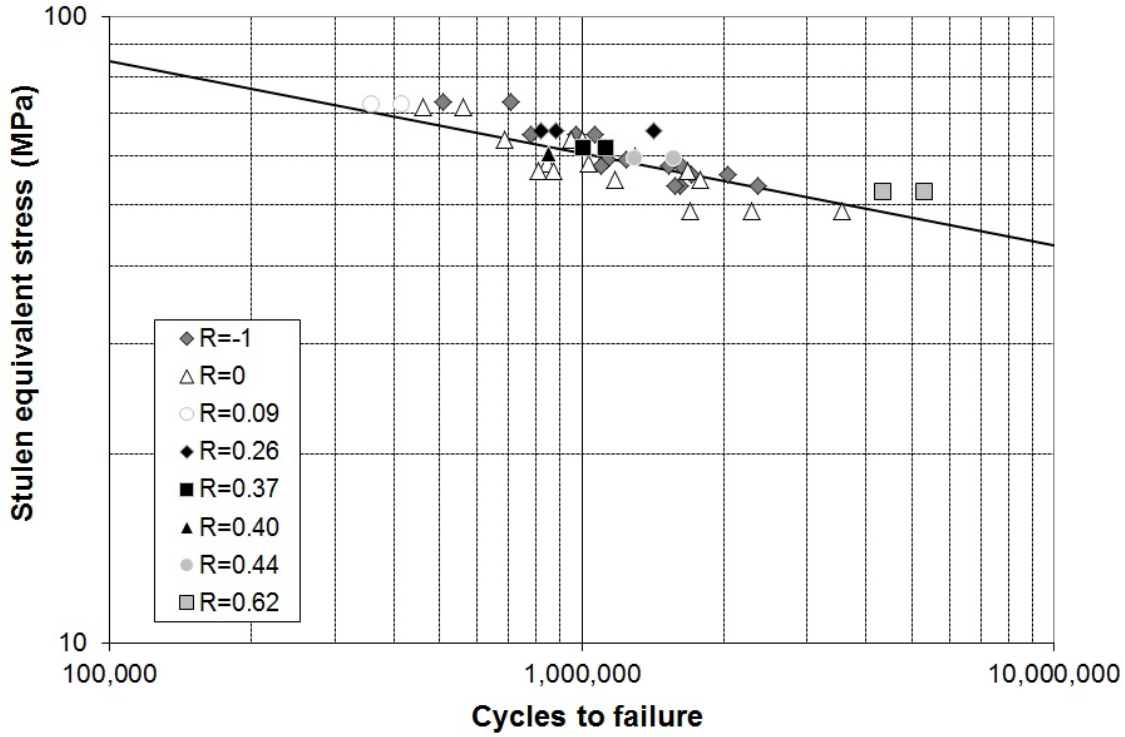

Figure A15. Stulen equivalent stress vs. cycles to failure for 356-T7 with machined surface.

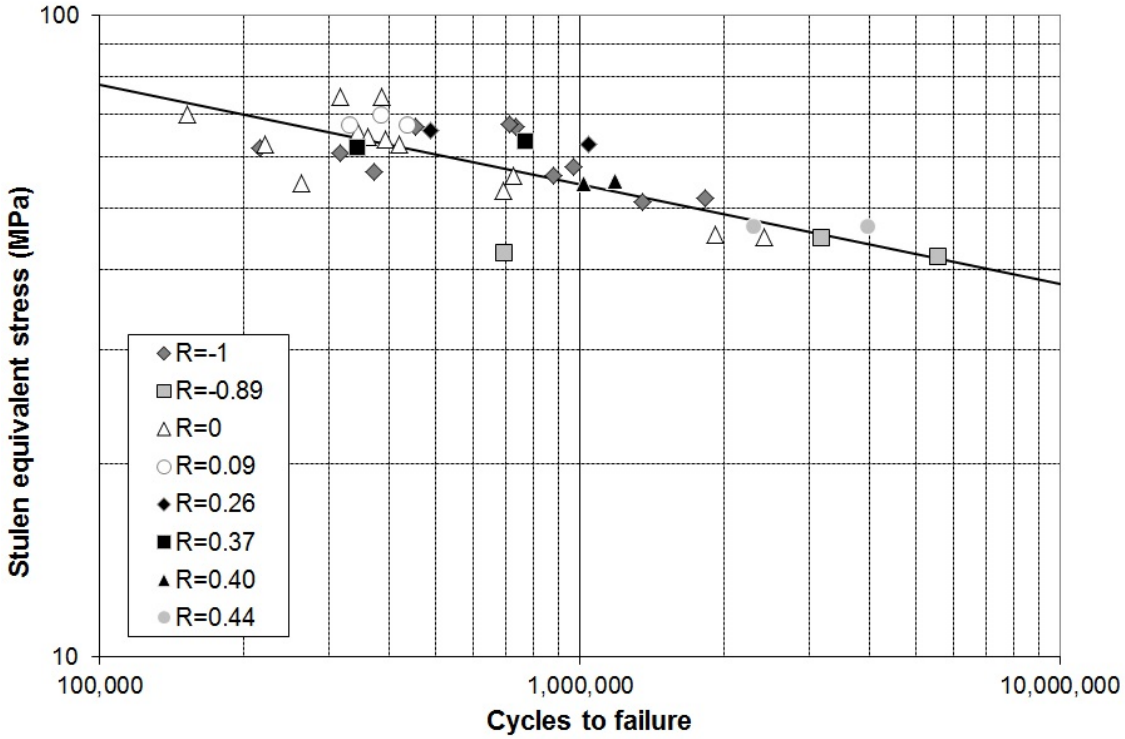

Figure A16. Stulen equivalent stress vs. cycles to failure for 356-T7 with as-cast surface.

A1.5 TOPPER-SANDOR EQUATION

Table A17. Topper-Sandor equivalent stress for 356-T6 with machined surface

R	Topper-Sandor equivalent stress (MPa)	Predicted cycles to failure	Actual cycles to failure	Error	Absolute error
0	94.8	154,280	202,239	-24%	24%
0	94.8	154,280	135,864	14%	14%
0	84.8	308,803	366,497	-16%	16%
0	84.8	308,803	395,475	-22%	22%
0	84.8	308,803	283,696	9%	9%
0	78.1	516,743	384,069	35%	35%
0	78.1	516,743	424,776	22%	22%
0	76.0	611,922	470,594	30%	30%
0	76.0	611,922	378,667	62%	62%
0	76.0	611,922	338,151	81%	81%
0	73.8	740,046	461,822	60%	60%
0	73.8	740,046	481,782	54%	54%
0	66.3	1,437,233	796,653	80%	80%
0	66.3	1,437,233	871,396	65%	65%
0.09	95.3	149,200	280,705	-47%	47%
0.09	95.3	149,200	176,107	-15%	15%
0.26	86.8	267,261	296,894	-10%	10%
0.26	86.8	267,261	343,288	-22%	22%
0.26	86.8	267,261	256,863	4%	4%
0.37	81.6	394,233	391,778	1%	1%
0.37	81.6	394,233	590,600	-33%	33%
0.40	80.1	443,054	555,037	-20%	20%
0.40	80.1	443,054	621,528	-29%	29%
0.40	80.1	443,054	674,470	-34%	34%
0.44	78.4	505,008	630,037	-20%	20%
0.44	78.4	505,008	580,154	-13%	13%
0.62	69.5	1,076,173	5,026,118	-79%	79%
0.62	69.5	1,076,173	3,381,193	-68%	68%
0.62	69.5	1,076,173	3,267,615	-67%	67%
Mean error				-0.13%	36%

Table A18. Topper-Sandor equivalent stress for 356-T6 with as-cast surface

R	Topper-Sandor equivalent stress (MPa)	Predicted cycles to failure	Actual cycles to failure	Error	Absolute error
0	78.8	150,692	226,313	-33%	33%
0	76.4	185,046	220,236	-16%	16%
0	72.2	270,546	537,623	-50%	50%
0	72.8	256,627	257,484	0%	0%
0	70.0	332,730	298,635	11%	11%
0	65.8	504,392	288,027	75%	75%
0	65.3	530,807	306,850	73%	73%
0	61.0	836,316	1,210,621	-31%	31%
0	58.6	1,086,202	451,319	141%	141%
0	61.5	792,639	959,461	-17%	17%
0	56.7	1,352,803	1,570,361	-14%	14%
0	54.2	1,843,752	942,849	96%	96%
0.09	80.1	135,424	425,327	-68%	68%
0.09	79.5	142,660	101,433	41%	41%
0.09	78.9	150,216	180,438	-17%	17%
0.26	76.3	186,591	250,808	-26%	26%
0.26	76.9	176,958	192,455	-8%	8%
0.26	72.9	254,062	365,086	-30%	30%
0.31	76.3	186,665	300,408	-38%	38%
0.31	72.8	255,069	386,571	-34%	34%
0.40	62.4	715,501	850,922	-16%	16%
0.40	66.8	452,847	359,927	26%	26%
0.40	63.8	616,696	528,929	17%	17%
0.44	60.8	856,642	2,496,331	-66%	66%
0.44	60.3	900,278	1,002,257	-10%	10%
Mean error				0.18%	38%

Table A19. Topper-Sandor equivalent stress for 356-T7 with machined surface

R	Topper-Sandor equivalent stress (MPa)	Predicted cycles to failure	Actual cycles to failure	Error	Absolute error
0	72.0	304,290	559,273	-46%	46%
0	72.0	304,290	461,839	-34%	34%
0	64.5	644,415	1,005,070	-36%	36%
0	64.5	644,415	947,782	-32%	32%
0	64.5	644,415	684,971	-6%	6%
0	59.4	1,125,027	1,034,306	9%	9%
0	59.4	1,125,027	846,376	33%	33%
0	57.9	1,341,532	1,674,938	-20%	20%
0	57.9	1,341,532	809,932	66%	66%
0	57.9	1,341,532	873,339	54%	54%
0	56.1	1,660,727	1,781,136	-7%	7%
0	56.1	1,660,727	1,178,452	41%	41%
0	50.5	3,380,627	1,694,084	100%	100%
0	50.5	3,380,627	2,286,468	48%	48%
0	50.5	3,380,627	3,566,207	-5%	5%
0.09	71.8	310,381	414,472	-25%	25%
0.09	71.8	310,381	358,191	-13%	13%
0.26	64.3	659,037	880,352	-25%	25%
0.26	64.3	659,037	819,491	-20%	20%
0.26	64.3	659,037	1,417,558	-54%	54%
0.37	59.6	1,102,973	1,129,332	-2%	2%
0.37	59.6	1,102,973	1,008,951	9%	9%
0.40	58.2	1,289,374	848,269	52%	52%
0.40	58.2	1,289,374	1,298,928	-1%	1%
0.44	56.8	1,533,022	1,295,199	18%	18%
0.44	56.8	1,533,022	1,567,027	-2%	2%
0.62	48.9	4,248,953	4,361,461	-3%	3%
0.62	48.9	4,248,953	24,870,798	-83%	83%
0.62	48.9	4,248,953	5,329,296	-20%	20%
Mean error				-0.14%	30%

Table A20. Topper-Sandor equivalent stress for 356-T7 with as-cast surface

R	Topper-Sandor equivalent stress (MPa)	Predicted cycles to failure	Actual cycles to failure	Error	Absolute error
0	70.0	198,767	152,661	30%	30%
0	65.9	292,939	345,206	-15%	15%
0	64.4	340,995	393,661	-13%	13%
0	74.2	136,134	386,067	-65%	65%
0	74.2	136,134	317,172	-57%	57%
0	63.4	376,572	221,445	70%	70%
0	64.9	322,263	362,635	-11%	11%
0	63.4	378,227	421,559	-10%	10%
0	55.6	878,858	262,855	234%	234%
0	56.9	753,172	727,386	4%	4%
0	54.3	1,021,497	693,066	47%	47%
0	46.5	2,773,884	2,413,722	15%	15%
0	46.9	2,640,750	1,914,190	38%	38%
0.09	68.9	219,645	385,936	-43%	43%
0.09	66.9	266,220	439,254	-39%	39%
0.09	66.9	266,220	332,457	-20%	20%
0.26	64.1	350,108	489,908	-29%	29%
0.26	61.4	464,683	1,042,450	-55%	55%
0.37	59.4	572,623	345,067	66%	66%
0.37	60.7	497,216	770,908	-36%	36%
0.40	54.0	1,058,418	1,018,546	4%	4%
0.40	54.4	1,010,426	1,180,591	-14%	14%
0.44	47.2	2,542,779	3,991,069	-36%	36%
0.44	47.8	2,320,059	10,107,592	-77%	77%
0.44	47.2	2,542,779	2,310,185	10%	10%
Mean error				-0.12%	42%

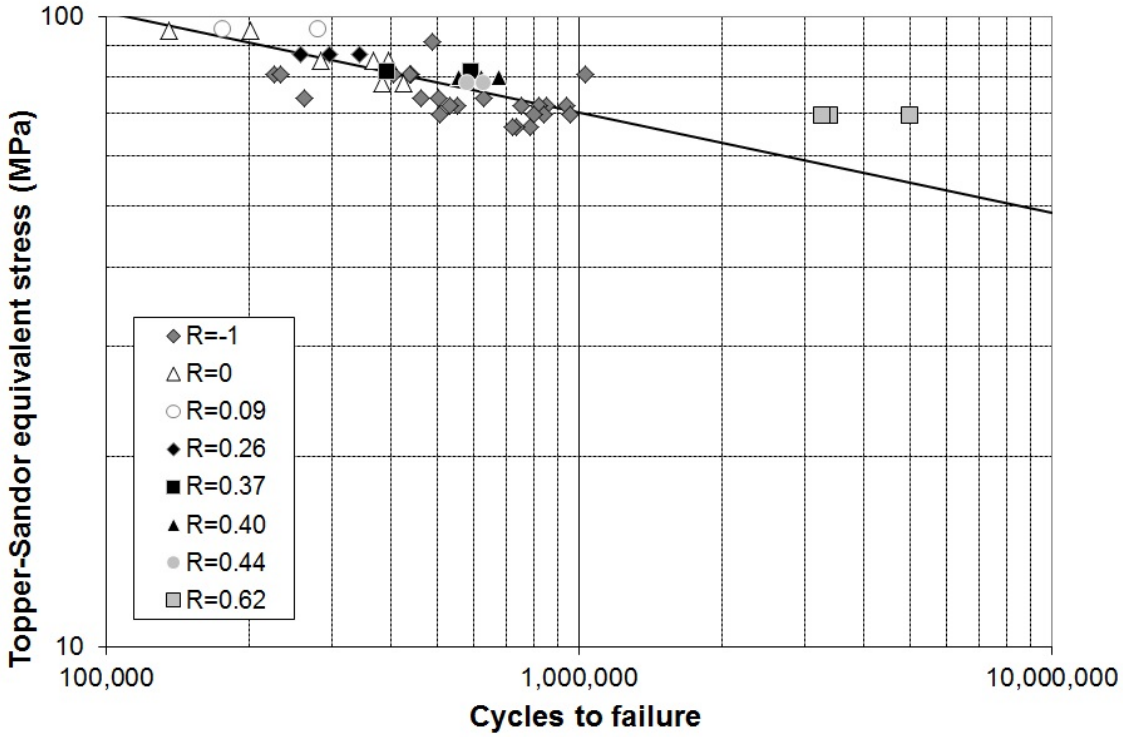

Figure A17. Topper-Sandor equivalent stress vs. cycles to failure for 356-T6 with machined surface.

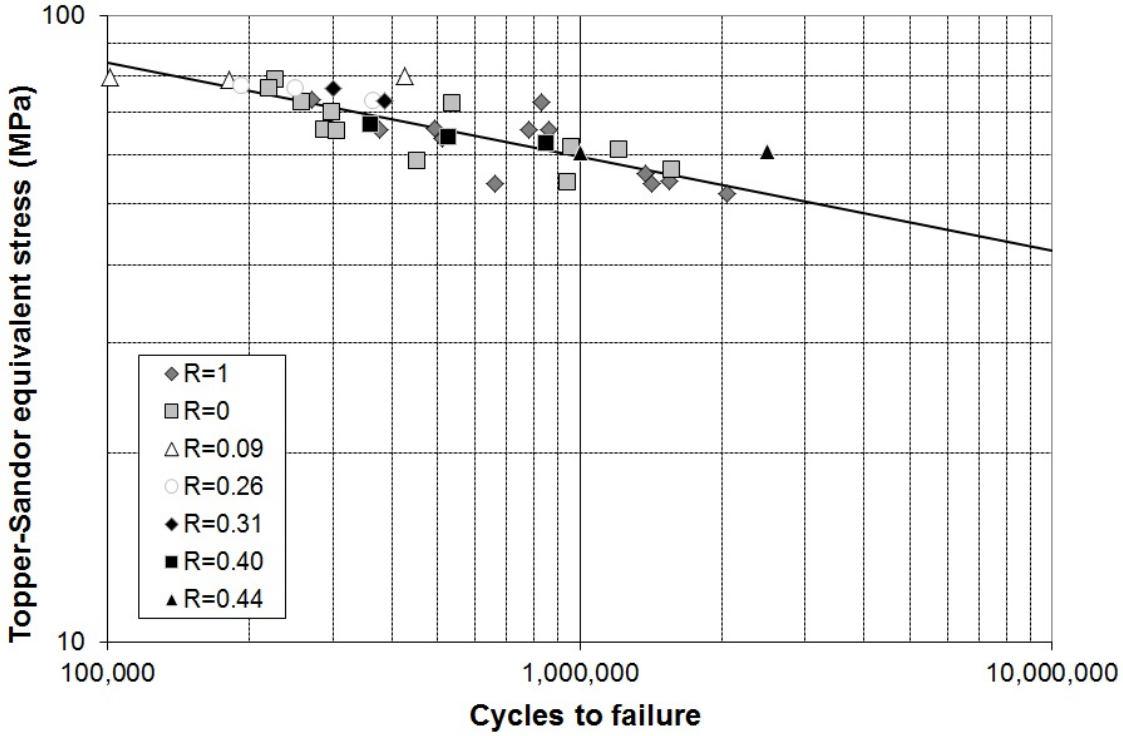

Figure A18. Topper-Sandor equivalent stress vs. cycles to failure for 356-T6 with as-cast surface.

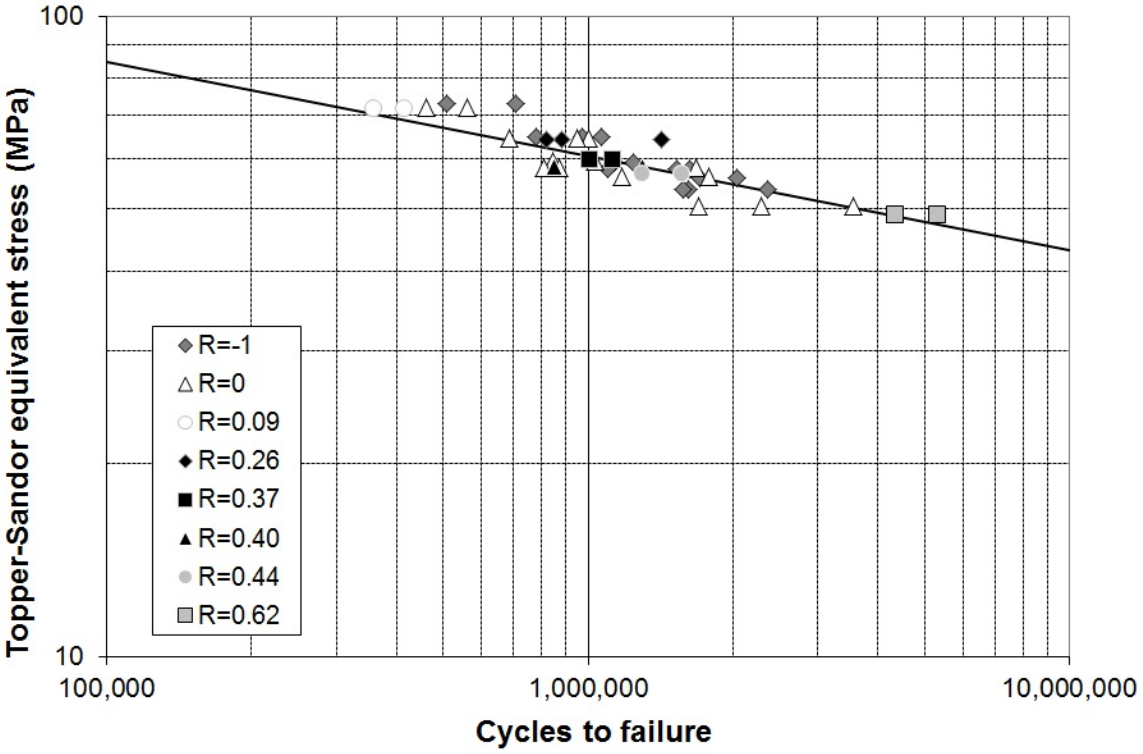

Figure A19. Topper-Sandor equivalent stress vs. cycles to failure for 356-T7 with machined surface.

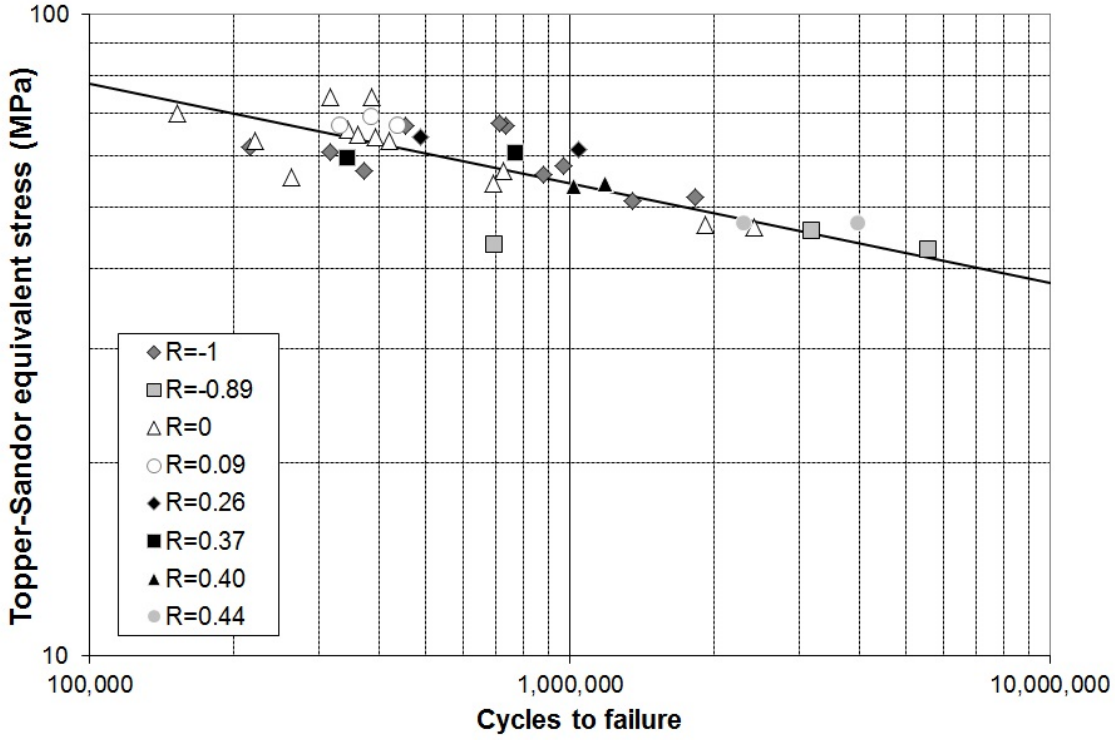

Figure A20. Topper-Sandor equivalent stress vs. cycles to failure for 356-T7 with as-cast surface.

A1.6 WALKER EQUATION

Table A21. Walker equivalent stress for 356-T6 with machined surface

R	Walker equivalent stress (MPa)	Predicted cycles to failure	Actual cycles to failure	Error	Absolute error
0	96.4	138,393	202,239	-32%	32%
0	96.4	138,393	135,864	2%	2%
0	85.7	289,927	366,497	-21%	21%
0	85.7	289,927	395,475	-27%	27%
0	85.7	289,927	283,696	2%	2%
0	78.5	502,123	384,069	31%	31%
0	78.5	502,123	424,776	18%	18%
0	76.3	601,420	470,594	28%	28%
0	76.3	601,420	378,667	59%	59%
0	76.3	601,420	338,151	78%	78%
0	73.8	736,764	461,822	60%	60%
0	73.8	736,764	481,782	53%	53%
0	65.9	1,497,359	796,653	88%	88%
0	65.9	1,497,359	871,396	72%	72%
0.09	97.2	131,654	280,705	-53%	53%
0.09	97.2	131,654	176,107	-25%	25%
0.26	87.9	247,955	296,894	-16%	16%
0.26	87.9	247,955	343,288	-28%	28%
0.26	87.9	247,955	256,863	-3%	3%
0.37	81.6	395,162	391,778	1%	1%
0.37	81.6	395,162	590,600	-33%	33%
0.40	79.6	458,492	555,037	-17%	17%
0.40	79.6	458,492	621,528	-26%	26%
0.40	79.6	458,492	674,470	-32%	32%
0.44	77.5	544,632	630,037	-14%	14%
0.44	77.5	544,632	580,154	-6%	6%
0.62	64.5	1,713,153	5,026,118	-66%	66%
0.62	64.5	1,713,153	3,381,193	-49%	49%
0.62	64.5	1,713,153	3,267,615	-48%	23%
Mean error				-0.20%	33%

Table A22. Walker equivalent stress for 356-T6 with as-cast surface

R	Walker equivalent stress (MPa)	Predicted cycles to failure	Actual cycles to failure	Error	Absolute error
0	80.0	136,424	226,313	-40%	40%
0	77.4	169,807	220,236	-23%	23%
0	72.9	254,596	537,623	-53%	53%
0	73.5	240,650	257,484	-7%	7%
0	70.5	317,469	298,635	6%	6%
0	66.0	494,907	288,027	72%	72%
0	65.4	522,625	306,850	70%	70%
0	60.8	849,268	1,210,621	-30%	30%
0	58.3	1,122,965	451,319	149%	149%
0	61.4	801,971	959,461	-16%	16%
0	56.3	1,419,903	1,570,361	-10%	10%
0	53.6	1,977,189	942,849	110%	110%
0.09	81.5	120,074	425,327	-72%	72%
0.09	80.9	126,972	101,433	25%	25%
0.09	80.2	134,205	180,438	-26%	26%
0.26	77.4	170,551	250,808	-32%	32%
0.26	78.0	160,973	192,455	-16%	16%
0.26	73.6	238,815	365,086	-35%	35%
0.31	77.2	173,111	300,408	-42%	42%
0.31	73.3	243,799	386,571	-37%	37%
0.40	61.4	799,730	850,922	-6%	6%
0.40	66.2	481,558	359,927	34%	34%
0.40	62.9	678,197	528,929	28%	28%
0.44	59.2	1,014,264	2,496,331	-59%	59%
0.44	58.7	1,072,039	1,002,257	7%	7%
Mean error				-0.06%	40%

Table A23. Walker equivalent stress for 356-T7 with machined surface

R	Walker equivalent stress (MPa)	Predicted cycles to failure	Actual cycles to failure	Error	Absolute error
0	73.5	265,114	559,273	-53%	53%
0	73.5	265,114	461,839	-43%	43%
0	65.3	593,729	1,005,070	-41%	41%
0	65.3	593,729	947,782	-37%	37%
0	65.3	593,729	684,971	-13%	13%
0	59.8	1,081,461	1,034,306	5%	5%
0	59.8	1,081,461	846,376	28%	28%
0	58.1	1,307,194	1,674,938	-22%	22%
0	58.1	1,307,194	809,932	61%	61%
0	58.1	1,307,194	873,339	50%	50%
0	56.2	1,645,235	1,781,136	-8%	8%
0	56.2	1,645,235	1,178,452	40%	40%
0	50.2	3,541,939	1,694,084	109%	109%
0	50.2	3,541,939	2,286,468	55%	55%
0	50.2	3,541,939	3,566,207	-1%	1%
0.09	73.6	262,991	414,472	-37%	37%
0.09	73.6	262,991	358,191	-27%	27%
0.26	65.5	579,001	880,352	-34%	34%
0.26	65.5	579,001	819,491	-29%	29%
0.26	65.5	579,001	1,417,558	-59%	59%
0.37	60.1	1,041,927	1,129,332	-8%	8%
0.37	60.1	1,041,927	1,008,951	3%	3%
0.40	58.4	1,257,113	848,269	48%	48%
0.40	58.4	1,257,113	1,298,928	-3%	3%
0.44	56.6	1,557,289	1,295,199	20%	20%
0.44	56.6	1,557,289	1,567,027	-1%	1%
0.62	45.9	6,497,585	4,361,461	49%	49%
0.62	45.9	6,497,585	24,870,798	-74%	74%
0.62	45.9	6,497,585	5,329,296	22%	22%
Mean error				0.04%	34%

Table A24. Walker equivalent stress for 356-T7 with as-cast surface

R	Walker equivalent stress (MPa)	Predicted cycles to failure	Actual cycles to failure	Error	Absolute error
0	71.1	179,393	152,661	18%	18%
0	66.7	272,042	345,206	-21%	21%
0	65.0	320,263	393,661	-19%	19%
0	75.7	119,531	386,067	-69%	69%
0	75.7	119,531	317,172	-62%	62%
0	63.9	356,303	221,445	61%	61%
0	65.6	301,400	362,635	-17%	17%
0	63.9	357,986	421,559	-15%	15%
0	55.5	886,661	262,855	237%	237%
0	57.0	750,934	727,386	3%	3%
0	54.1	1,042,562	693,066	50%	50%
0	45.8	3,061,683	2,413,722	27%	27%
0	46.2	2,903,349	1,914,190	52%	52%
0.09	70.2	195,325	385,936	-49%	49%
0.09	68.0	240,519	439,254	-45%	45%
0.09	68.0	240,519	332,457	-28%	28%
0.26	65.0	319,446	489,908	-35%	35%
0.26	62.0	436,516	1,042,450	-58%	58%
0.37	59.5	564,805	345,067	64%	64%
0.37	61.0	482,256	770,908	-37%	37%
0.40	53.4	1,142,551	1,018,546	12%	12%
0.40	53.8	1,084,396	1,180,591	-8%	8%
0.44	45.6	3,172,227	3,991,069	-21%	21%
0.44	46.3	2,858,719	10,107,592	-72%	72%
0.44	45.6	3,172,227	2,310,185	37%	37%
Mean error				0.20%	45%

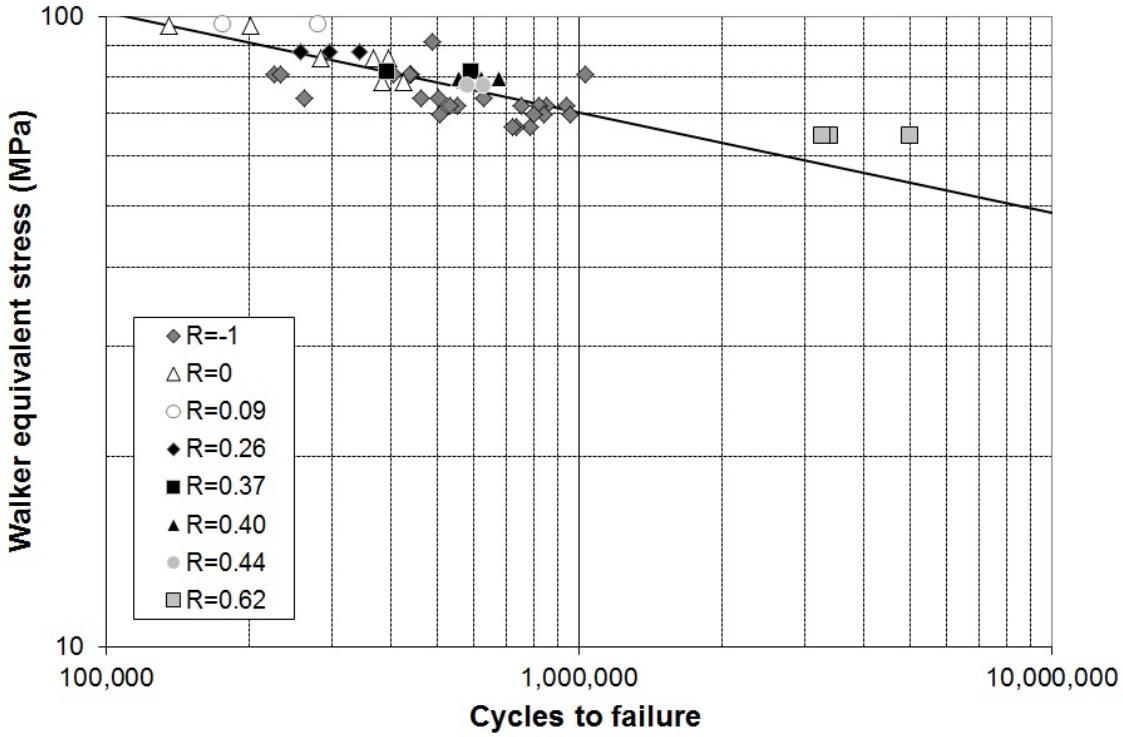

Figure A21. Walker equivalent stress vs. cycles to failure for 356-T6 with machined surface.

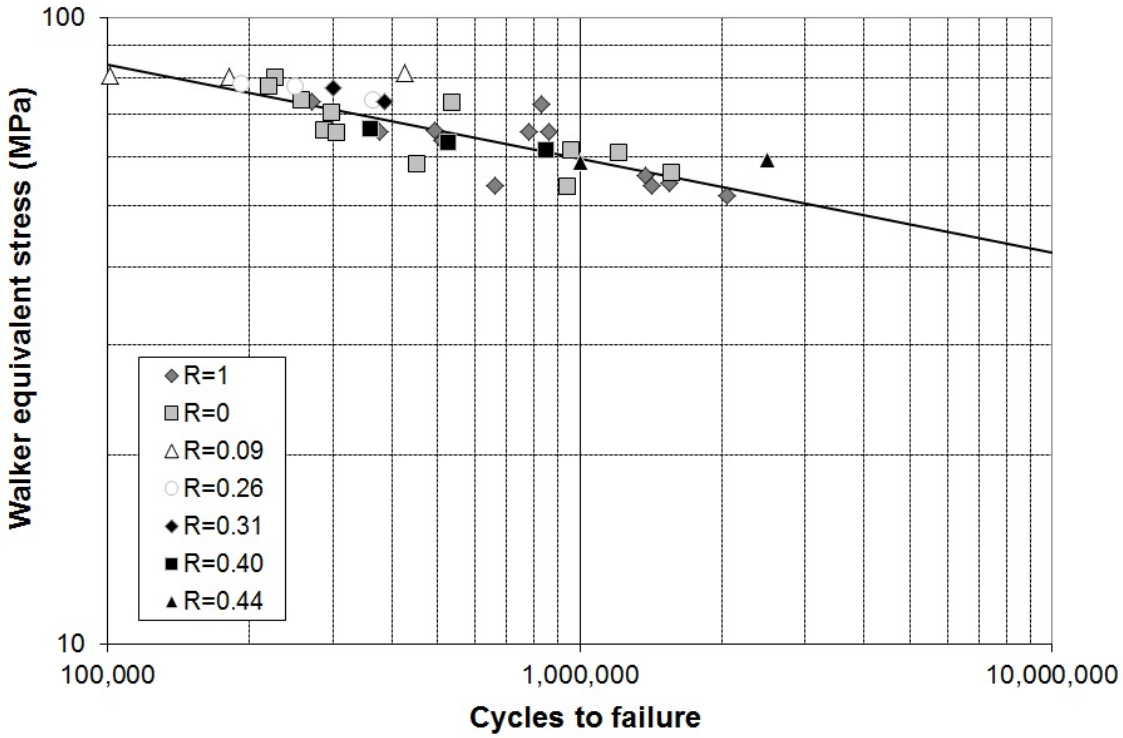

Figure A22. Walker equivalent stress vs. cycles to failure for 356-T6 with as-cast surface.

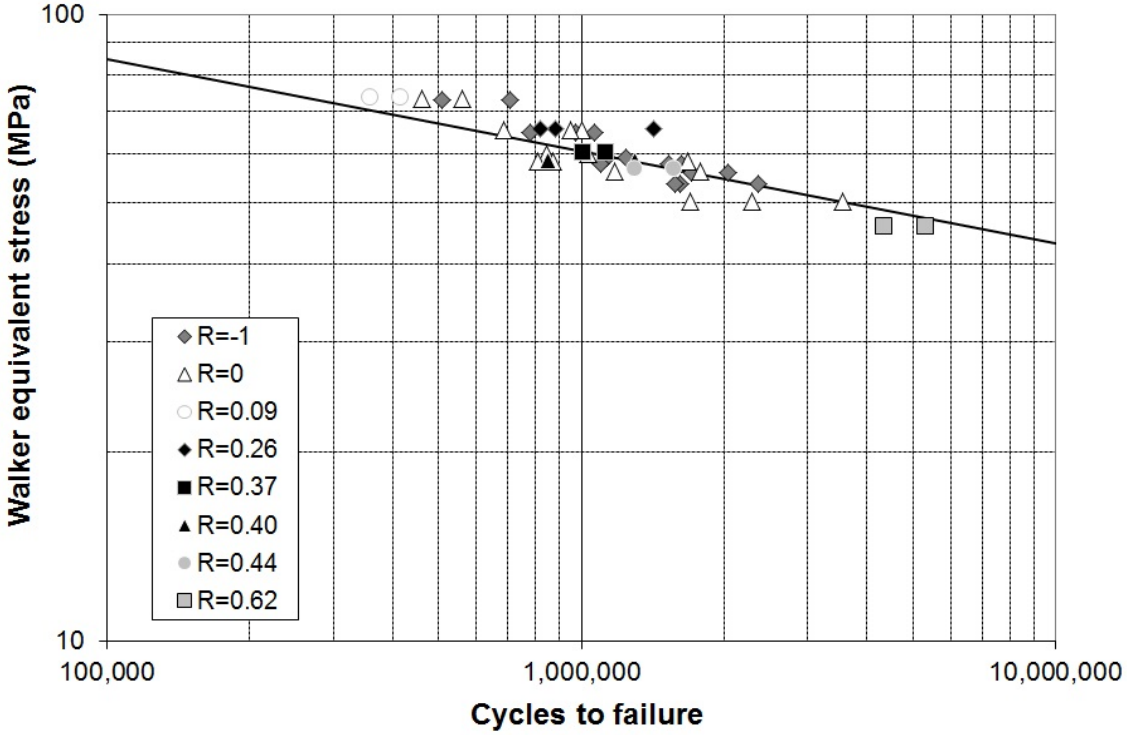

Figure A23. Walker equivalent stress vs. cycles to failure for 356-T7 with machined surface.

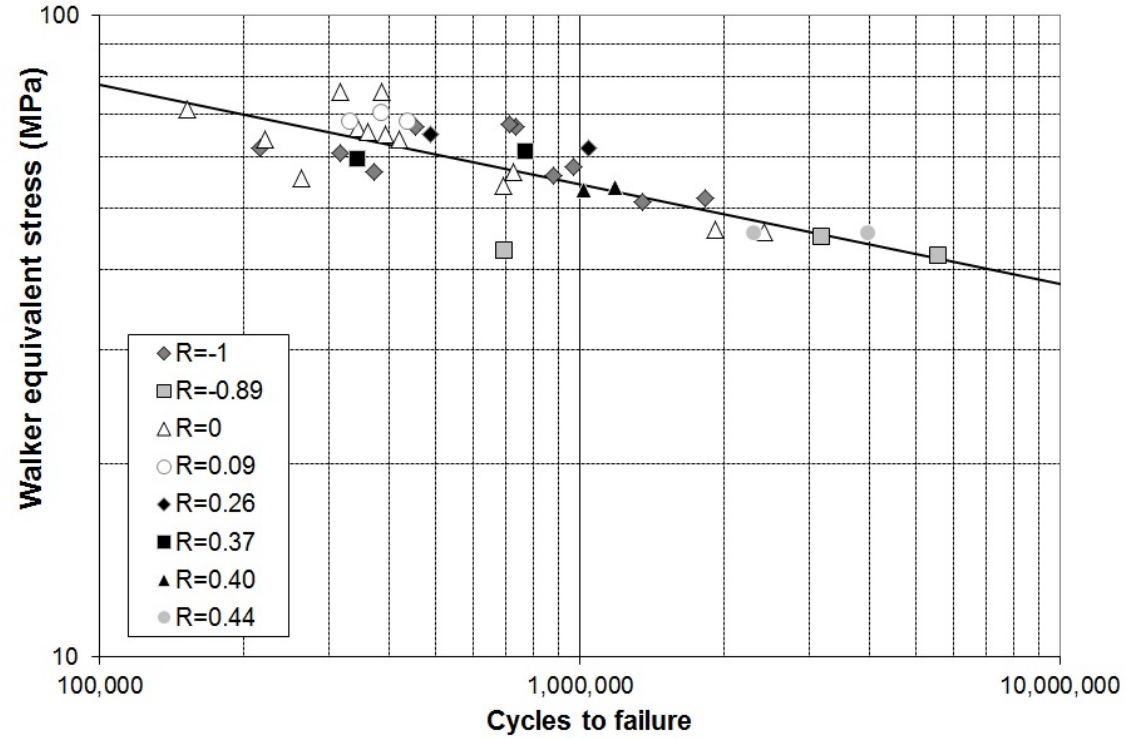

Figure A24. Walker equivalent stress vs. cycles to failure for 356-T7 with as-cast surface.